Bio-inspired dry adhesives from carbon nanofibers and their potential use in space technology

Zur Erlangung des akademischen Grades
Doktor der Ingenieurwissenschaften
der Fakultät für Maschinenbau
Karlsruher Institut für Technologie (KIT)

genehmigte
Dissertation
von

M.Sc. Christian Lutz

Tag der mündlichen Prüfung:	5. Dezember 2018
Hauptreferent:	PD Dr. Hendrik Hölscher
Korreferenten:	Prof. Dr. Martin Dienwiebel Prof. Dr. André Schirmeisen

Abstract

The outstanding ability of geckos to run up and down a tree as well as hanging on ceilings, fascinated mankind for a long time. Their adhesion properties originate from millions of nanohairs covering their toes, which built the end part of a sophisticated hierarchical micro- and nanoscale system. The nanohairs contacting the surface and adhere due to Van der Waals forces. This enables the gecko to adhere on nearly every surface. However, due to their nanometer-size and complex geometry, it is a challenge to mimic those structures with artificial materials using state of the art fabrication processes.

The presented approach for mimicking the attachment system of a gecko is based on carbon nanotubes/nanofibers. Due to their diameters in the nanometer-range, they are perfect candidates for mimicking the nano-hairs of geckos. In difference to polymers carbon nanotubes/nanofibers offer high temperature stability and outstanding mechanical properties.

Therefore, the adhesion properties between vertically aligned carbon nanotube arrays (fabricated with plasma enhanced chemical vapor deposition) and debris parts of meteorites mounted to cantilevers were investigated, for their use under harsh conditions such as in space. The adhesion measurements were conducted by atomic force microscopy at temperatures ranging from -20 °C to +240 °C, before and after exposing the carbon nanotube arrays to simulated space conditions. The measured adhesion properties were practically constant with an adhesion force of 2.5 N/cm² over the investigated temperature range. Additionally, the adhesion properties between micro-ice layers and carbon nanofiber bundles mounted to cantilevers were investigated, revealing constant adhesion properties with an adhesion force of 2.3 N/cm².

However, a simple and low-cost fabrication process to grow carbon nanotube/nanofiber based dry adhesive surfaces would be desirable. Therefore, a novel fabrication process to grow carbon nanofibers with flame synthesis in an open ethanol flame was developed. The carbon nanofibers can be oriented during growth by applying a magnetic field. The fabricated carbon nanofiber arrays were investigated after their adhesion properties with atomic force microscopy. The measured adhesion forces and energies rise linear with increasing preload force. Oriented carbon nanofibers reveal 68 % higher adhesion forces of up to 0.66 N/cm², compared with randomly aligned carbon nanofibers. Endurance tests revealed constant adhesion forces and energies, for up to 50 000 attachment/detachment cycles.

Lastly, during further development of the flame synthesis process with an increase in the thickness of the copper support layer, the growth of a novel kind of carbon nanofibers was discovered. The resulting structures were named ‘lambda shaped carbon nanofiber’ due to their similarity to the Greek letter lambda. Lambda shaped carbon nanofibers have two ‘feet’ connected with the ground and optional a free standing ‘head’. Higher flame velocities, achieved in a micro channel structure due to dynamic pressure at the inlet, result in the growth of twisted lambda shaped carbon nanofibers, with two twisted feet and a non-twisted head.

Kurzfassung

Die herausragende Fähigkeit von Geckos Bäume hoch und runter zu laufen sowie an der Decke hängen zu können, fasziniert die Menschheit schon sehr lange. Ihre Adhäsionseigenschaft beruht auf Millionen von Nanohaaren die ihre Füße bedecken und den obersten Teil eines hochentwickelten hierarchischen Mikro- und Nanosystems bilden. Die Nanohaare kontaktieren die Oberfläche und haften aufgrund von van-der-Waals Kräften. Dies ermöglicht dem Gecko das Haften an nahezu allen Oberflächen. Aufgrund der komplexen Geometrie im nm-Bereich ist es allerdings eine Herausforderung solche Strukturen mit künstlichen Materialien und unter Verwendung etablierter Herstellungsprozesse nachzuahmen.

Der hier vorgestellte Ansatz zur Nachahmung des Gecko-Haftsystems basiert auf Kohlenstoffnanoröhren und Kohlenstoffnanofasern. Aufgrund der Durchmesser im nm-Bereich, eignen sie sich hervorragend für die Nachahmung der Nanohaare eines Geckos. Kohlenstoffnanoröhren/Kohlenstoffnanofasern besitzen zudem im Vergleich mit Polymeren, welche ebenfalls zur Nachahmung von Haftstrukturen eingesetzt werden, eine hohe Temperaturstabilität und herausragende mechanische Eigenschaften.

Daher wurden die Adhäsionseigenschaften zwischen Feldern mit vertikal ausgerichteten Kohlenstoffnanoröhren und Bruchstücken von auf Biegebalken befestigte Meteoriten, für den Einsatz unter rauen Bedingungen wie z.B. im Weltraum untersucht. Für die Adhäsionsmessungen wurde ein Rastersondenmikroskop eingesetzt. Der untersuchte Temperaturbereich lag zwischen -20 °C bis +240 °C. Die Messung wurde vor und nach Aussetzung der Kohlenstoffnanoröhren in simulierten Weltraumbedingungen durchgeführt. Es zeigten sich nahezu konstante Adhäsionseigenschaften mit einer Adhäsionskraft von 2.5 N/cm^2 in dem untersuchten Temperaturbereich. Zusätzlich wurden die Adhäsionseigenschaften zwischen Mikro-Eis Oberflächen und Bündel mit Kohlenstoffnanoröhren untersucht. Es zeigten sich ebenfalls konstante Adhäsionseigenschaften mit einer Adhäsionskraft von 2.3 N/cm^2.

Ein einfacher und kostengünstiger Herstellungsprozess für auf Kohlenstoffnanoröhren/Kohlenstoffnanofasern basierende Adhäsionsoberflächen wäre wünschenswert. Deshalb wurde ein neuer Herstellungsprozess zum Wachstum von Kohlenstoffnanofasern mittels Flammsynthese in einer offenen Ethanolflamme entwickelte. Durch Anlegen eines magnetischen Feldes konnten die Kohlenstoffnanofasern während des Wachstums ausgerichtet werden. Die so hergestellten Felder mit Kohlenstoffnanofasern wurden auf ihre Adhäsionseigenschaften mittels Rastersondenmikroskop untersucht. Die gemessenen Adhäsionskräfte und Adhäsionsenergien stiegen dabei linear mit der Erhöhung der Anpresskraft an. Verglichen mit den zufällig ausgerichteten Kohlenstoffnanofasern wiesen ausgerichtete Kohlenstoffnanofasern 68 % höhere Adhäsionskräfte mit bis zu 0.66 N/cm^2 auf. Ausdauertests zeigten konstante Adhäsionskräfte und Adhäsionsenergien für 50 000 Messzyklen.

Schließlich wurde während der konsequenten Weiterentwicklung des Flammsynthese-Prozesses durch die Verwendung dickerer Unterstützungsschichten aus Kupfer eine neue Art des Kohlenstoffnanofaser-Wachstumes entdeckt. Die erhaltenen Strukturen wurden aufgrund ihrer Ähnlichkeit mit dem griechischen Buchstaben Lambda, “lambdaförmige Kohlenstoffnanofasern“ getauft. Lambdaförmige Kohlenstoffnanofasern haben zwei mit dem Boden verbundenen “Füße“ und optional einen frei stehenden “Kopf“. Höhere Geschwindigkeiten der Flamme, erzeugt durch den dynamischen Druck am Eingang eines Mikrokanals, resultierten im Wachstum von gedrehten lambdaförmige Kohlenstoffnanofasern, mit zwei verdrehten “Füßen“ und einem nicht verdrehten “Kopf“.

Contents

List of figures

List of tables

List of abbreviations

AFM	atomic force microscope
CNF	carbon nanofiber
CNT	carbon nanotube
CVD	chemical vapor deposition
DPN	dip-pen nanolithography
FIB	focused ion beam
HRTEM	high-resolution transmission electron microscope
LL5	low iron and low metal meteorite of type 5
NTFs	nanotriplefibers
NWA	northwest Africa (find spot of meteorites)
PECVD	plasma enhanced chemical vapor deposition
PS-b-P2VP	poly(styrene)-block-poly(2-vinyl pyridine)
SEM	scanning electron microscope
SFM	scanning force microscope
XPS	X-ray photoelectron spectroscope
µCS	microchannel cantilever spotting
ΛCNF	lambda shaped carbon nanofiber (with two feet)
λCNF	lambda shaped carbon nanofiber (with two feet and a head)
$\vec{a}_1, \vec{a}_2$	unit vectors
A	area
A_H	Hamaker constant
B	magnetic flux
B_r	remanence
$\vec{C}_h$	lattice vector
d	diameter
D, z	distances

e	vapor pressure
E_{abs}	absorbed energy
E_{adh}	adhesion energy
f_0	resonance frequency
F	force
F_{pre}	preload force
F_{adh}	adhesion force
g_a	growth activity
k	spring constant
m	mass
m_{eff}	effective mass
M	mass at the cantilever end
n, m, q, N	integers
r, R	radiuses
R_w	gas constant
s	length
t	penetration depth
T	temperature
V	volume
α	angle
γ	work of adhesion
θ	chiral angle
ξ	adhesion energy per area
ρ_w	absolute humidity
σ	adhesion force per area
φ	relative humidity

1 Introduction

1.1 Motivation

Many devices created by mankind are inspired by nature. Airplanes, submarines, and jet engines are historical examples for the successful mimicking of birds and sea creatures [1]–[3]. The motivation for the design of such tools is typically caused by the fascination about the famous abilities of animals and plants. The strong adhesion of gecko's toes [4], [5] and the self-cleaning properties of the lotus leave [6] are two illustrative and very popular examples for this process of bio-inspired engineering. Geckos fascinate mankind for a long time. When a gecko is walking up and down a tree, or hanging on the ceiling, it seems that the gecko overcomes gravity. Already the Greek philosopher Aristoteles (4th century B.C.) described the ability of a gecko: "*It can run up and down a tree in any way, even with the head downwards*" [7]. Nevertheless, there are several other animals with the same ability like ants [8], bugs [9], and spiders [10]. However, the gecko deserves the most interest because it is the heaviest animal with adhesion properties. The Tokay gecko (Figure 1.1) with a total length up to 35 cm and a weight up to 300 g [11], is the biggest gecko and generates adhesion forces up to 10 N/cm² [5].

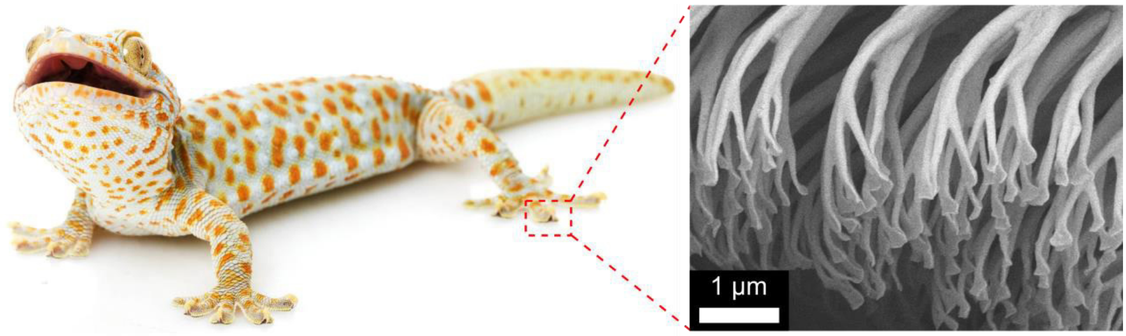

Figure 1.1: The Tokay gecko (left) with a scanning electron microscopy image of its hierarchical system of micro- and nanostructures (right). Photography of the gecko used under license from Shutterstock.com [12] and image of gecko structures adapted and reprinted with permission from Kellar Autumn [13].

Originally seven theories arose to explain the secret behind the famous adhesion of geckos for more than a century. Sticky secretions, micro-interlocking, micro-suction cups, electrostatic forces, friction, capillary forces, and intermolecular forces were discussed. Finally, the gecko's secret was solved by elimination. Friction cannot be the cause due to its definition. Friction appears only in shear direction, but geckos can stick to ceilings, even when the surface is very flat, such as polished glass or a silicon dioxide wafer [7]. This also eliminates the theory, that geckos use a kind of micro-interlocking. If micro-suction cups would be responsible for the adhesion of a gecko, they should not show any adhesion in vacuum. However, geckos revealed adhesion forces also in vacuum [14]. Furthermore, geckos do not have any kind of micro-suction cups. Electrostatic forces can be also eliminated, because geckos can stick to surfaces where no electrostatic forces can built-up [4]. Geckos do not have perspiratory glans on their toes which refute the theory of sticky secretions. However, condensed water from the atmosphere between the surface and the nanostructures of a gecko could generate additional capillary forces. Autumn *et al.* [7] rejected this hypothesis experimentally. They assume if capillary forces would be responsible for gecko's adhesion strength, the adhesion force of a gecko on hydrophobic surfaces should be very low compared with the adhesion force on hydrophilic surfaces. The outcome was that the adhesion force between a gecko setae and hydrophilic as well as hydrophobic surfaces are nearly the same. This finding rejected the hypothesis that capillary forces are the main cause for gecko adhesion.

Consequently, the remaining theory explaining gecko's secret are intermolecular forces [7]. This theory arose with the invention of electron microscopy, where the gecko revealed his secret in kind of a hierarchical system of micro- and nanostructures made by keratin on his toes [15]–[17]. The big 'hairs' are placed directly on the lamellae of the gecko and are called setae with diameters of around 4.2 µm and lengths of about 110 µm. The setae split four times and end in the so-called spatula with a triangular shape and a size of about 200 x 200 nm (Figure 1.1). The density of the setae is in the range of 14 400 setae/mm^2. The total amount of setae of a Tokay gecko is about 6.5 million. These structures can generate an adhesion force of 100 N for one gecko [5], in case that all nanohairs are in contact with the surface simultaneously. In general, this is much more than a gecko with a weight of 300 g needs, but it offers the gecko a tremendous safety factor. Consequently, a gecko is only using a few per cents of his maximum force. A possible reason for this is that not all hairs of the gecko can contact the surface at the same time, especially, when the surface is rough or contaminated with dust particles. To release its feet from the surface, the gecko is using a trick, it is rolling his toes to its inside to minimize the pull-off force to lift off one foot. This allows the gecko to lift-off its feet in only 15 ms. Additionally, the gecko, as well as most gecko-inspired adhesives have a self-cleaning mechanism. If the feet are contaminated with dust particles, the adhesion force between the gecko's hairs and the dust particles is lower than between dust particles and the surface resulting in a cleaning of the gecko's hairs with each release step [18].

The basic adhesion trick used by the gecko is based on the nm-size of the contacts, which can be explained by the contact splitting theory [19], [20]. Figure 1.2 shows two square areas with the same size. The left is contacted by only one big spherical tip and the right one by n smaller spherical tips. This leads to an increase in the adhesion force which rises with the square root of the number of spherical contacts:

$$F_c{}' = \sqrt{n}F_c, \tag{1.1}$$

where F_c is the adhesion force for one big spherical contact and F_c' is the adhesion force for n spherical contacts.

Beside contact splitting, the gecko developed another fascinated geometrical structure for its adhesion ability. The tips for contacting the surface are only the top part of a hierarchical system illustrated in Figure 1.3 on the right side. To stick on extremely flat surfaces (Figure 1.3 a), it is not necessary to have a hierarchical system of, e.g., four levels. In this case an attachment system without hierarchy can generate the same adhesion as a hierarchical system of multiple levels. However, the gecko's environment in the nature with surfaces such as trees and rocks are not flat. Therefore, a hierarchical system is of advantage compared to a system without hierarchy (Figure 1.3 b). A non-hierarchical attachment system cannot contact all of its hairs with rough surfaces resulting in a reduced adhesion. Additionally, if the hairs exceed a critical length, they stick together [21], which also results in a reduced adhesion after the contact splitting theory [19], [20]. Hierarchical structures do not stick together and are perfectly made for surface uncertainties which are present everywhere in nature. The hierarchical system of a gecko can be simplified regarded as a multiple-level spring model [22]–[25]. Figure 1.3 c) compares two spring models with a one-level hierarchy (left) and a four-level hierarchy (right), whereas the one-level hierarchy describes most of the artificial dry adhesives and a four-level hierarchy comes closer to the description of the real attachment system of a gecko.

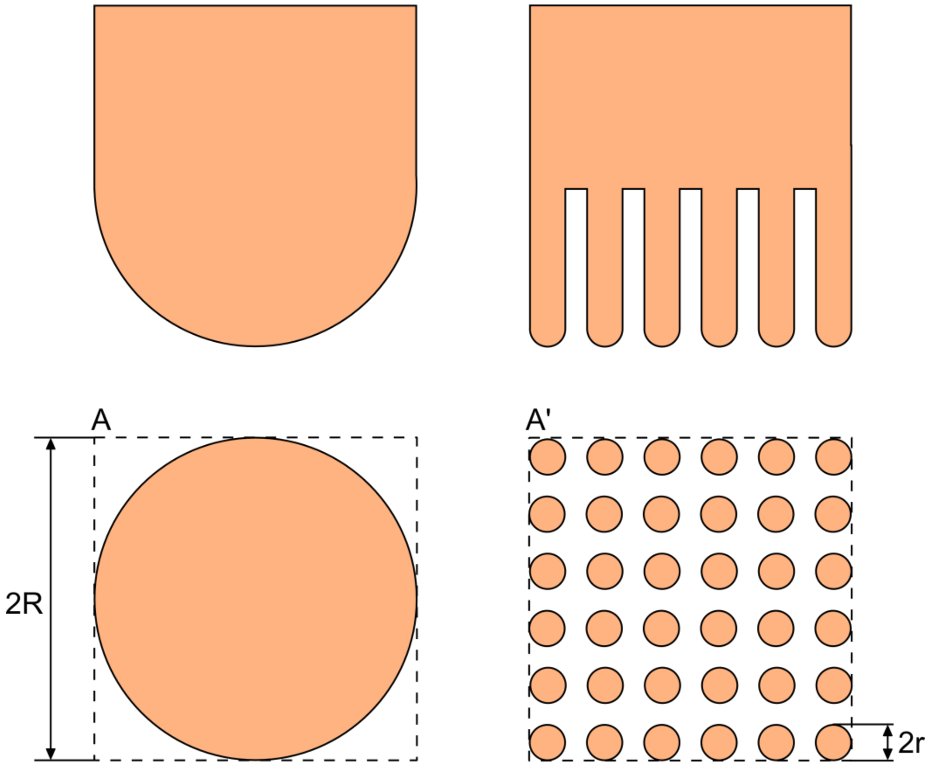

Figure 1.2: Contact splitting theory, with one spherical contact (left) and several spherical contacts (right). The side views are represented at the top whereas the top views are represented at the bottom. If the two arrays are identical, the adhesion rises with the square root of the number of contacts. Figure adapted from Arzt *et al.* [20].

The intermolecular forces such as van der Waals forces (vdW-forces) are mainly responsible for the adhesion of a gecko [7]. The vdW-forces [26] are interactions between atoms or molecules depending on the distance between the interaction partners. They are subdivided into three forces with the London dispersion forces (acting between temporary dipoles), the Debye forces (between permanent dipoles and induced dipoles), and the Keesom forces (between permanent dipoles). In practically all cases, the London dispersion forces are the strongest of the three vdW-forces. In the case of a sphere contacting a flat surface the vdW-force F can be calculated using the following Equation [27]:

$$F(D) = -\frac{A_H R}{6D^2}, \tag{1.2}$$

with the Hamaker constant A_H, the radius R and the distance D between the sphere and the surface [27]. However, it might be possible that the pillars at the end of the structures of a gecko buckling after touching the surface. In this case the vdW-force can be approximately calculated as the interacting between a cylinder and a flat surface expressed per unit length (N/m) using the following Equation [27]:

$$F(D) = -\frac{A_H\sqrt{R}}{8\sqrt{2}D^{\frac{5}{2}}}. \tag{1.3}$$

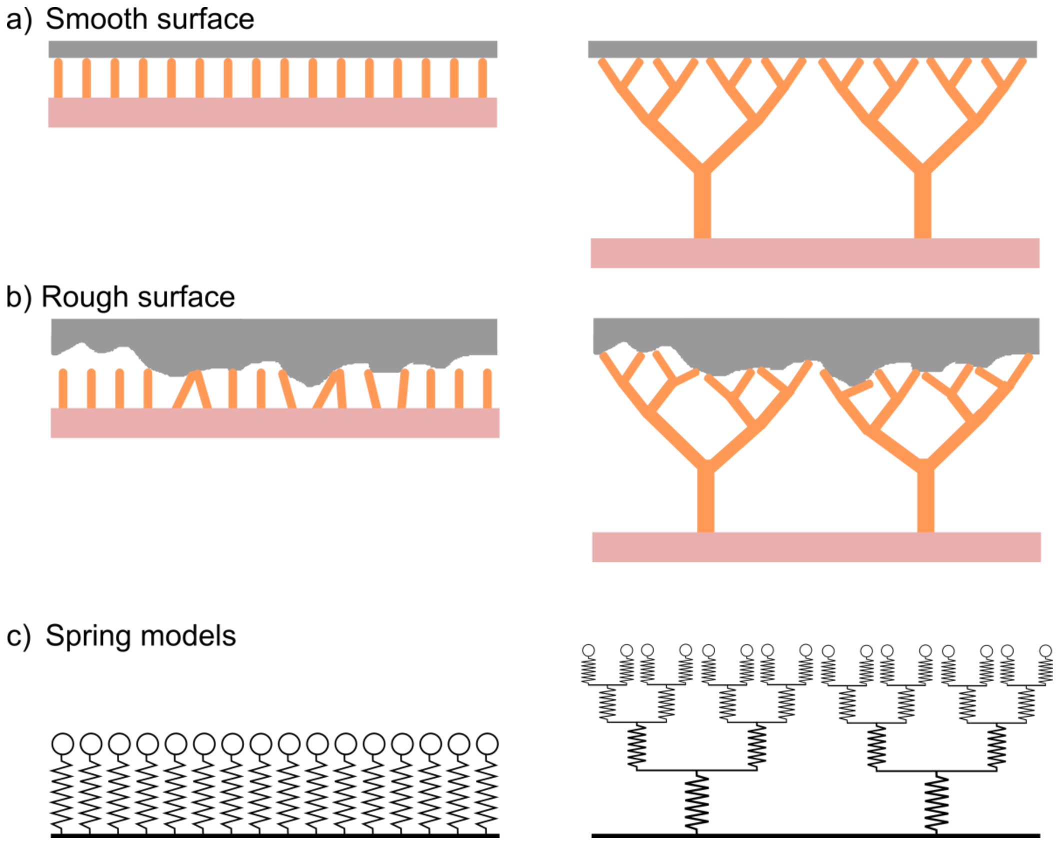

Figure 1.3: Flat versus hierarchical structures for contacting surfaces of different roughness, with a) a flat surface and b) a rough surface contacted by systems of pillars with a one-level hierarchy (left) and a four-level hierarchy (right). The four-level hierarchical system enables all of the pillars to contact the rough surface without agglutination of the pillars. c) The different level hierarchical systems can be described by using a spring model. Figure part c) adapted from Bhushan [22].

Mimicking the nanostructures of a gecko with artificial materials, such as polymers or carbon nanotubes/nanofibers can lead to high performance dry adhesives with a possible use in manufacturing to replace screws or glued connections, gloves in sport, e.g., to catch a ball better, for climbing aids or robots [28], in medicine as novel plasters [29] or for novel braking systems in automotive. Another field of application is space technology. Due to low- or zero gravity it is a challenge, e.g., to attach landing units on small bodies like meteorites, asteroids and comets. Dry adhesives which can cope under space conditions can solve such problems. Figure 1.4 shows a vision of a landing unit model which can cope with different underground materials, such as rock and ice surfaces.

Dry adhesives made by polymers are cost-effective with simple fabrication techniques [30]–[32]. However, the use of dry adhesives made by polymers is limited. High temperatures or the exposure to radiation (e.g., in space) might damage the structures made from polymers [33], [34]. Additionally, the size of such structures is limited by the used structuring technology.

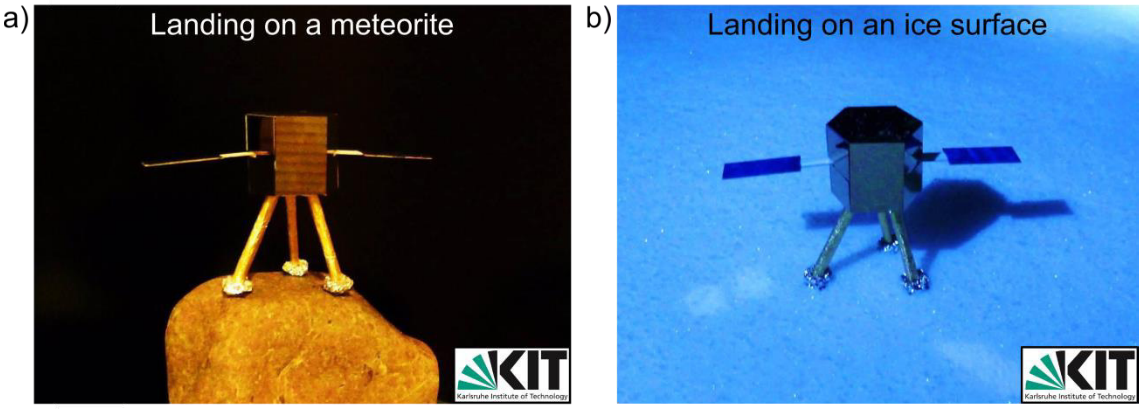

Figure 1.4: Vision of space probe landing on a) a meteorite and b) on an ice surface. It should be mentioned, that the lander on the images is a model and landing were performed on Earth.

Carbon nanotubes (CNTs) and carbon nanofibers (CNFs) are due to their possible available size from 1 µm down to 1 nm [35], [36] very promising to mimic the nanostructures of geckos [37]–[41]. They have outstanding mechanical properties such as a tensile strength of 150 GPa, a Young's modulus of 0.8 TPa [42] with a low density between 1.33 g/cm³ and 1.78 g/cm³ [43], [44]. Additionally, CNTs are stable under radiation [45] and at temperatures up to 750 °C in air and up to 2800 °C in vacuum [46]. Moreover, Y-shaped CNTs/CNFs [47]–[50] offers a promising possibility for mimicking the hierarchical structure of a gecko. Therefore, CNTs/CNFs are very promising materials for artificial dry adhesives.

However, it is not easy to fabricate CNTs/CNFs. State of the art processes like chemical vapor deposition (CVD) [51] or plasma enhanced chemical vapor deposition (PECVD) [52] require a sophisticated lab infrastructure, consume a certain amount of energy to facilitate the process and rely on several process gasses. Additionally, the growth of Y-shaped CNTs/CNFs with CVD or PECVD is not completely understood up to now. Therefore, a simple, environmental friendly and cost-effective way to grow CNT/CNF-based dry adhesives with the possibility to grow Y-shaped CNT/CNF-structures would boost the research in dry adhesives and nanotechnology.

1.2 Outline

The goal of this work was to develop a simple, low-cost process to grow CNTs/CNFs. This is achieved by using only an open ethanol flame, providing the necessary energy in terms of heat and acting simultaneously as carbon source. The produced CNT/CNF arrays are used as dry adhesives and investigated by atomic force microscopy (AFM) for their adhesion properties. Additionally, the adhesion properties under harsh conditions and their endurance ability were investigated. Chapter 2 provides an overview on CNTs/CNFs with respect to their properties and manufacturing processes. Additionally, the AFM based adhesion measurement principle is presented.

In Chapter 3, I present the adhesion properties of CNT arrays for their potential use under harsh conditions, as needed for space technology. Therefore, the adhesion properties between debris parts of meteorites mounted on AFM cantilevers and CNT arrays are measured at different temperatures before and after exposing the CNT arrays to simulated space conditions. Moreover, the adhesion between micro-ice layers and CNF bundles mounted to AFM cantilevers is investigated.

In Chapter 4, I describe the production of CNFs with a developed alternative growth process based on an open ethanol flame with the option to align the CNFs during growth with a permanent magnet. Using this method, randomly aligned as well as aligned CNFs were fabricated and investigated for their adhesion properties by AFM. Additionally, the long term stability of the fabricated CNF arrays was investigated for up to 50 000 attachment/detachment cycles.

In Chapter 5, I present the invention of a novel kind of CNFs grown with the advanced process from Chapter 4. I named these structures lambda-shaped CNFs due to their similarity to the Greek letter lambda. Therefore, a machine was developed to achieve precise process conditions with nearly no jitter in the ethanol flame. By using a new substrate with a 3 µm thick copper layer, the growth of lambda shaped CNFs was discovered. AFM based microchannel cantilever spotting (µCS) and dip-pen nanolithography (DPN) were performed for the controlled deposition of catalysts, to investigate the locally controlled growth of single lambda shaped CNFs on defined substrate positions. Using higher flame velocities, produced in a channel structure due to dynamic pressure at the inlet, resulted in the growth of twisted lambda shaped CNFs with two twisted feet CNFs and a not twisted head CNF.

Finally, Chapter 6 gives a conclusion of my study and an outlook on possible future experiments and developments.

2 Materials and methods

For the fabrication and development of novel gecko-inspired dry adhesives based on carbon nanostructures, a fundamental understanding of these structures is necessary. This chapter gives an overview on the properties of carbon nanotubes and related material thereof, growth theories, and common fabrication processes. Additionally, the AFM based adhesion measurement for the investigation and characterization of adhesive nanostructures is presented.

2.1 Carbon nanotubes

Due to their outstanding properties, carbon nanotubes (CNTs) are regarded as one of the most promising materials for the 21st century, with countless possible applications like lightweight CNT composites for the use in automotive, aerospace, for ships or in sporting goods as tennis rackets and bicycle frames [53]. Additionally, with their small size in the nm-range and their outstanding properties, CNTs are perfectly made for mimicking Gecko-inspired dry adhesives [37], [40], [41], [54]. This chapter gives an overview about different kind of CNTs and their respective properties. Especially, the theoretical theory describing CNTs growth and the different manufacturing processes of CNTs is introduced in this section.

2.1.1 Properties of carbon nanotubes

There are two natural modifications of carbon on Earth. Graphite (sp^2-bonded) consists of carbon atoms ordered in 2D layers stacking over each other with an angle of 120° between. One layer of graphite can be regarded as a honeycomb structure which is called graphene. Diamond (sp^3-bonded) consists of carbon atoms spatial arranged with an angle of 109.5° between. The third carbon modification was discovered in 1985 by Kroto *et al.* [55] during laser evaporation of graphite with spherical carbon structures of 60 atoms (C_{60}) and ellipsoid structures of 70 atoms (C_{70}). A fourth modification of carbon was discovered in 1991 by Iijima [56] and, is called carbon nanotubes (CNTs).

CNTs are hollow cylinders made by graphene layers which belong to the class of carbon nanofibers (CNFs). CNFs normally do not reveal perfectly ordered cylindrical graphene layers. CNTs and CNFs are called one dimensional carbon nanostructures (1D-CNs). An overview of all possible 1D-CNs with their appearance in cross sections is depicted in Figure 2.1.

CNTs have typical diameters in the nm-range and lengths in the µm-range, with a Young's modulus up to 1.25 TPa [57] and a tensile strength up to 63 GPa [58]. There are several types of CNTs, which distinguish from each other by their number of graphene layers. Table 2.1 shows an overview of different kinds of 1D-CNs and their properties.

Single walled carbon nanotubes (SWCNTs) are built up of only one graphene layer and have outer diameters between 1 – 2 nm [35]. SWCNTs have a Young's modulus of 1.25 TPa [57] and a tensile strength of 3.6 GPa [59]. The density of SWCNTs is in the range of 1.33 – 1.4 g/cm³ [43]. To distinguish different kind of SWCNTs with different properties, the vector notation from Saito *et al.* [60] can be used. A SWCNT can be imagined as rolling a cylinder from a graphene sheet (Figure 2.2). After rolling, the atoms A and A' lie imaginary over each other. The distance between A and A' is described by the lattice vector:

$$\vec{C_h} = n\vec{a}_1 + m\vec{a}_2 \equiv (n, m), \tag{2.1}$$

where $\vec{a}_1$ and $\vec{a}_2$ are the unit vectors of graphite multiplied with multiples (n and m) of the unit vectors. Consequently, the diameter of a SWCNT can be calculated from the lattice vector.

$$\mathrm{d} = \frac{|\vec{C_h}|}{\pi} \tag{2.2}$$

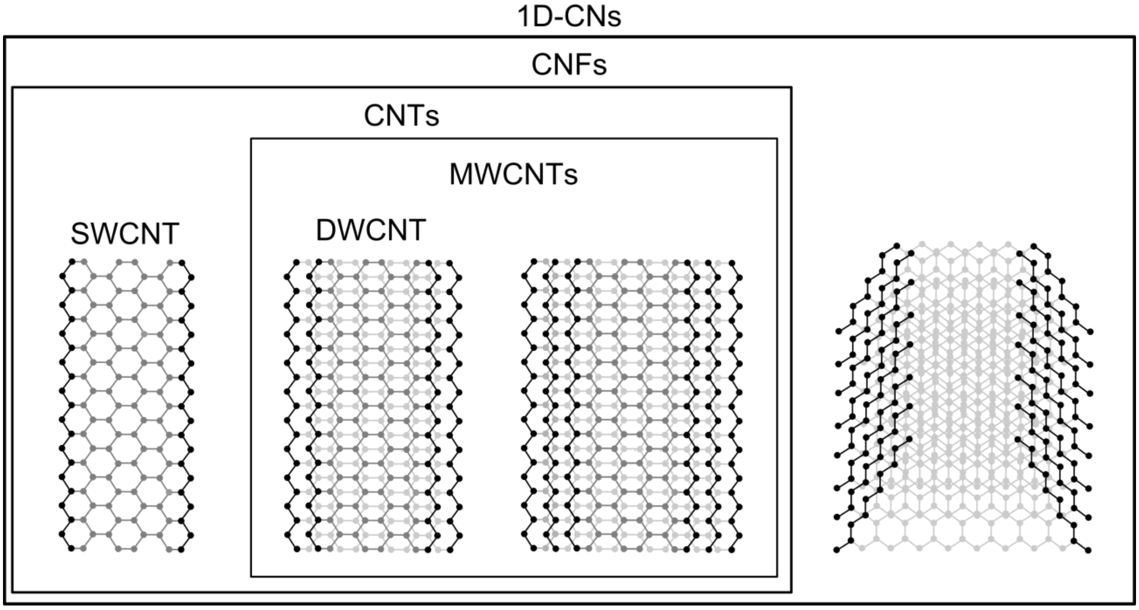

Figure 2.1: Cross section of all possible 1D-CNs structures. The smallest structures are SWCNTs consisting of one graphene layer. Nanotubes consisting of two graphene layers are called DWCNTs. Nanotubes consisting of more than two graphene layers and DWCNTs are called MWCNTs. SWCNTs and MWCNTs belong to the group of CNTs. A feature of the CNTs is the cylindrical, ordered arrangement of graphene layers. Imperfect cylindrical structures with herringbone arrangement of the graphene layers as shown on the right side are called CNFs. CNTs belong also to the group of CNFs.

The angle between the lattice vector and the horizontal line is called chiral angle θ and can be calculated from the multiples of the graphite unit vectors.

$$\theta = \tan^{-1}\left(-\frac{\sqrt{3}m}{2n + m}\right) \tag{2.3}$$

Using this vector notation, three different kinds of SWCNTs can be defined. Zigzag SWCNTs have a chiral angle of zero ($n > 0$ and $m = 0$). Armchair SWCNTs have a chiral angle of 30° ($n = m$). All other combinations with $n \neq m \neq 0$ are called chiral SWCNTs [35]. The metallic or semiconducting SWCNT can be distinguish with the ratio of the multiples.

$$2n + m = 3q \tag{2.4}$$

A SWCNT is conductive, when q is an integer and semiconductive for all other cases. Armchair SWCNTs are always metallic and therefore conductive, whereas zigzag and chiral SWCNTs can be metallic or semiconducting. Assuming that all values of chiral vectors are possible, one third of all possible SWCNTs are metallic and two thirds are semiconducting [61].

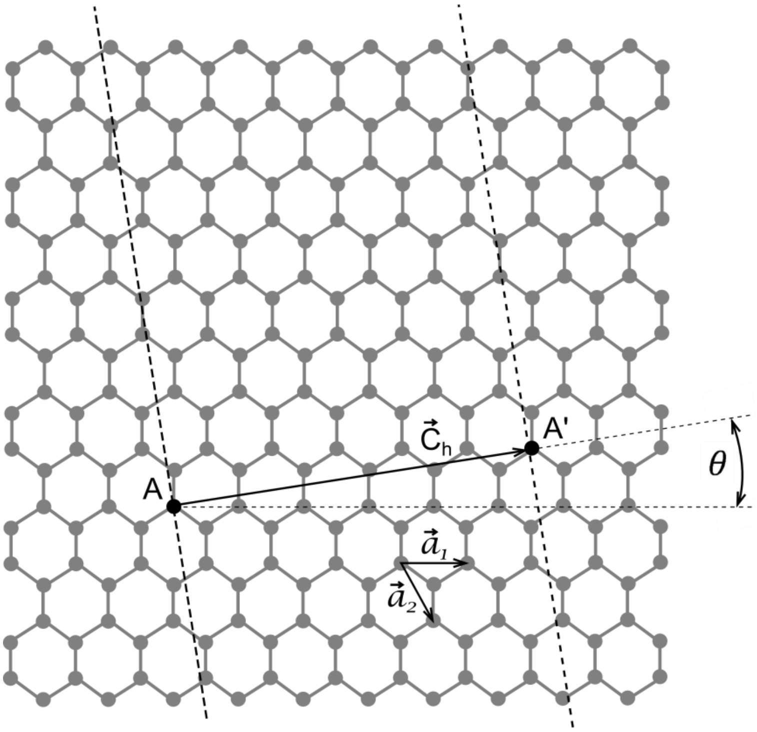

Figure 2.2: SWCNT characterization on a graphene sheet. A SWCNT can be imagined by rolling a cylinder from a graphene sheet. The perimeter of the SWCNT is the lattice vector $\vec{\boldsymbol{C}}_{\boldsymbol{h}}$, which is built by a multiple of the unit vectors of graphite ($\vec{\boldsymbol{a}}_{\mathbf{1}}$ and $\vec{\boldsymbol{a}}_{\mathbf{2}}$). The chiral angle $\boldsymbol{\theta}$ is the angle between the lattice vector and the horizontal line. To build a SWCNT, the graphene sheet can be imaginary cut along the two dashed lines which stand perpendicular on the lattice vector. After rolling the cut graphene layer to a tube, the atoms of the lattice vector ($\boldsymbol{A}$ and $\boldsymbol{A'}$) laying imaginary over each other. Figure adapted from Saito *et al.* [60].

Multi-walled carbon nanotubes (MWCNTs) are built of at least two graphene layers and have diameters between 2 – 150 nm [62]. A special kind of MWCNTs are the double walled carbon nanotubes (DWCNTs) consisting of two graphene layers with a distance between the two walls of 0.33 – 0.42 nm [63], [64]. DWCNTs are in the focus of interest due to their possible usage as bearings in micro- and nanodevices [65]. The Young's modulus of MWCNTs with 1.05 TPa [66], is lower than those of SWCNTs. However, the tensile strength with 11 – 63 GPa [58] is higher than those of SWCNTs. The density of 1.74 g/cm³ [67] is also higher compared with SWCNTs. Carbon nanofibers (CNFs) have outer diameters in the range of 50 – 1000 nm [36] and appear with disordered graphene layers or a kind of herring arrangement of the graphene layers. Due to these defects in the structure, the mechanical properties of CNFs are much lower than those of CNTs. However, CNFs have a Young's modulus in the range of 6 – 300 GPa [36] and tensile strength in the range of 1.25 – 3.52 GPa [36]. The density of CNFs is nearly in the same range as for MWCNTs with 1.78 g/cm³ [44]. Therefore, CNFs are comparable with the material properties of steel but a much lower density. For comparison, steel has a density of 7.9 g/cm³, a Young's modulus between 196 – 216 GPa and a tensile strength between 360 – 510 MPa [68].

Table 2.1: Typical properties of SWCNTs, MWCNTs and CNFs taken from literature, including the range of the outer diameter, Young's modulus, tensile strength and density.

	SWCNTs	MWCNTs	CNFs
Outer diameter	1 – 2 nm [35]	2 – 150 nm [62]	50 – 1000 nm [36]
Young's modulus	1.25 TPa [57]	1.05 TPa [66]	6 – 300 GPa [36]
Tensile strength	3.6 GPa [59]	11 – 63 GPa [58]	1.25 – 3.52 GPa [36]
Density	1.33 – 1.4 g/cm³ [43]	1.74 g/cm³ [67]	1.78 g/cm³ [44]

2.1.2 Growth mechanism of carbon nanotubes

In general, CNTs as well as CNFs grow at high temperatures (600 – 1200 °C) from catalytic centers in the nm-range on a substrate in the presence of a gas mixture with a gas containing carbon. Catalytic centers for CNT growth used in most studies are made from Fe, Ni and Co [69], [70]. These transition metals are in the focus of interest due to their high carbon solubility at high temperatures and a high carbon diffusion rate [71]–[73]. However, CNT growth from several other catalysts like Mn, Mo, Pt, Pd, Sn, Mg and Al was also investigated by Yuan *et al.* [74]. Hard materials with a higher melting point as the catalytic centers such as Si, SiO_2, Al_2O_3, Ti, TiN, Ta, and W are used as the substrate for the catalytic centers [75]–[77]. The gas mixture consists of a carbon containing gas, mostly hydrocarbon (C_xH_y), a reduction gas (hydrogen or ammonia) and an inert gas as precursor, such as argon.

There are two widely-accepted growth mechanism for CNTs and CNFs growth [73]. In the tip growth model (Figure 2.3 a), the CNT lift off the catalytic center from the substrate, resulting in a CNT which grows between the substrate and the catalytic center. Whereas in the base growth model (Figure 2.3 b), the catalytic center sticks to the substrate and the CNT grow in height. Both growth models start with the presence of a gas mixture. Hydrogen reduces the metal catalysts which are assumable oxidized during exposure to atmosphere. Using nickel as a catalyst, the reduction with hydrogen can be described with the following chemical process [78].

$$\mathrm{NiO} + \mathrm{H_2} \rightarrow \mathrm{Ni} + \mathrm{H_2O} \tag{2.5}$$

The inert gas in the mixture, such as argon, does not contribute to the CNT growth directly, but it is widely used to mix it in the gas flow. The inert gas is mainly used before CNT growth starts to heat up the sample in the oven and to flush the oxygen out off in the reaction chamber. Otherwise the oxygen in the oven reacts with the samples catalyst at elevated temperatures and prevents the reduction step. Also the cooling of the sample is commonly conducted under the presence of an inert gas.

Hydrocarbon which flows over the catalytic centers, supplies the carbon source to build the CNTs. When the hydrocarbon contacts the catalytic centers, it decomposes into hydrogen (H_2) which goes into the main flow and can help reducing other catalytic centers into pure state and carbon which gets dissolved into the catalytic center. The catalytic center is made from nickel in the following example Equation.

$$2\mathrm{Ni} + C_x\mathrm{H}_y \rightarrow \mathrm{XCNi_2} + \frac{1}{2}\mathrm{YH_2} \tag{2.6}$$

After the carbon solubility limit is achieved, CNTs start to grow. CNT growth stops, when the carbon containing gas is switched off from the flow of the gas mixture.

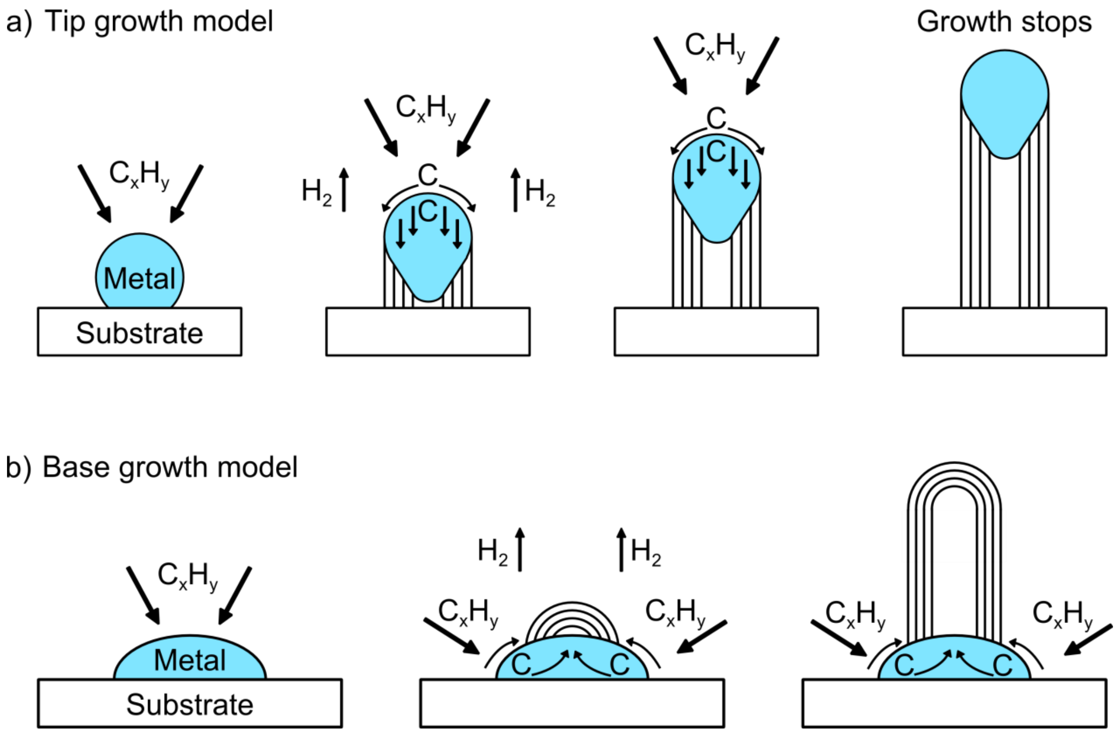

Figure 2.3: The two possible mechanisms for CNT growth, in a) the tip growth model and b) the base growth model. In both cases hydrocarbon flows over the metal catalytic centers and decomposes into hydrogen which goes back into the main flow and carbon which gets dissolved into the catalytic centers. CNTs start to grow from the catalytic centers after the carbon solubility limit of the catalysts is achieved. The two mechanisms distinguish from each other whether the catalytic center is placed on the top of the CNT or between CNT and substrate. In the tip growth model, the CNT is connected with the substrate and lift off the metal catalysts during growth. The opposite case is the base growth model, where the metal catalyst sticks to the substrate and the CNTs grow from the catalyst upward. Figure adapted from Kumar [73].

2.1.3 Catalytic centers for carbon nanotube growth

Catalytic centers are the basic component to grow CNTs. They can be imagined as ‘seed grains’ from which the CNTs grow. The following two subsections give an overview about different fabrication methods for catalytic centers and their properties during CNT growth at elevated temperatures.

Fabrication of catalytic centers

There are several manufacturing methods to produce catalytic centers in the nm-range. A simple way to manufacture catalytic centers is to sputter or evaporate a thin metal layer (thickness of 1 – 30 nm) on a substrate and expose it to a thermal treatment to break or melt the layer into tiny islands [79]. However, catalytic centers with random sizes and spaces arise with this process. A more controlled way is to use a lithography process with a mask, containing the size and location of the required catalytic centers [80]. It is also possible to use a metal-chloride solution, e.g., $NiCl_2$ solved in ethanol to cast a thin layer of the metal containing solution on a substrate. This leads to tiny islands of nickel after conducting a thermal treatment [81]. AFM-based dip pen lithography offers a possibility to determine size and location of the catalytic centers made by a metal solution [82]. Shadow nanosphere lithography offers another possibility to produce catalytic centers [83]. Therefore, as an example conducted in my work, polymer nanospheres were brought on a surface, e.g., with dip coating, resulting in arranged monolayers of nanospheres. These can be used as a mask to sputter or evaporate material through the free space between the spheres. After removing of the polymer nanospheres by etching or using a ultrasonic treatment, catalytic centers in a honeycomb ordered arrangement are left on the substrate, which can be used to grow CNTs with a honeycomb ordered arrangement [84], [85].

Another low cost process which allows covering big arrays with catalytic centers in an ordered way is a chemical nanolithography process based on amphiphilic block copolymers [86]–[92]. These copolymers self-assemble in a solvent like toluene to so-called micelles, containing a polar core which allows loading them with a metal. In this process a block copolymer, e.g., poly(styrene)-block-poly(2-vinyl pyridine) (PS-b-P2VP) mixed with toluene to achieve a 1 wt.% solution with micelles, which can be loaded with nickel (molar ratio of Ni_2^+ / vinyl pyridine = 0.5). Dip coating of the solution on substrates, such as Si or SiO_2 can be performed by dip coating. Figure 2.4 shows some typical results after dip coating varying the velocities a) – c) and using of block copolymers of different sizes. The space between the micelles gets smaller by decreasing the dip coating velocity from 10 mm/min in a) to 1 mm/min in c). Monolayers of hexagonally ordered arrays of metal loaded micelles arise. Oxygen plasma etching removes the polymer leaving the bare nickel catalytic centers on the substrate. The AFM images in d) – f) show different sizes of catalytic centers, which were achieved by using different block copolymers and nickel loading ratios. A P293-S2VP polymer-template d) resulting in diameters of about 28 nm, e) a P3808-S2VP polymer-template (loading ratio of 1) resulting in diameters of about 40 nm and f) a P3808-S2VP polymer-template (loading ratio of 2) resulting in diameters of about 68 nm. The diameter distributions in the evaluation below show nearly Gaussian distributions in all there cases. The heights of the catalytic centers range from 8 - 18 nm. Such catalytic centers can be used for the growth of CNTs [93], [94].

State of catalytic centers during growth

There is a vivid discussion which state the catalytic centers have during CNT growth [95]. However, it is favored that the catalytic centers are in a liquid phase for the growth of SWCNTs [96] due to smaller catalysts sizes whereas the catalytic centers for MWCNT growth may be in solid state due to bigger catalysts sizes [73].

Even the melting point of the used catalysts is higher than the temperature achieved in a CVD process during CNT growth, the melting point of catalytic centers in the nm-range is reduced. In general the melting point of a nanoparticle T_{mp} can be described with [97]:

$$T_{mp} = T_{mb}\left(1 - \frac{N}{2n}\right), \qquad (2.7)$$

where T_{mb} is the melting point of the bulk material, N is the amount of atoms on the surface of the nanoparticle and n the total amount of atoms of the nanoparticle.

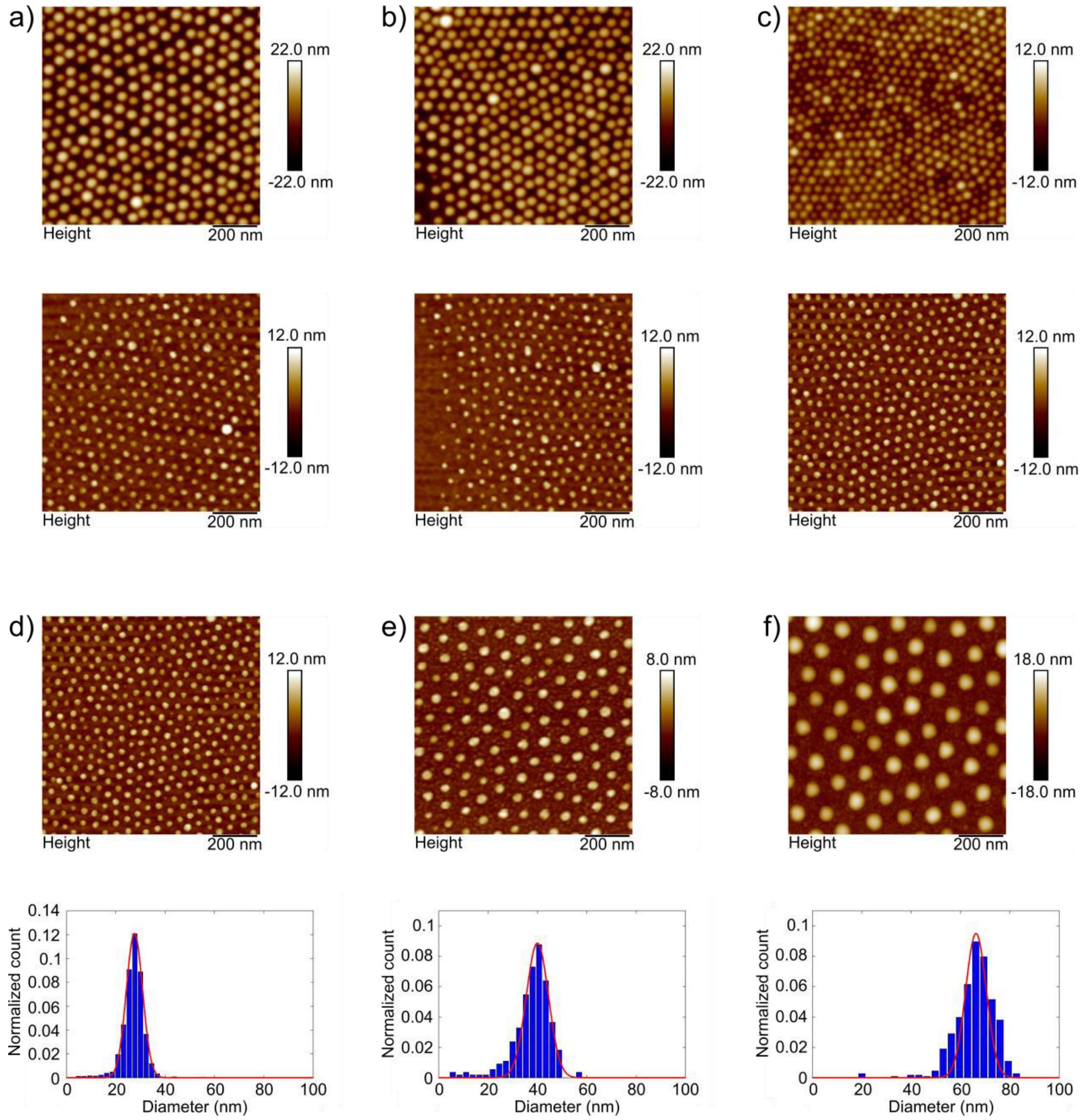

Figure 2.4: Catalytic centers achieved with a chemical nanolithography process based on amphiphilic block copolymers. AFM height images after deposition of micelles from P293-S2VP with different dip coating velocities: a) v = 10 mm/min, b) v = 5 mm/min, c) v = 1 mm/min and below their corresponding nickel catalytic centers after removing the polymer with oxygen plasma etching. It is obvious that the nanodots after plasma etching get smaller due to removal of the polymer cover. The AFM images in d) – f) show different sizes of catalysts achieved by using of different block copolymers and nickel loading ratios with d) the P293-S2VP polymer-template resulting in diameters of about 28 nm, e) the P3808-S2VP polymer-template (loading ratio of 1) resulting in diameters of about 40 nm and f) P3808-S2VP polymer-template (loading ratio of 2) resulting in diameters of about 68 nm. The diameter distributions in the evaluation below show nearly Gaussian distribution in all there cases. The heights of the catalytic centers range from 8 - 18 nm.

For a nanoparticle with a spherical shape, the relation between the total amount of atoms and the surface atoms is given by:

$$\frac{N}{n} = \frac{4d}{D}. \tag{2.8}$$

Equation (2.7) can be rewritten to calculate the melting point of a spherical nanoparticle from the diameter of the nanoparticle D and the diameter of the atoms d, which is assumed as two times the van der Waals radius r_w [97].

$$T_{mp} = T_{mb}\left(1 - \frac{2d}{D}\right) \tag{2.9}$$

The van der Waals volume (also known as atomic volume) V_w is simplified by Housecroft and Constable [98]:

$$V_w = \frac{4}{3}\pi r_w^3. \tag{2.10}$$

The atomic diameter can be calculated by rewriting Equation (2.10):

$$d_w = \left(\frac{6V_w}{\pi}\right)^{\frac{1}{3}}. \tag{2.11}$$

This leads to the following Equation depending on the melting point of the bulk material, the diameter of the nanoparticle and the van der Waals volume:

$$T_{mp} = T_{mb}\left(1 - \frac{2}{D}\left(\frac{6V_w}{\pi}\right)^{\frac{1}{3}}\right). \tag{2.12}$$

Table 2.2 gives the material properties with the melting point of the bulk material and the atomic volume of the three common catalytic centers for CNT growth with Fe, Co and Ni. The atomic diameter can be calculated by using Equation (2.11). Figure 2.5 shows the distribution of the melting point of spherical nanoparticles over the diameter of the nanoparticles using Equation (2.12) with the calculated atomic diameters. The melting points decrease with a decrease in the diameter of the spherical nanoparticles and starts gradually at ~15 nm.

Table 2.2: Material properties for Fe, Co and Ni. Including the melting point of the bulk material and the atomic volume per mole [99]. The atomic diameters were calculated from the atomic volume per mole.

Material	T_{mb} (K)	Atomic volume per mole (cm^3)	Atomic diameter (nm)
Fe	1809	7.09	0.282
Co	1768	6.67	0.277
Ni	1726	6.59	0.275

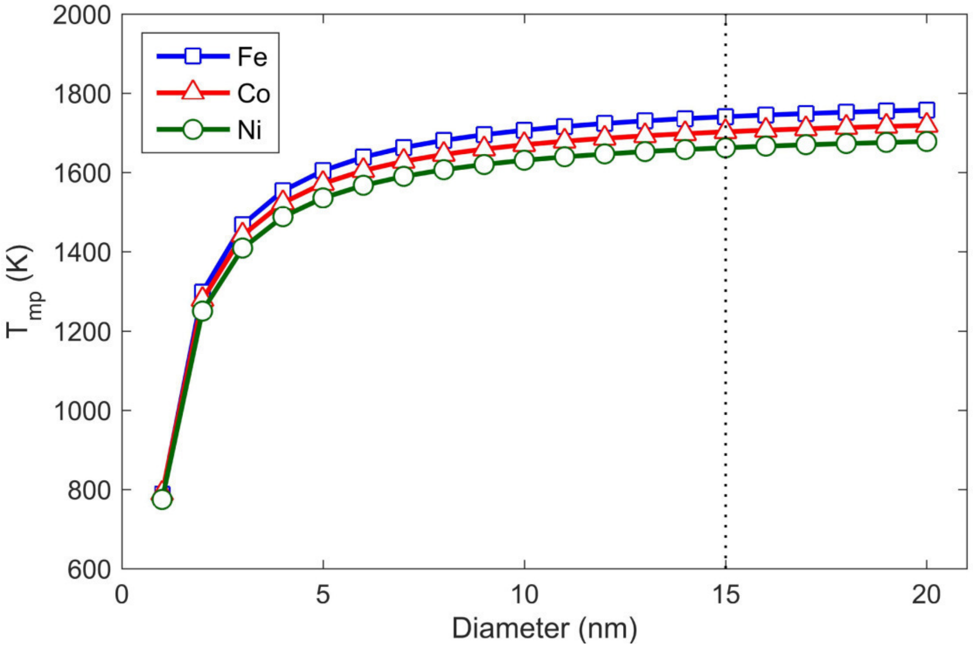

Figure 2.5: Calculated melting temperature of spherical nanoparticles of Fe (blue squares), Co (red triangles) and Ni (green circles) as a function of the diameter. The melting temperature decreases with the diameter of the spherical nanoparticles. A significant decrease starts gradually at ~15 nm.

2.1.4 Synthesis of carbon nanotubes

There are several possible processes to grow CNFs and CNTs. Arc discharge was used for the first reported CNT growth in 1991 by Iijima [56]. In this method, CNTs grow between two graphite electrodes in the arc and accumulate on the graphite cathode [100]. Another process is laser vaporization, where a graphite target gets evaporated by a laser resulting in CNTs [101]. The main processes to produce CNTs are ‘chemical vapor deposition’ and a modification with a plasma source, the ‘plasma enhanced chemical vapor deposition’. These two processes are described in detail in the following. An energy friendly way to produce CNTs and CNFs, but less investigated up to now, is flame synthesis. However, CNT or CNF growth is a challenge. Depending on the used process, there are up to eight process parameters (temperature, pressure, growth time, carbon source, precursors, flow rates, catalysts and the substrate). Using one set of working parameters and changing only one slightly might prevent CNT or CNF growth.

Chemical vapor deposition

The important process to synthesis CNTs and CNFs in research and for industrial production is chemical vapor deposition (CVD). For most lab synthesis, a horizontal placed quartz tube with a gas inlet on one end and a gas outlet on the other end (Figure 2.6 a) is used. The quartz tube is placed in a conventional oven. The oven heats the inner region of the quartz tube, where CNTs grow by temperatures of up to 500 – 1100 °C. Usually a gas mixture of three gases is used. One of them is the carbon containing gas (e.g. ethylene or methane), the second gas is for the reduction (hydrogen or ammonia) and the third gas is an inert gas (e.g. argon) to regulate the flow. Typically growth times are between several minutes up to several hours. A catalytic system is paced in the center of the quartz tube containing a substrate (e.g. Si, SiO_2, TiN or Al_2O_3) with catalytic centers (iron, nickel or cobalt) on the top. For industrial production of CNTs, a vertically placed quartz tube (Figure 2.6 b) can be used. In this case, the catalysts and the carbon can bring in gaseous or liquid shape from the top in the vertically aligned quartz tube, where the CNTs or CNFs grow and fall to the bottom in a plate. This process is more suitable for mass production in industry than for small experiments in research [102].

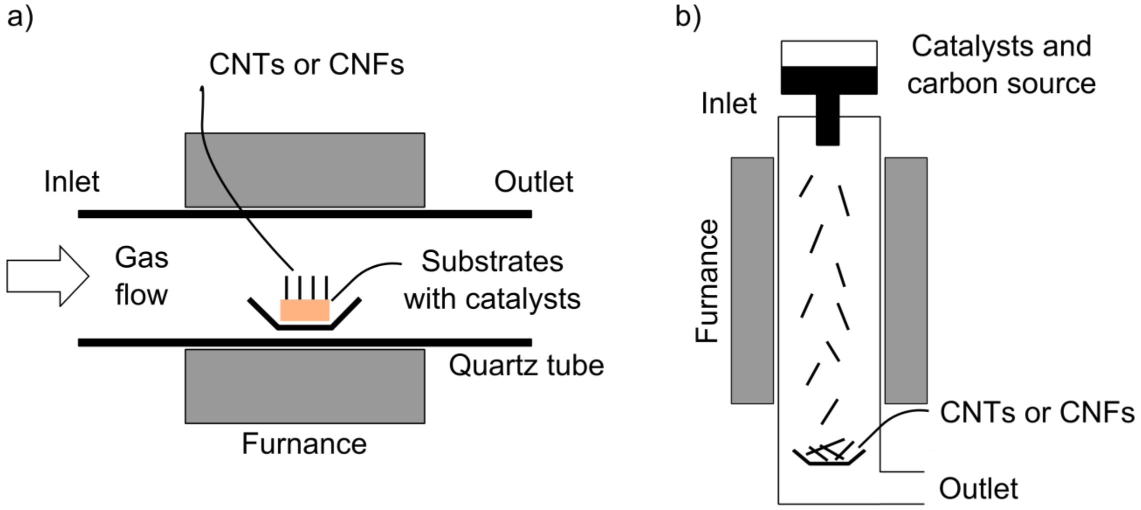

Figure 2.6: Schematic setup of CVD processes to grow CNTs or CNFs. a) A typical lab setup with a horizontal quartz tube surrounded by a furnace. The substrates with the catalysts are placed in the tube flowed by a gas mixture resulting in CNT or CNF growth. b) An industrial setup for mass production to grow CNTs or CNFs. The catalysts are brought together with the carbon source from the top into the vertically system, resulting in CNT or CNF growth, which can be collected in a plate at the bottom. Figure adapted from Szabo *et al.* [102].

Some typical CNT structures grown with the help of Sharali Malik in horizontal CVD for lab synthesis (see Figure 2.6 a) are shown in Figure 2.7. Randomly aligned CNTs growing on the ground from nickel catalysts produced by a micellar template on a silica substrate (Figure 2.7 a). The CNT diameters have a size in the range of 50 nm with lengths up to several micrometers. By the use of a special catalytic system, which is in most cases based on a thin (~1 nm) iron layer on a 10 nm Al_2O_3 layer on a silica or silicon substrate and the use of ethylene (C_2H_2) as a process gas, so called CNT-forest can be grown [103], [104]. These CNT-forests have heights up to several centimeters with a high aspect ratio. By patterning the layers with catalysts on the substrate, ordered arrays with CNT-forest pillars can be achieved [105], [106]. Figure 2.7 b) shows CNT-forest grown with CVD. The CNT-forest has a height of 150 µm, the CNT diameters vary between 30 - 70 nm. This corresponds to an aspect ratio of about 3000. At low magnifications on the microscale under the SEM, the CNTs in the forest look very aligned. However, under high SEM magnifications CNT-forests reveal disordered structures and less alignment either from the side view or from the top view.

Another possibility to grow aligned CNTs with CVD is applying an electric field between two electrodes with a small distance between 10 – 20 µm. The catalytic centers are in this case directly placed on one electrode and growing straight to the other electrode [107], [108].

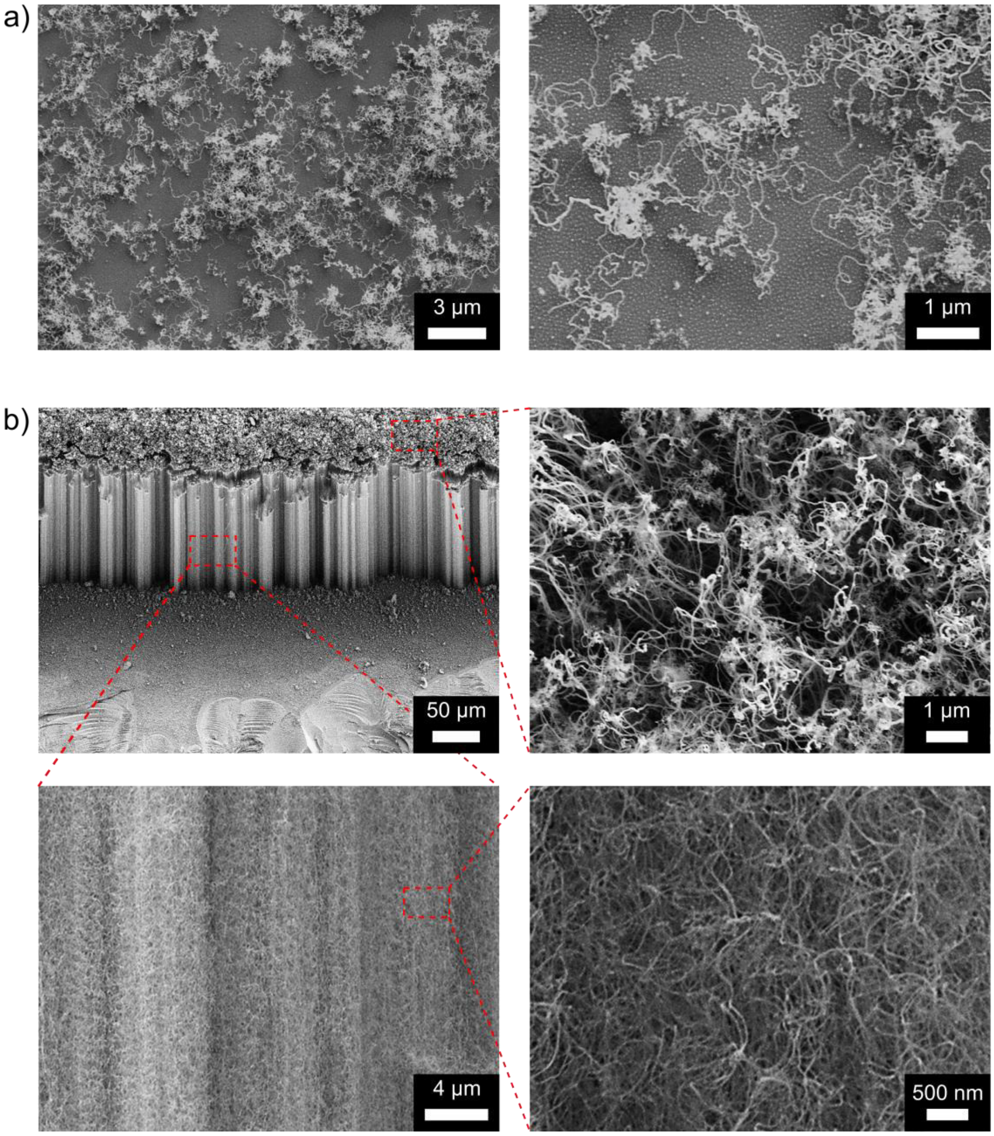

Figure 2.7: Different CNTs grown in CVD. a) With CNTs grown from nickel catalysts produced by a micellar template on a silica substrate. It is obvious that the CNTs grow on the ground in random directions. The diameters are in the range of 50 nm and with a length up to several micrometers. b) By using a catalytic system based on an Al_2O_3 substrate with Fe catalysts and ethylene as process gas, so called CNT-forests can be obtained. The CNTs in the forest have heights up to 150 µm and diameters between 30 – 70 nm, resulting in a high aspect ratio of about 3000. The CNTs look very aligned at low magnifications on the microscale under the SEM. However, at high SEM magnifications on the nanoscale, the CNTs do not reveal perfect alignment either from the side view, or from the top view.

Plasma enhanced chemical vapor deposition

A plasma enhanced chemical vapor deposition (PECVD) process is a modified CVD process to enable oriented CNT growth [52], [109], [110]. A PECVD setup (Figure 2.8 a) consists of the same infrastructure as the horizontal CVD lab setup (Figure 2.6 a), but in PECVD the sample is placed between two electrodes. Appling a high voltage and frequency leads to a plasma between the electrodes where the sample is placed. It is commonly assumed that the CNTs grow vertically aligned on the substrate due to the electric field in the PECVD [111], [112]. However, Bower *et al.* [113] tilted the substrate in the plasma resulting in aligned CNTs always perpendicular to the substrate surface. These results contradict the previous assumption. The aspect ratio for CNTs grown with PECVD is normally smaller than those who grown with CVD. Figure 2.8 b) shows a result for CNTs grown from a 20 nm nickel layer on a silicon wafer with 1 µm SiO_2 in PECVD performed by Oleg Ageev and Oleg Il'in with applying a plasma of 45 W, resulting in vertically aligned CNTs. Additionally, CNT growth via PECVD offer the advantage that it can also work under lower temperatures (e.g. 120 °C) compared with CVD [114]. This allows CNT growth on temperature sensitive substrates. Therefore, CNT growth with PECVD can be very promising to produce field emitter for displays [109]. Additionally, vertically aligned growth of CNTs with PECVD is very promising for CNT based dry adhesives. Compared with randomly aligned CNTs, vertically aligned CNTs with a low aspect ratio cannot stick together, as shown in Figure 2.8 b) which leads not to a reduced adhesion force due to agglomeration [19].

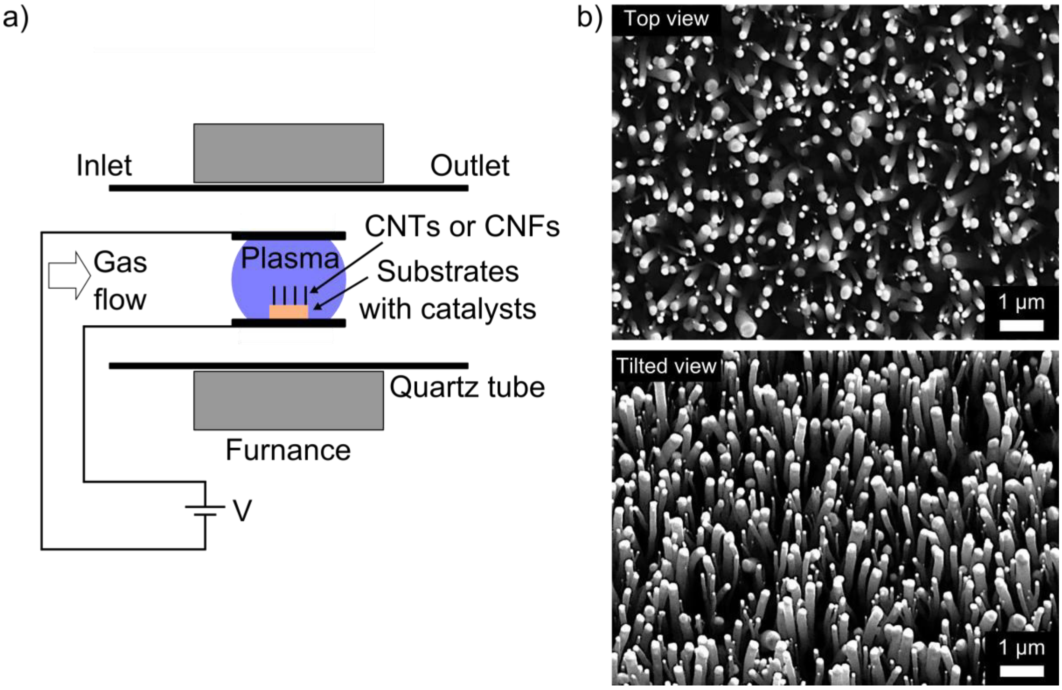

Figure 2.8: CNT growth with PECVD. a) A schematic setup of a PECVD process to grow CNTs or CNFs. In general PECVD is the same process as CVD but with a possibility to apply a plasma in the region where the sample is placed. The produced CNTs with PECVD have lower aspect ratios than CNTs produced with CVD. b) SEM images, with top view and a 30° tilted view, shows CNTs grown in PECVD with diameters between 60 – 200 nm and a height of about 2 µm. The CNTs grow vertically aligned.

Flame synthesis

Beside CNT and CNF growth using the well-established processes with arc discharged, laser vaporization, CVD and PECVD, another process based on an open flame which got less attention up to now exist. Several groups investigated CNT and CNF growth from flame synthesis [115]–[121]. In the flame synthesis only an open flame, e.g., from ethanol as fuel is used to grow CNTs or CNFs.

This alternative process is surprisingly simple and does not need complex infrastructure or lab equipment. An open flame offers the required temperature and acts as the carbon source.

However, these processes are not easy to control which might be the reason why up to now very few studies on this topic were reported. However, flame synthesis benefit from very low process costs. It does not need electricity to heat an oven or for controllers to regulate the gas flow. A standard experiment with flame synthesis is in the range of several minutes whereas with CVD it can last several hours. Therefore, flame synthesis is an energy friendly way to grow CNTs or CNFs and should get more attention. MWCNTs were grown from Li and Hsieh [115] using a paraffin wax candle and Hsieh *et al.* [116] from a Bunsen burner. Pan and Bao [119] grew CNTs and CNFs by using an open ethanol flame. Bao and Pan [117] used an ethanol flame with a DC voltage of 25 V around it resulting in aligned CNTs and CNFs. Zhang and Pan [120] used an open ethanol flame with an arranged magnet above the flame which is shown in Figure 2.9 a). An aluminum flat protects the magnet from damage and losing his performance at elevated temperatures. The magnetic field leads to aligned CNTs and CNFs. A typical result of CNFs produced by flame synthesis using an open ethanol flame without a magnet is shown in Figure 2.9 b).

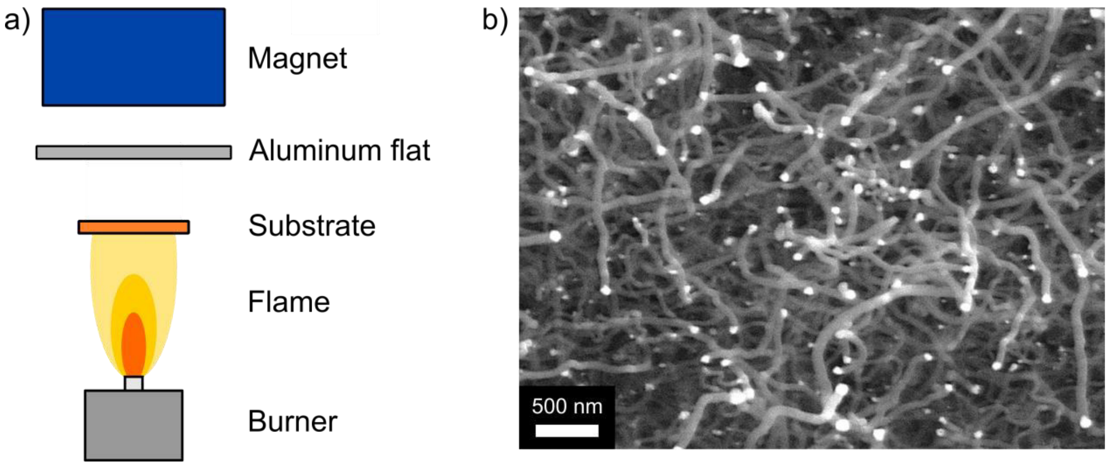

Figure 2.9: Flame synthesis of CNTs/CNFs. a) A schematic setup of a flame synthesis process to produce CNTs and CNFs adapted from Zhang and Pan [120]. A burner with a carbon containing gas or fluid generates a flame. The sample is placed directly in the hot zone of the flame. In the setup from Zhang and Pan a magnet is used to align the CNTs during growth. An aluminum flat protects the magnet from the flame. b) A result of CNTs and CNFs grown in an ethanol flame on a copper substrate with nickel-catalysts.

2.2 AFM based adhesion measurement

The atomic force microscopy (AFM) or sometimes also called scanning force microscopy (SFM) was invented by Binnig *et al.* in 1986 [122] and is a powerful tool to investigate the micro- and nanoscale world. This Section gives at first an overview about the AFM applications and the working principle. AFM based adhesion detection is introduced in this Section, including the fabrication of customized AFM cantilevers mounted with silica spheres or debris particles from rock materials. The obtained force-distance diagrams from AFM based adhesion measurement are discussed including the calculations of the adhesion properties.

2.2.1 AFM working principle

The AFM is a versatile tool which can work under different environments such as ambient conditions, gases, liquids or in vacuum and is mainly used to characterize surface topographies [123]. Nevertheless, several other properties in the micro- and nanoscale range such as adhesion [124], friction [125], magnetism [126] or binding forces in biology [127] can be investigated, too. AFM based dip-pen lithography enables structured writing of, e.g., metal salts on flat surfaces. Also surface modifications and molecular manipulations are possible [128]–[130]. However, the AFM is mainly used for topography measurements. A cantilever with a tip to conduct the measurement, in most cases a sharp pyramid structure (Figure 2.10), is placed over the sample under investigation. The cantilever is brought into contact with the surface and scanned over the surface directly (contact mode). In this case a deflection of the cantilever results during interaction with the surface. Another possibility is to oscillate the cantilever over the surface and measure the amplitude (tapping mode). The sample is placed on a scanner-table, which can move in three directions. A laser beam is focused on the backside of the cantilever and the reflected beam is guided to a photo-diode and enables the detection of the deflection of the cantilever. The deflection of the cantilever is small compared with its length. The signal from the piezo table and the photo-diode goes through a loop to a computer to visualize the results of the measurement on a screen. In case of a topography measurement, lines are scanned in x-direction and put together for a full image of the topography.

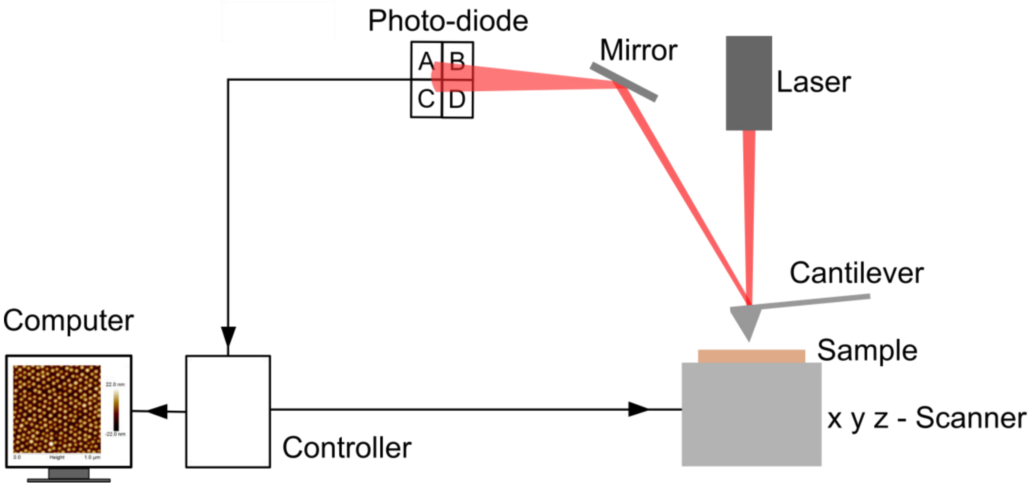

Figure 2.10: Schematic setup of the AFM working principle. The sample is placed on a table, which is movable in three axes. A sharp tip on a cantilever interacts with the sample surface, resulting in a bending of the cantilever. A laser is focused on the cantilever and a photo-diode receives the reflected laser beam to detect the bending of the cantilever. The signal goes over a loop to a computer and the signal is visualized on a screen. Figure adapted from [131].

2.2.2 AFM adhesion measurement

The AFM setup can be also utilized for adhesion measurements. For that the cantilever is scanned in z-direction and the deflection from the cantilever is used to calculate the force between tip and sample by using the spring constant of the cantilever. Figure 2.11 shows a force distance diagram of an adhesion force measurement. In this case, a pyramidal shaped tip on an AFM cantilever is used to approach a flat surface (a-b). The tip gets attracted to the surface (b-c) due to van der Waals forces which is called ‘snap-in’. After the snap-in, the preload is applied causing a linear deflection of the cantilever (c-d). The complete approach is called trace, the retraction from the surface is called retrace. In the retrace line, at first a linear deflection of the cantilever in opposite direction arise (d-e), resulting in a ‘snap-out’ (e-f). Finally, the cantilever drives upwards to leave the surface (f-g). After reaching the start position again, the adhesion measurement cycle is finished.

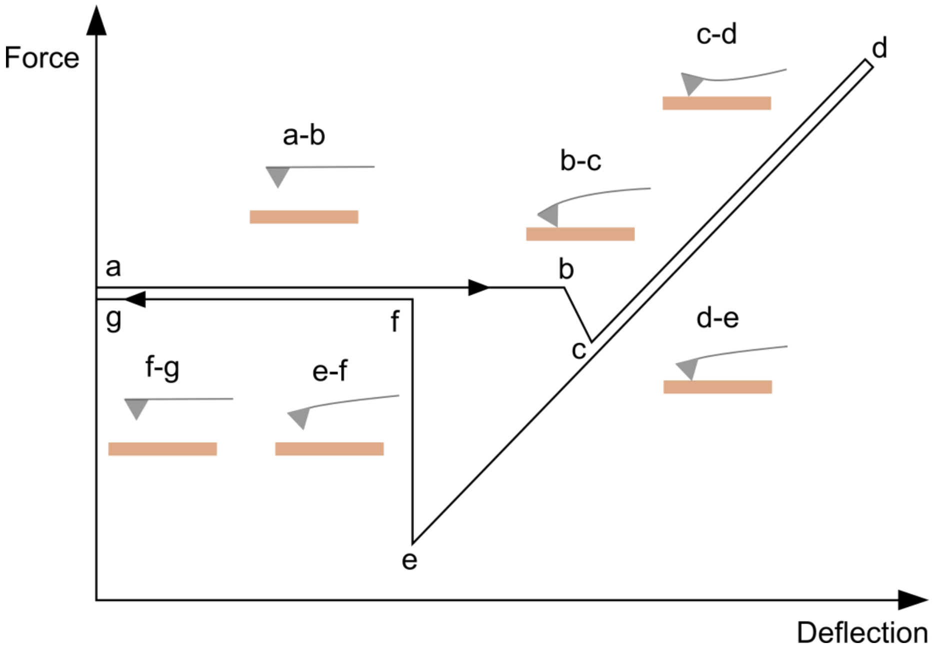

Figure 2.11: Theoretical force distance diagram obtained with a sharp tip on an AFM cantilever interacting with a flat surface. From a-b, the cantilever approaches the surface and gets attracted (b-c) to the surface by van der Waals forces. Followed by a linear deflection of the cantilever caused by the preload (c-d). The way back is described by a linear deflection of the cantilever in opposite direction (d-e), where the maximum force in negative direction at point e is the adhesion force. The diagram from e-f describes the pull-off, which means that the cantilever tip suddenly jumps off the surface and goes back to a relaxed position. Finally, the cantilever drives upwards away from the surface f-g to finish the adhesion measurement cycle. Figure adapted from [132].

2.2.3 Fabrication of AFM cantilevers for adhesion measurements

AFM cantilevers with sharp tips [133] for scanning the topography or measuring physical properties are commercially available. However, customized cantilevers for special measurements have to be self-produced. Therefore, tipless cantilevers built the basis to equip the cantilevers with customized setups. Göring *et al.* [134] used 3D laser writing to produced different polymer based geometry setups on bare AFM cantilevers. Schmutz *et al.* [135] and Röhrig *et al.* [32] glued spheres to bare cantilevers to measure topography, friction and adhesion. To transfer micro-objects for measurements on bare cantilevers, a micro-manipulation unit integrated in an optical light microscope is used. Figure 2.12 shows a schematic setup for the micro manipulation unit integrated in an optical light microscope and Figure 2.13 shows an optical image of the micro manipulation unit with the light microscope and the glass needle. At first a glass slide is subdivided into in four arrays. On the first array a tiny droplet (diameter < 100 µm) of a two component glue with a drying time of about 90 minutes is placed directly on the glass slide. The second array stays free and serves later for the deposition of a tiny droplet (1 µL) of isopropanol. The tipless cantilever is placed on the third array. On the fourth array the micro objects which should be transferred to the cantilever are placed. In this study, this can be either tiny debris parts of meteorites in the µm-range or silica spheres with a diameter of 20 µm. In the case of the meteorites debris parts, with a originally size of ~2 x 2 x 2 mm³, they are broken mechanically to achieve debris parts with a size in the range of 100 x 100 x 100 µm³. The debris parts of the meteorites are placed directly on the glass slide. For the silica spheres, a tiny droplet (2 µL) of an isopropanol solution with the spheres are placed on the glass slide. The isopropanol evaporate and leave the silica spheres on the glass slide. This drying process can be accelerated through heating by increasing the intensity of the microscope light. Once everything is placed on the glass slide, the transfer process can be started. First, the very sharp glass needle of the micromanipulator with a diameter of 10 µm at the end, which is moveable in three directions, is dipped only with the end part into the two component glue. The glass needle with the glue on the end is now transferred to the bare cantilever and brought in contact with the area on the cantilever where the micro object should be placed later, leaving a tiny micro droplet of glue on the cantilever. After this step, the micromanipulator needle is contaminated with glue and has to be cleaned before transferring the micro objet. Therefore, a tiny droplet of isopropanol (~1 µL) is placed on the second array of the glass slide and the micromanipulator needle is dipped in and out until the glue on the needle is dissolved completely.

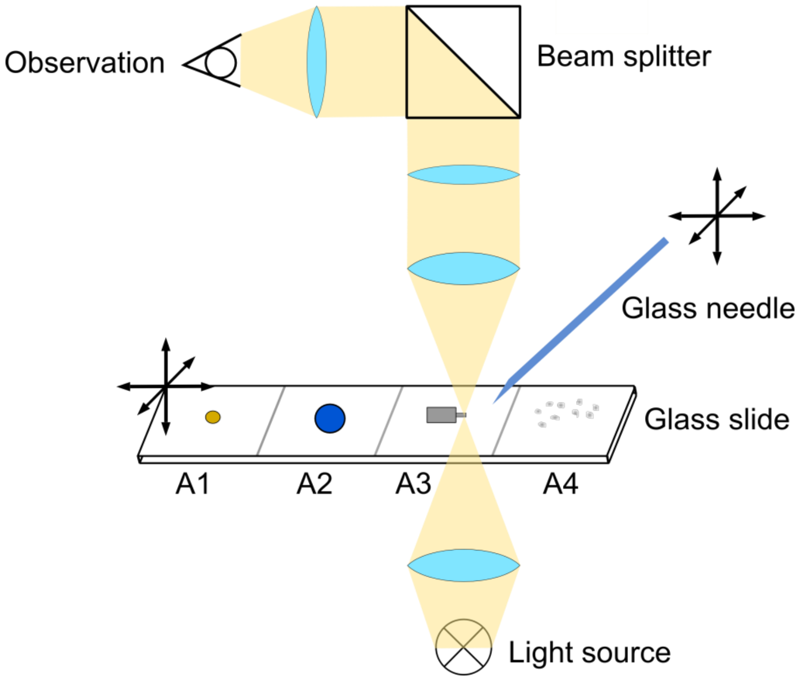

Figure 2.12: Schematic setup for the fabrication of customized AFM cantilevers. The glass slide is subdivided into four arrays, with a tiny droplet of a two component glue on A1, a droplet of isopropanol on A2, the bare AFM cantilever on A3 and either silica spheres or debris parts of meteorites on A4. The glass slide is placed on a microscope table which is moveable in three axes. A glass needle is used for transferring glue or an object to mount on the cantilever which is also movable in three axes. The micromanipulation process can be investigated through the optical light microscope.

This process can be observed under the light microscope. Now, the micromanipulator needle can be moved to the fourth array to collect either a silica sphere or a debris part of a meteorite by electrostatic forces. The needle with the micro object can now be transferred to the third array with the cantilever. The micro object gets deposited over the glue area on the cantilever and the needle has to be retracted. The customized setup can be used for the adhesion measurements after successfully drying of the built cantilever of about 90 minutes. Figure 2.14 a) and b) show a bare cantilever under different magnifications before transferring a micro object to it. Figure 2.14 c) shows a cantilever mounted with a 20 µm silica sphere and Figure 2.14 d) shows a cantilever mounted with a tiny debris part of a Chelyabinsk meteorite (chondrite LL5) with a size of 60 x 60 x 60 µm³.

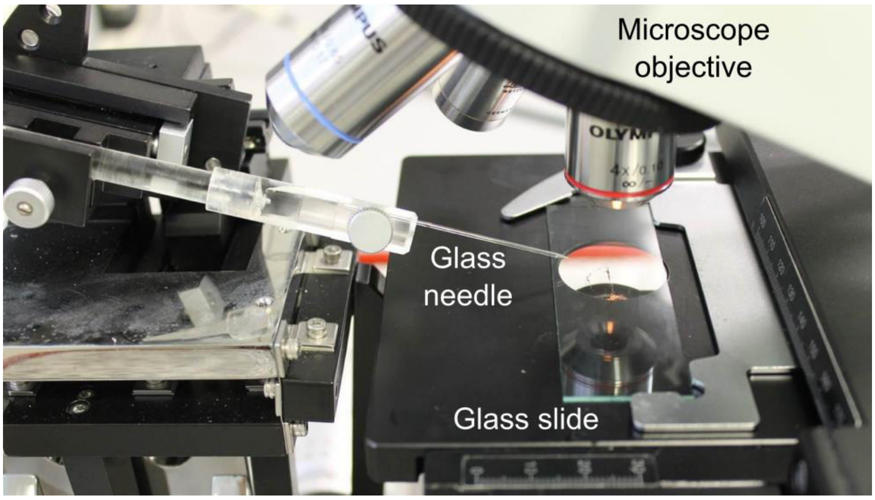

Figure 2.13: Picture of the micro-manipulation unit with the glass needle and the glass slide which are both movable in three axis. The manipulation process can be observed with the light microscope under a magnification of 4x, 20x and 40x.

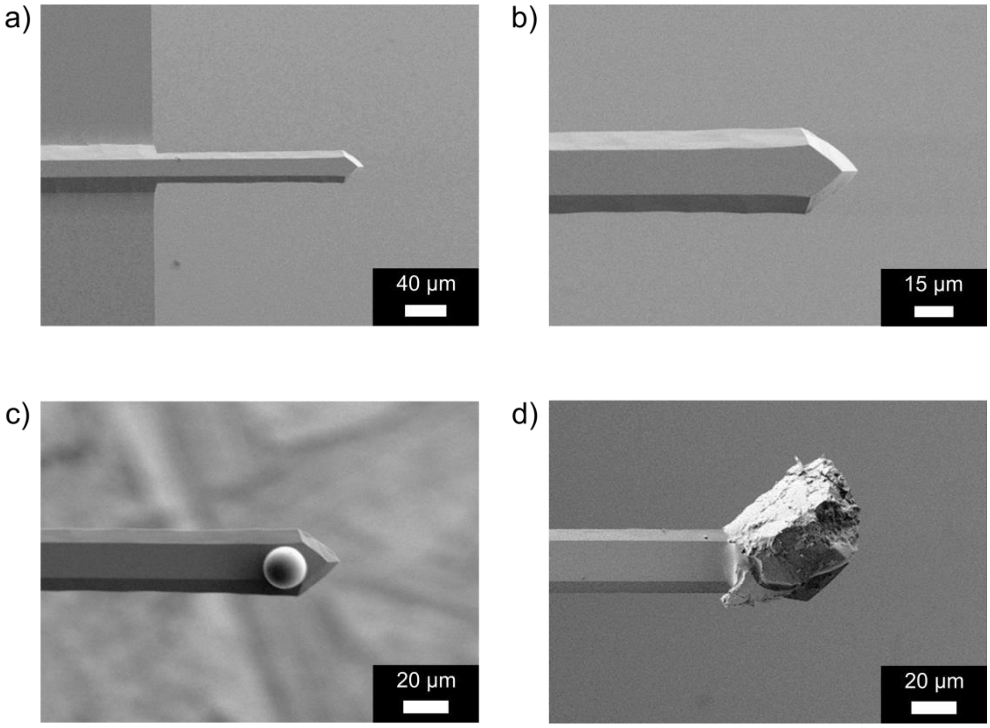

Figure 2.14: Fabrication of customized AFM cantilevers for adhesion measurements. a), b) Bare AFM cantilevers, who serve as the basis for the micro objects transferred by the micromanipulator. c) The micro objects are in this study either a silica sphere with a diameter of 20 µm or d) a debris part of a meteorite, in this case a debris part of a Chelyabinsk meteorite (chondrite LL5) with a size of ~ 60 x 60 x 60 µm³.

One of the produced cantilevers with a 20 µm silica sphere was used for a sequence of optical images showing the approach and touchdown of the silica sphere with the surface during an AFM adhesion measurement cycle from the side view (Figure 2.15).

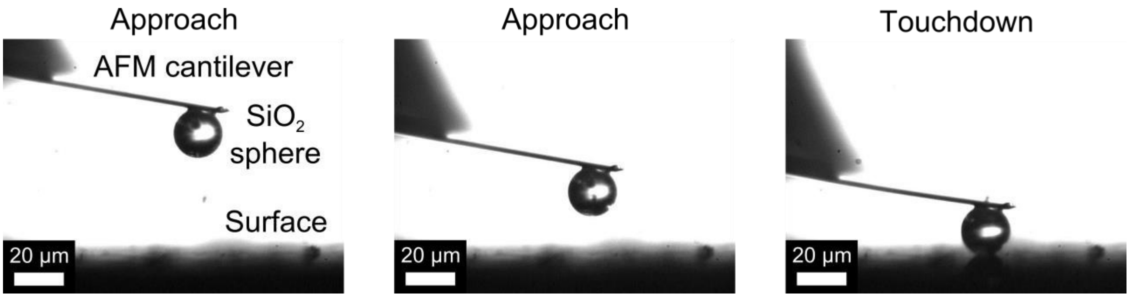

Figure 2.15: Approach to the surface of a customized AFM cantilever. The sequence of optical images showing an AFM cantilever with a 20 µm silica sphere approaching and touching a surface during an AFM adhesion measurement from the side view.

2.2.4 Adhesion force and energy calculation from force-distance diagrams

Adhesion force and energy can be calculated from the force distance diagrams. Figure 2.16 shows a force distance diagram from an AFM adhesion measurement obtained between an AFM cantilever mounted with a 20 µm silica sphere and a flat silicon surface. The two measurements lines are trace $F_t(z)$ (blue dashed line), describing approach, touch and press into the surface. The other line is retrace $F_r(z)$ (red solid line), describing the way back with the information about the pull of from the surface containing the adhesion force and energy.

The maximum value of trace and retrace are identical and describe the preload force:

$$F_{pre} = max\{F_t(z)\} = max\{F_r(z)\}. \tag{2.13}$$

If the maximum distance z_3 is known, the preload force can also be calculated with:

$$F_{pre} = F_t(z_3) = F_r(z_3). \tag{2.14}$$

The adhesion force is defined as the minimum absolute force value of the retrace line:

$$F_{adh} = |min\{F_r(z)\}|. \tag{2.15}$$

The adhesion energy is defined as the area between the zero line $(F = 0)$ and retrace. The calculation can be simplified by only considering the area where the retrace line are not zero but negative $(z_1 - z_2)$.

$$E_{adh} = \left| \int_{z_1}^{z_2} F_r(z)\, dz \right| \tag{2.16}$$

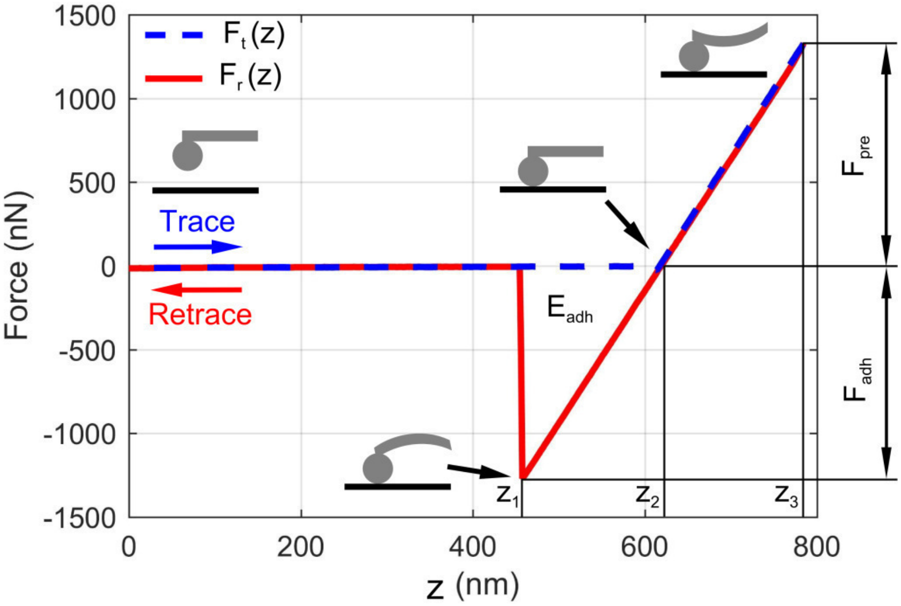

Figure 2.16: Experimental force distance diagram, obtained from a 20 µm silica sphere on an AFM cantilever interacting with a flat silicon surface. The diagram consists of trace (blue dashed line) which describes the silica sphere approaching the surface, touching the surface and being pressed in the surface. Due to the hard silicon surface, the silica sphere cannot stamp into the surface, resulting in a deflection of the cantilever. The retrace (red solid line) describes the way back including the adhesion force leading to a deflection of the cantilever in the opposite direction. The adhesion energy, needed to pull the sphere from the surface, is the area between the zero line and retrace.

2.2.5 Adhesion force and energy calculation per area for spheres and stones

Adhesion forces and energies can be calculated from the force distance diagrams obtained from AFM measurements as described in Chapter 2.2.4. However, it is difficult to compare the resulting adhesion forces and energies. Only when the same sphere on a cantilever, or a sphere with identical size is used, the results are comparable. This is maybe possible for the silica spheres, but for debris parts of stones, it is nearly impossible. To obtain comparable results, the adhesion forces and energies should be referred to an area. This area is defined as the projected area A_p (Figure 2.17), where CNTs contact the sphere or debris part of a stone. In the case of a sphere, the projected area can be directly calculated via geometrical relations by knowing the diameter or radius of the sphere and the penetration depth t. The penetration depth can be obtained from the force distance diagrams (see Figure 2.16), in case that the surface is soft and gets mostly compressed by the sphere, I, therefore, made the assumption:

$$t \approx z_3 - z_2. \tag{2.17}$$

Using the radius r of the sphere and the penedration depth, leads to the following relation containing the radius r_p of the projected area:

$$r^2 = (r - t)^2 + \left(r_p\right)^2. \tag{2.18}$$

Rewriting Equation (2.18) to the radius of the projected area leads to:

$$r_p = \sqrt{t(2r - t)}. \tag{2.19}$$

The projected area by itself is defined as:

$$A_p = \pi {r_p}^2. \tag{2.20}$$

Including Equation (2.19) into Equation (2.20) gives the projected area dependence from the radius of the sphere and the penetration depth:

$$A_p = \pi t(2r - t). \tag{2.21}$$

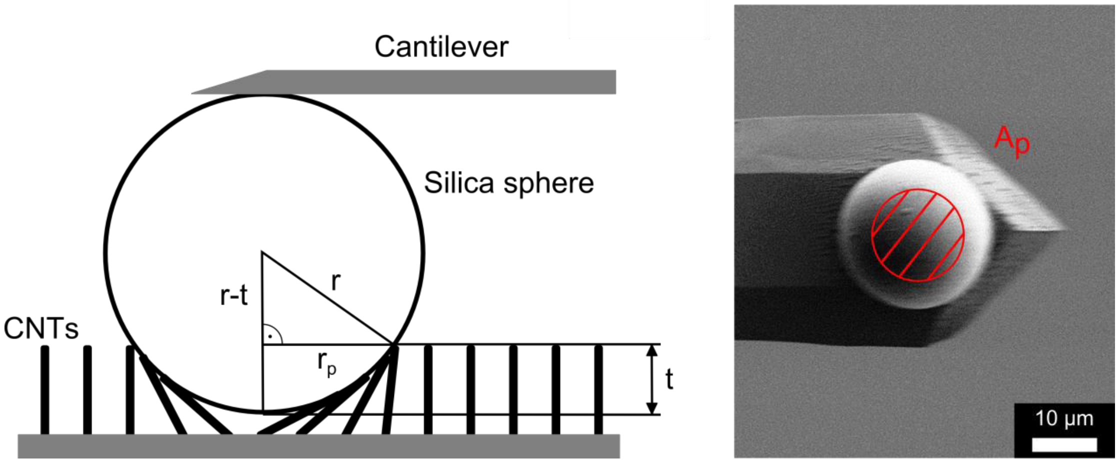

Figure 2.17: Projected area of a silica sphere mounted to an AFM cantilever. The projected area can be calculated via geometrical relations from the diameter of the silica sphere and the penetration depth from the force distance diagrams. The projected area is exemplified in the SEM image (right side) for a 20 µm silica sphere on an AFM cantilever.

In the case of debris parts of stones on a cantilever, the projected area cannot be calculated directly due to inhomogeneous geometries. In this case an approximation was used to determine the projected area from two SEM images. Therefore, SEM images of the debris part of a stone were recorded from two side views shifted by 90° from each other, which is depicted in Figure 2.18 a) and b). By knowing the penetration depth, the two lengths of each side (s_1 and s_2) of the projected area, which is defined as the rectangle in Figure 2.18 c) and d), can be determined from the SEM images.

$$A_p \approx s_1 s_2 \tag{2.22}$$

By using the projected area, the adhesion force and energy can be referred to an area, with σ_p the adhesion force per area and ξ_p the adhesion energy per area.

$$\sigma_p = \frac{F_{adh}}{A_p} \tag{2.23}$$

$$\xi_p = \frac{E_{adh}}{A_p} \tag{2.24}$$

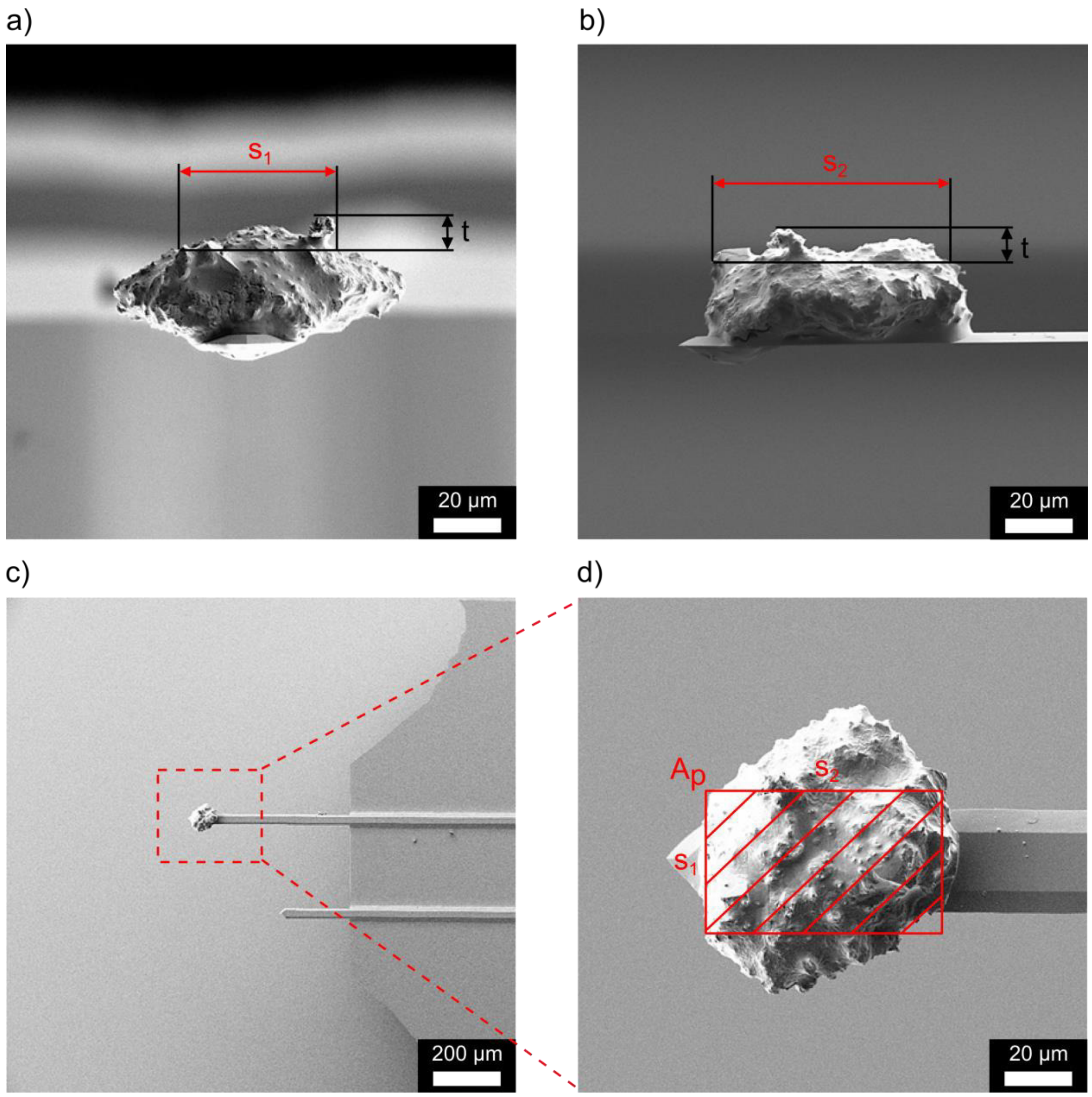

Figure 2.18: Determination of the projected area from SEM images for debris parts of stones glued on cantilevers by using the penetration depth. a), b) The lengths s_1 and s_2 can be determined from two SEM images of the two side views. c), d) The projected area refers to the top view of the stone on a cantilever, which is pictured as the shaded area.

3 Dry adhesives from CNFs for space technology

Low- or zero gravity is a fundamental issue in space technology and makes especially attachment in space a challenge. Working outside space crafts or space stations require handles or jetpacks for the locomotion of the astronauts. Landing units are restricted to a sufficient surface gravity, as it is found on larger astronomical objects and planets like Moon or Mars. However, in case of small meteorites, asteroids, and comets, mechanical attachment systems are unavoidable due to extremely low gravity. Transferring the attachment ability of the gecko to space with CNF based dry adhesives can solve such problems. This Chapter deals with the rigorous investigation of the adhesion properties of CNFs at harsh conditions as in space.

3.1 Motivation for attachment in space

The landing of space probes on other planets, moons, comets, asteroids, and meteorites is one of the biggest challenges for mankind to investigate space and reveal its secrets, such as if life exists or existed outside Earth. One of the greatest achievements in space history and for mankind was the manned landing of the lunar module Eagle with the Apollo 11 mission on the Earth Moon in the year 1969 [136]. Later on, rovers landed on Mars in 2004 and 2012 with the Mars Exploration Rover Mission [137] and the Mars Science Laboratory [138]. These missions benefit from a sufficient gravity on the surface of the Moon with 1.62 m/s^2 [139] and of the Mars with 3.71 m/s^2 [140]. Therefore, it was not necessary to mount attachment units on the landers. However, landing on small bodies such as comets, asteroids, and meteorites is a challenge due to their low gravity. One famous example was the Philae lander of the Rosetta mission [141], which landed in 2014 on the comet 67P/Churyumov-Gerasimenko with a surface gravity of only 0.0003 m/s^2 [142]. Therefore, the landing module Philae was designed to attach mechanically with the firing of an anchoring harpoon and three ice-screws on each landing foot. However, these mechanical attachment systems did not reveal the desired fixation of the lander on the surface. Due to the low surface gravity, Philae bounced two times over the comets surface before it stopped on a shadow cliff wall [143]. The stopping position in the shadow was not the perfect landing area for its solar modules to collect sunlight.

A mechanical attachment system requires a surface geology for which it was designed. Therefore, proper geological information about the landing place is needed which is in most cases not known at the planning of such a long distance mission. Consequently, an attachment system that can perform in space and cope with different surface morphologies and materials is desirable to improve the landing and subsequently enhance the success of such space missions. The two surface materials of interest are rocky material and ice, which are the two main components of comets. Figure 1.4 shows a vision of a model of a landing unit which might cope with different underground materials, such as a meteorite and an ice surface.

Additionally, CNT based dry adhesives can be used for manufacturing of satellites to connect their different components like cables, sensors and protection foils. Due to the extreme space temperatures, satellites are covered with insulation foils for thermal control and to protect the sensitive on-board instruments [144], [145]. Figure 3.1 shows the ‘Trace Gas Orbiter’ satellite during manufacturing stage with some typical insulation foils [146]. Adhesives are the method of choice to attach the insulation foils on satellites compared to mechanical connections like screws due to their low weight. However, the adhesives have to survive at least one decade under harsh conditions in space. Therefore, dry adhesives which can cope with these conditions over years without failure would improve satellites and possibly their lifetime.

Figure 3.1: Manufacturing of the satellite ‘Trace Gas Orbiter’ at Thales Alenia Space. The satellite is covered with insulation foils for thermal control. Reprinted with permission from Thales Alenia Space [146].

Another possible application for the need of dry adhesives in space, which can be realized for space missions very quickly, is inspired by the Cassini mission [147], which investigated the Saturn rings, which consist of tiny particles [148]. CNT arrays might be used as a catcher to collect such stardust and micrometeorites, which will stick to the CNT arrays for further investigations direct on the space probes or for transportation to Earth. Therefore, CNTs seem to be the material of choice due to their outstanding material properties (see Chapter 2.1.1). Additionally to a temperature stability of up to 2800 °C in vacuum [46], CNTs have a radiation resistance [149], which makes them a promising material for long term space missions in areas with high radiation, such as the Van Allen belts surrounding Earth [150] or Jupiter [151].

3.2 Micrometeorites on AFM cantilevers

For the AFM based adhesion measurement between debris parts of meteorites and CNT arrays, tipless cantilevers were mounted with micro-meteoritic particles. For the study, three meteorites (Figure 3.2) were purchased from Minerando GmbH; a 197 mg Chelyabinsk meteorite (chondrite LL5) [152], a 11 mg Mars meteorite (NWA 6963) [153] and a 13 mg Lunar meteorite (NWA 4881) [154]. The purchased debris parts of the meteorites had sizes of several millimeters.

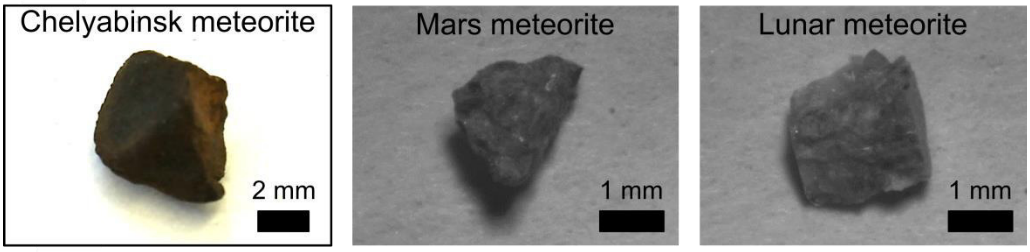

Figure 3.2: Debris parts of meteorites used for adhesion measurements before mechanically breaking into smaller parts for the measurements. The pictures show a 197 mg Chelyabinsk meteorite (chondrite LL5) [152] on the left side, a 11 mg Mars meteorite (NWA 6963) [153] in the center and a 13 mg lunar meteorite (NWA 4881) [154] on the right side. The debris parts of the meteorites had sizes of several millimeters.

These meteorites were mechanically crushed to achieve debris parts of meteorites with sizes between 60 µm and 120 µm. The debris parts were transferred and glued to tipless cantilevers utilizing a micro-manipulation unit as described in Chapter 2.2.3. Figure 3.3 a) shows the schematic setup of the AFM based measurement principle with the micro-meteorite on the cantilever. Figure 3.3 b) shows the Mars micro-meteorite on the cantilever used for the adhesion measurement with a size of 100 x 105 x 45 μm^3. The lunar micro-meteorite had a size of 100 x 90 x 40 μm^3 (Figure 3.3 c) and the micro-meteorite from Chelyabinsk had a size of 70 x 65 x 35 μm^3 (Figure 3.3 d). A SEM from Zeiss (SUPRA 60 VP) was used to image the meteoritic particles on AFM cantilevers. Normally, non-conductive samples, such as rock material are sputtered with a thin (~10 nm) silver layer to make the surface electrically conductive for SEM investigations in order to avoid charging effects. In this case, the debris parts of meteorites were investigated by SEM without any sputtering to avoid changing their surface chemistry, which might influence the adhesion measurements. Therefore, very low subsequent acceleration voltages (1 – 1.5 kV) were used and the distance between detector and sample was adjusted to 5 – 7 mm.

AFM offers the possibility to calculate the mass of the debris parts of the meteorites mounted on the cantilevers from the resonance frequency of a tipless cantilever before and after mounting a meteoritic particle to it. The resonance frequency f_0 for a rectangular cross section cantilever can be expressed by the Equation [155]:

$$f_0 = \frac{1}{2\pi}\sqrt{\frac{k}{M + m_{eff}}}, \tag{3.1}$$

with the cantilever spring constant k, the additional mass M placed at the cantilevers end and the effective mass m_{eff}. For the used cantilever, the relation between the effective mass and the 'real' mass m of the cantilever is $m_{eff} = 0.24m$. To calculate the mass M of the meteoritic particle, Equation (3.1) can be rewritten to:

$$M = \frac{k}{(2\pi f_0)^2} - m_{eff}. \tag{3.2}$$

Using the thermal tune method [156], a spring constant of 0.4 N/m was determined. The resonance frequency of a tipless AFM cantilever ($M = 0$) was measured to 14.82 kHz (Figure 3.4 a), resulting in an effective mass of 46 ng and a real mass ($m = m_{eff}/0.24$) of 192 ng. A resonance frequency of 2.53 kHz (Figure 3.4 d) was measured for the Mars meteorite on the cantilever from Figure 3.3 b) leading to a calculated mass of 1.53 µg. The lunar meteorite on the cantilever (Figure 3.3 c) had a resonance frequency of 3.02 kHz (Figure 3.4 c) leading to a calculated mass of 1.07 µg. The meteorite from Chelyabinsk on the cantilever (Figure 3.3 d) had a resonance frequency of 4.76 kHz (Figure 3.4 b) leading to a calculated mass of 0.40 µg. Table 3.1 shows an overview of the three meteoritic probes with their respective properties.

Table 3.1: Specification and properties of the used micro-meteorites, mounted on AFM cantilevers.

	Mars meteorite	Lunar meteorite	Chelyabinsk meteorite
Specification	NWA 6963	NWA 4881	chondrite LL5
Dimension (µm³)	100 x 105 x 45	100 x 90 x 40	70 x 65 x 35
Resonance frequency (kHz)	2.53	3.02	4.76
Mass (µg)	1.53	1.07	0.40

3.3 AFM measuring setup for high and low temperatures and fabrication of CNTs for the measurement

An AFM measurement setup including a Peltier element (Figure 3.5) was used to conduct adhesion measurements at low and high temperatures. The required temperature range from -20 °C to +240 °C was achieved with two different Peltier elements. A Peltier element ‘Dimension Cooler’ from Bruker with a maximum working range from -40 °C to +100 °C was used for measurements under +20 °C and a Peltier element “Dimension Heater” from Bruker with a maximum working range from +20 °C to +250 °C was used for all measurements above +20 °C.

The sample under test with the CNT arrays was placed on top of the Peltier element. The setup around the Peltier element has an inlet and an outlet for a fluid to regulate the temperature (Figure 3.5 a). In this setup deionized water at room temperature (~20 °C) was used for the Dimension Heater and deionized water cooled with ice to ~0 °C was used for the Dimension Cooler. Another pipe which is connected to the setup of the Peltier element offers the possibility to flood the area around the sample with gaseous dry nitrogen which is necessary for measurements at low temperatures (<0 °C). In this way, condensation of water from the air on the samples surface and subsequent influence on the adhesion measurement is prevented. A special AFM cantilever holder based on a flexible silicone rubber sealing (Figure 3.5 b) was used to achieve a closed system for the measurement allowing production of customized atmospheres (e.g. a dry nitrogen atmosphere). The ramp frequency was set to 1 Hz and kept constant for all adhesion measurements. The spring constant of the cantilever was determined as 0.4 N/m.

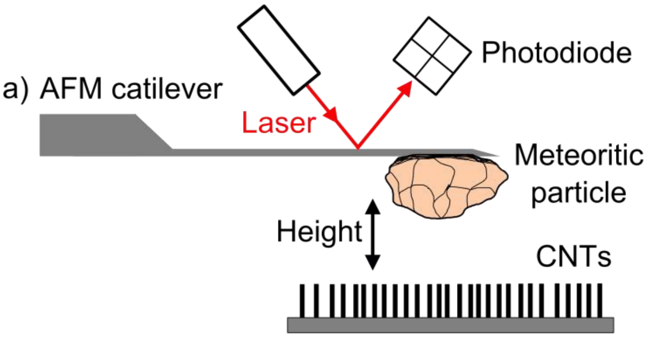

b) Mars meteorite (NWA 6963)

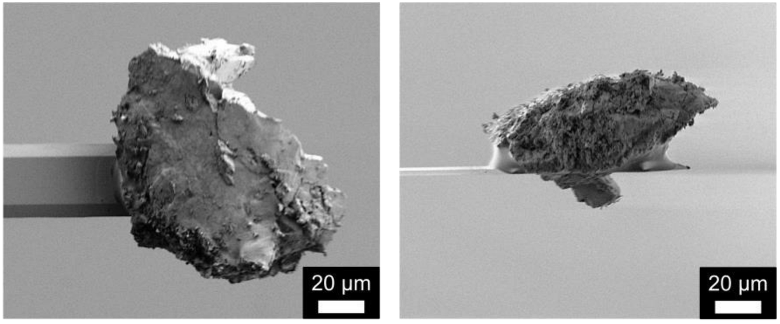

c) Lunar meteorite (NWA 4881)

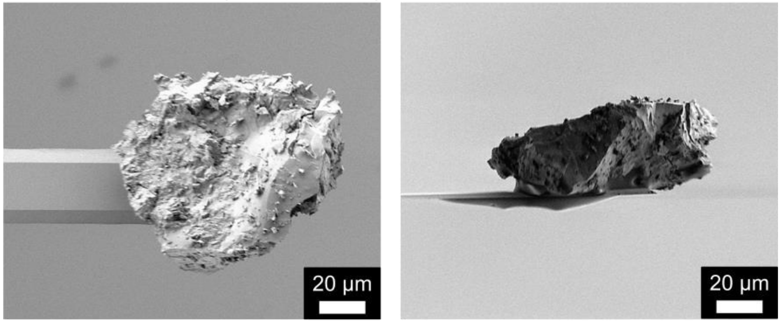

d) Chelyabinsk meteorite (chondrite LL5)

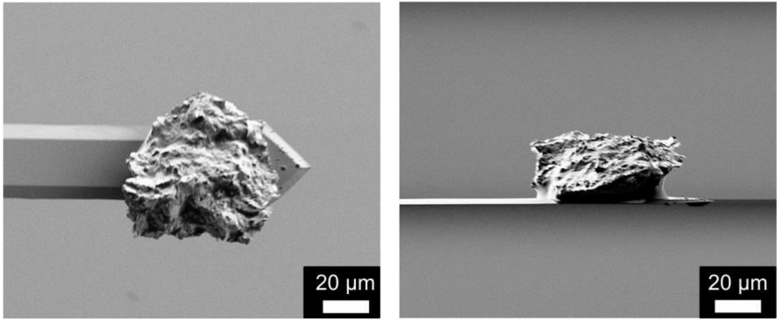

Figure 3.3: Adhesion measurement between CNT arrays and micrometeorites mounted on AFM cantilevers. a) Schematic setup for the AFM based adhesion measurement. A debris part of a tiny meteorite is glued to an AFM cantilever and pressed into CNT arrays followed by a lift-off. During this process the cantilever bends. A laser beam is focused on the backside of the cantilever and a photodiode detects the bending with the information of the adhesion properties, to calculate the adhesion forces and energies. Three different meteoritic probes were prepared and used for the adhesion measurements, b) a Mars meteorite (NWA 6963), c) a lunar meteorite (NWA 4881) and d) a meteorite from Chelyabinsk (chondrite LL5). The SEM images represent top views on the left side and side views (90° tilted) on the right side.

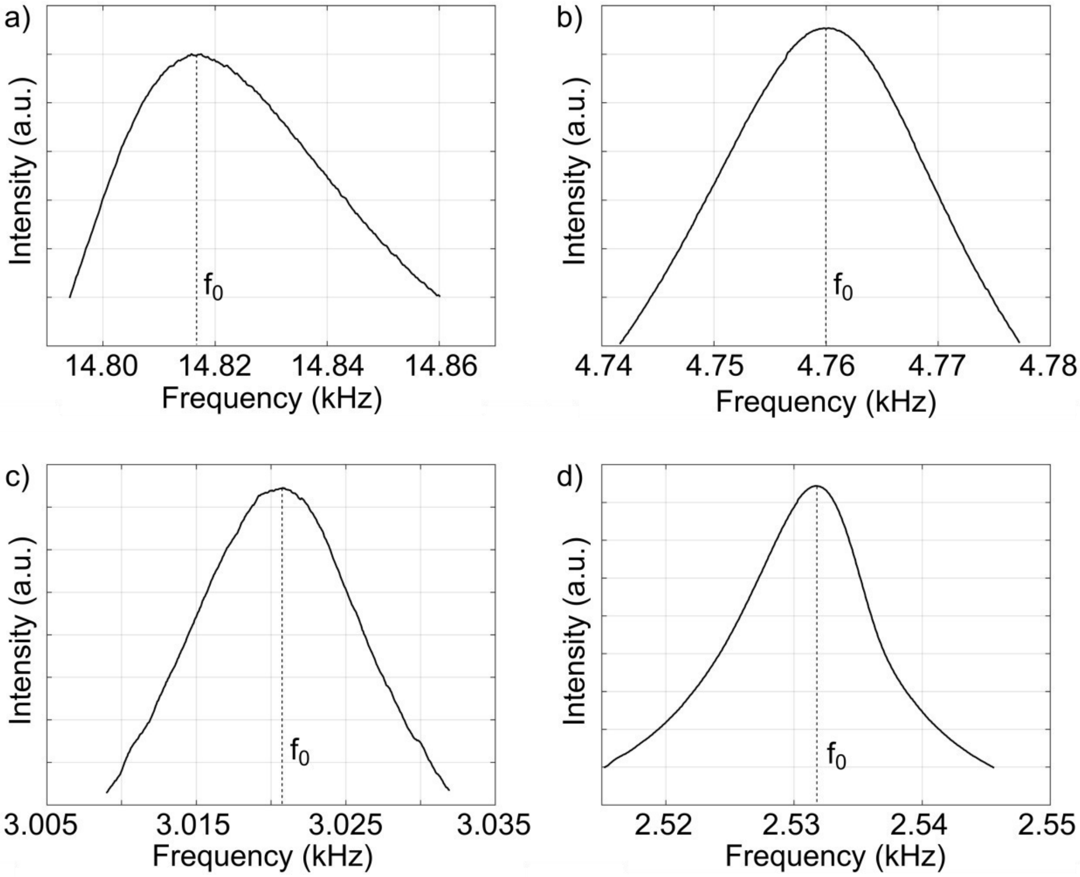

Figure 3.4: Resonance frequency measurement for micro-meteorites mounted on AFM cantilevers for the calculation of the mass of the debris parts of the meteorites. a) A tipless cantilever without a meteorite with a measured resonance frequency of 14.82 kHz, resulting in an effective mass of the cantilever of 46 ng. b) The cantilever with the Chelyabinsk meteorite has a resonance frequency of 4.76 kHz, resulting in a mass of the meteorite of 0.40 µg. c) The cantilever with the lunar meteorite has a resonance frequency of 3.02 kHz, resulting in a mass of the meteorite of 1.07 µg. d) The cantilever with the Mars meteorite has a resonance frequency of 2.53 kHz, resulting in a mass of the meteorite of 1.54 µg.

MWCNT arrays were used for the adhesion measurement of micro-meteorites. A PECVD process described in Ageev *et al.* [157] was performed by Oleg Ageev and Oleg Il'in for the production of MWCNT arrays (Figure 3.5 c). A piece of a Si-wafer (1x1 cm^2) with 1 µm SiO_2 on the top served as substrate. For the catalysts, a 20 nm thick layer of nickel was evaporated on the substrate. Before MWCNTs growth starts, a reduction step with ammonia (NH_3) and DC plasma (45 W) was conducted for 1 minute to get rid of the oxidized nickel layer leaving nickel on the surface. The MWCNT growth temperature was 750 °C with a growth time of 45 minutes. The chamber pressure was 4.5 Torr in the PECVD machine and a gas mixture of C_2H_2 with a flow rate of 70 sccm and NH_3 with a flow rate of 210 sccm was used.

Additionally, another kind of CNT sample was produced for the adhesion measurement between CNTs on AFM cantilevers and micro-ice surfaces. For this, a process based on an open ethanol flame as described in Chapter 4.3 was applied. Therefore, a piece of a Si-wafer (1x1 cm^2) was used and sputtered with a 50 nm tungsten layer. This substrate was dip-coated in a $NiCl_2$ solution in ethanol with a concentration of 20 mg/mL leaving a thin $NiCl_2$*$6H_2O$ layer on the surface, acting as the catalyst to grow CNFs. The sample was placed for 3 min in the ethanol flame resulting in micro bundles of CNFs.

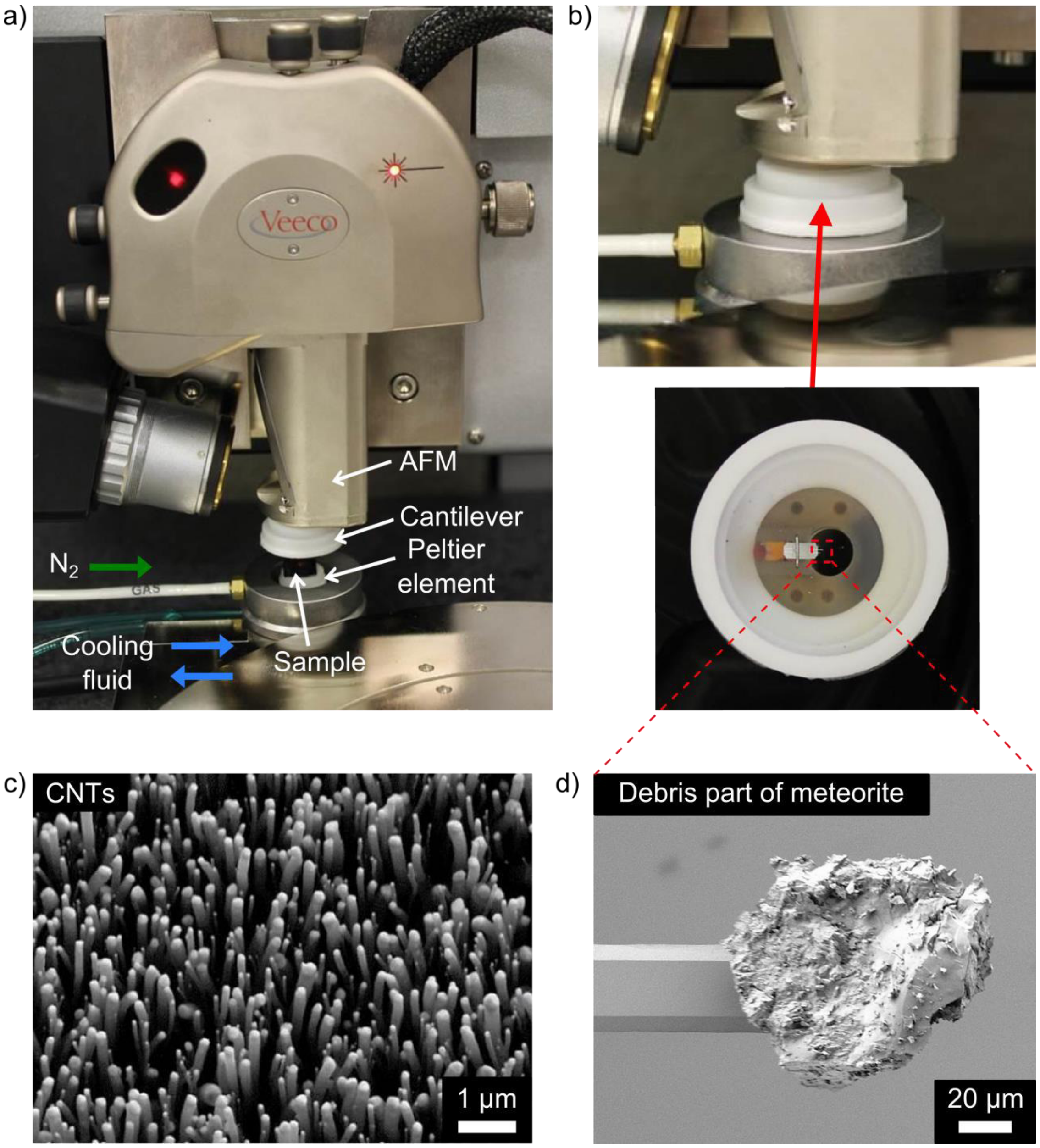

Figure 3.5: Setup for the temperature dependent AFM based adhesion measurement. a) The AFM measurement head and a Peltier element below it to cool down or heat up the sample. b) A silicone rubber seal can be placed on top of the Peltier element and the sample to achieve a closed system. Two pipes with a cooling fluid regulate the Peltier element and a pipe with gaseous nitrogen can be used to flood the chamber and conduct experiments under nitrogen atmosphere. This procedure is necessary at low temperatures (<0° C) to prevent condensation on the sample from the humidity in the air. c) SEM image with a 30° tilt of the used sample of aligned CNT arrays. d) The AFM cantilever with a debris part of a meteorite mounted to the cantilever.

3.4 Adhesion measurement between CNTs and micro-meteorites at low and high temperatures

Vertically aligned CNT arrays grown in a PECVD process as described in the previous section with diameters between 60 nm and 200 nm and heights of about 2 µm were used as the sample to measure the adhesion between debris parts of meteorites and CNTs. The grown CNTs benefit from a homogeneous density over the whole sample of about 7 CNTs/µm^2. Figure 3.3 a) shows the schematic adhesion measurement principle. Debris parts of meteorites mounted to AFM cantilevers were pressed into CNT arrays with a defined preload force and lifted-off. The results are force-distance diagrams (Figure 3.6) containing information about the adhesion force F_{adh} and energy E_{adh}, as well as the absorbed energy E_{abs}. Figure 3.6 shows three force distance diagrams obtained for the meteorites from a) Mars, b) Moon and c) Chelyabinsk. A preload force of 1 µN was used for all three measurements. The force-distance diagrams contain trace (blue dashed lines) and retrace (red solid lines). The retrace lines exhibit typical tear-offs originating from one or more CNTs contacting the micro-meteorite and loosing suddenly the contact to it during lift-off. Some adhesion measurements were conducted by Zeyu Ma as a part of his Bachelor thesis [158].

Figure 3.7 shows the results from the adhesion measurements with a) the adhesion force and b) the adhesion energy in a temperature range from -20 °C to +240 °C. Steps of 20 °C were used to conduct measurements at 14 different temperatures. For each temperature, five measurements on different areas of the sample were conducted to consider small changes in the quality of the CNT arrays. A mean value was calculated from the five values and the final data is shown in Figure 3.7 with error bars representing the standard deviation. The symbols correspond to the adhesion between CNT arrays and the micro-meteorite from Chelyabinsk (blue squares), from Mars (red circles) and from Moon (gray triangles). Linear fits were calculated (dashed lines). For the micrometeorite from Chelyabinsk, linear fits dependent on the temperature T: $F_{adh} = 446nN - 0.145(\frac{nN}{°C})T$ and $E_{adh} = 44.8fJ - 0.054(\frac{fJ}{°C})T$; for the micro-meteorite from Mars $F_{adh} = 483nN - 0.175(\frac{nN}{°C})T$ and $E_{adh} = 39.8fJ - 0.029(\frac{fJ}{°C})T$; and for the micro-meteorite from Moon $F_{adh} = 420nN - 0.152(\frac{nN}{°C})T$ and $E_{adh} = 21.3fJ - 0.005(\frac{fJ}{°C})T$.

The measured adhesion forces and energies are nearly constant or change only little over the investigated temperature range. However, there are temperature dependent effects that can influence the adhesion measurement. Even though CNTs are hydrophobic [159], tiny amounts of water from the air might condense on the catalytic centers made of nickel which are located at the top of the CNTs touching the micro-meteorite first during an adhesion measurement.

To prove the hydrophobicity of the used CNT arrays, the contact angle of a sample with CNTs was measured and compared with a reference sample consisting of a piece of a silicon wafer. Therefore, 4 µL droplets of deionized water were deposited on the CNTs and reference sample. Figure 3.8 shows the results from the contact angle measurements with a) the silicon reference sample and b) the CNT surface. The CNT surface resulted in a contact angle of 146° indicating a hydrophobic surface, whereas the silicon reference surface revealed contact angles between 50° and 60°. The condensation of water on the nickel catalysts can induce capillary forces which will disappear at higher temperatures. This can explain the slightly decline of the adhesion properties at elevated temperatures. Additionally, thermal fluctuation [160] might lead to a decreased adhesion.

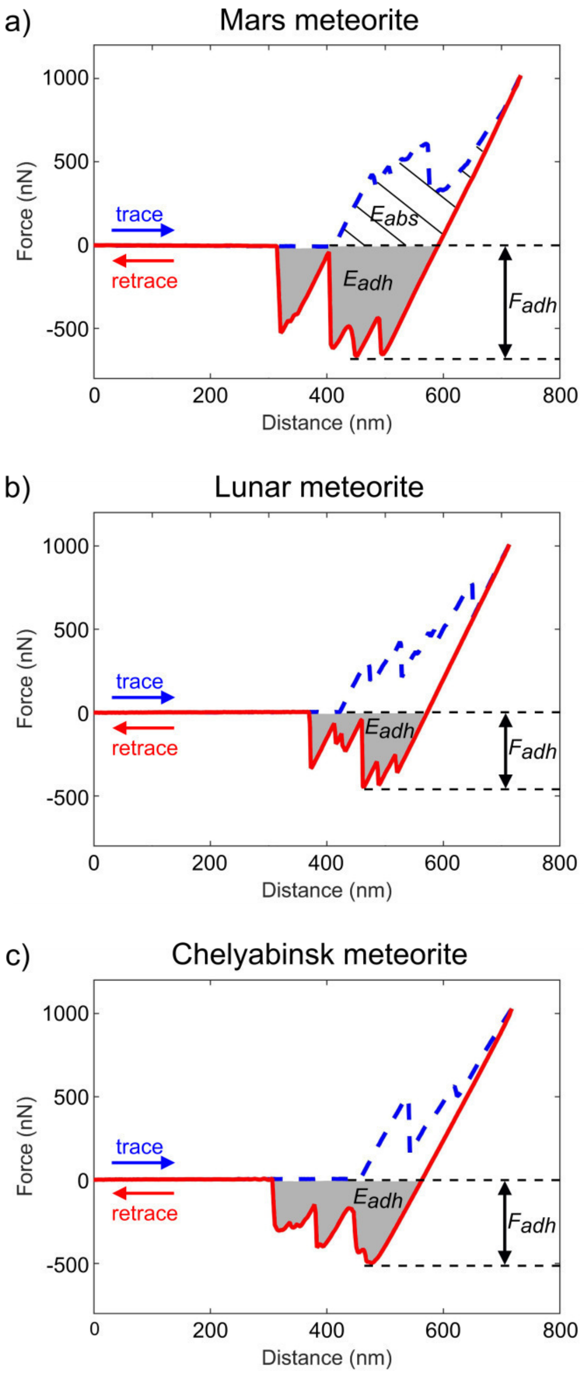

Figure 3.6: Force-distance diagrams from an AFM based adhesion measurement obtained between CNT arrays and debris parts of meteorites, for a) the Mars meteorite, b) the lunar meteorite and c) the meteorite from Chelyabinsk. A constant preload force of 1 µN was used for these adhesion measurements. The force-distance diagrams represent approach (blue dashed line) with the information about the absorbed energy (E_{abs}) and retraction (red solid line) with the adhesion force (F_{adh}) and the adhesion energy (E_{adh}).

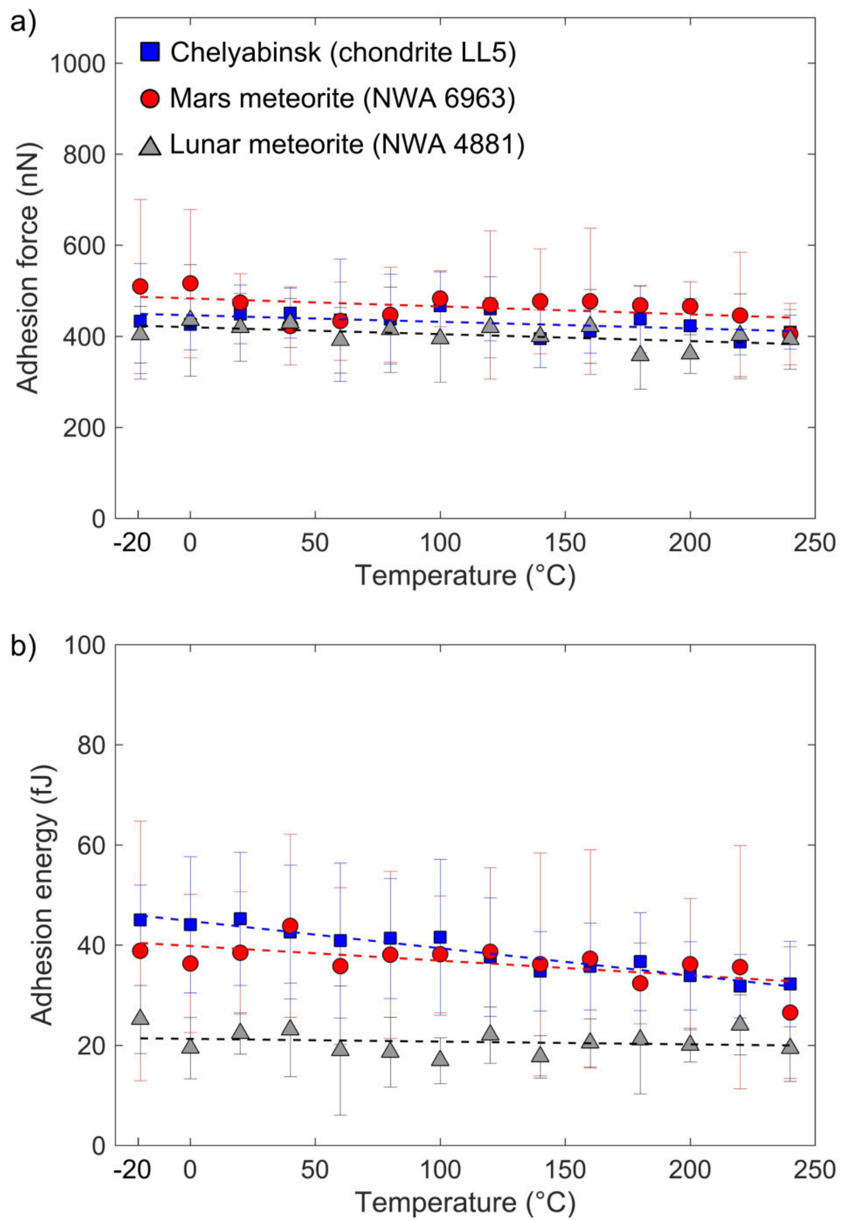

Figure 3.7: Temperature dependent adhesion measurements with a) the adhesion force and b) the adhesion energy between CNT arrays and debris parts of meteorites from -20 °C to +240 °C. The measurements in the temperature range were conducted with the debris parts of the Chelyabinsk meteorite (blue squares), the Mars meteorite (red circles) and the lunar meteorite (gray triangles). The error bars were calculated from five measurements and the data points represent the mean values. The linear fits are visualized as dashed lines. The adhesion forces and energies are nearly constant over the measured temperature range.

Small changes in the adhesion properties between the three investigated debris parts of meteorites, independent from the temperature can be explained by different geometric shapes and roughnesses of the micrometeorites (see Figure 3.3). Subsequently, this leads to different contact areas and small deviations in adhesion forces and energies. The debris part from the Mars meteorite revealed the highest adhesion force with 516 nN and an adhesion energy of 44 fJ. To refer the adhesion properties to an area, the contact areas of the debris parts of meteorites were estimated from SEM side views as described in Chapter 2.2.5. For the debris part of the Mars meteorite, a contact area of 20.6 µm² was determined, resulting in an adhesion force per area of ~2.5 N/cm² with an adhesion energy per area of 21 µJ/cm². This is a quarter of the adhesion force of a real gecko with 10 N/cm² [5].

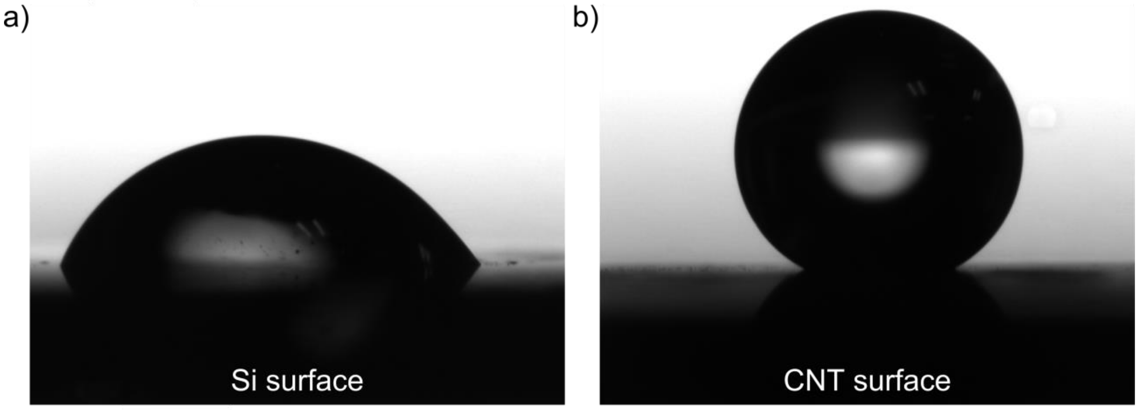

Figure 3.8: Contact angle measurements with a water droplet on a Si- and CNT surface. a) A 4 µL water droplet deposited on a part of a Si-wafer resulting in a contact angle between 50° and 60°. b) A water droplet of the same size deposited on an array with CNTs resulting in a contact angle of 146° indicating a hydrophobic surface.

A very important question for dry adhesives is how many times they can be used without replacement of the adhesion layers. In case of landing units, the adhesion layers have to perform only once. However, in case of rovers with covered dry adhesives feet, investigating meteorites, asteroids, comets or planet’s surface, the long term stability plays an important role. Therefore, endurance runs with 1000 attachment/detachment cycles between CNT arrays and the debris part of the Mars meteorite were conducted. The preload force was set to 1 µN with a ramp frequency of 1 Hz. Figure 3.9 shows the results of the endurance runs with a) the adhesion forces and b) the adhesion energies. The endurance runs were conducted at three different temperatures with three runs for each temperature of -20 °C (blue rhombuses), +120 °C (red squares) and +240 °C (magenta triangles). The error bars represent the standard deviations. The adhesion properties are nearly constant over the number of measurements independent from temperature.

However, another important question is if the CNT arrays would survive a complete space mission without losing their adhesion strength. Therefore, the sample was exposed to simulated space conditions by Pierre Jouanne and Amandine Charles at Thales Alenia Space. At first, to simulate a possible storage of 9 years on ground before the mission starts, a hydrothermal ageing of 7 days at 45 °C with a relative humidity of 93 % was performed. For the simulation of the flight to the Earth orbit, 10 thermal cycles starting from -50 °C up to +75 °C were conducted in vacuum. Finally, to simulate the operation in space after leaving the Earth orbit, 113 thermal cycles in a temperature range starting from -180 °C up to +150 °C were performed. After exposed to these simulated space conditions, the sample was measured again with respect to its adhesion properties. Therefore, endurance runs as described above were performed using the same cantilever and parameters. Figure 3.9 c) shows the measured adhesion forces and Figure 3.9 d) shows the respective adhesion energies. Compared with the measurements before, the adhesion forces and energies are in the same range and do not change very much during 1000 attachment/detachment cycles. SEM investigations of the CNT arrays exposed to simulated space conditions revealed no damage of the structures, showing the potential use of CNT arrays for long term adhesion applications under harsh environments as in space.

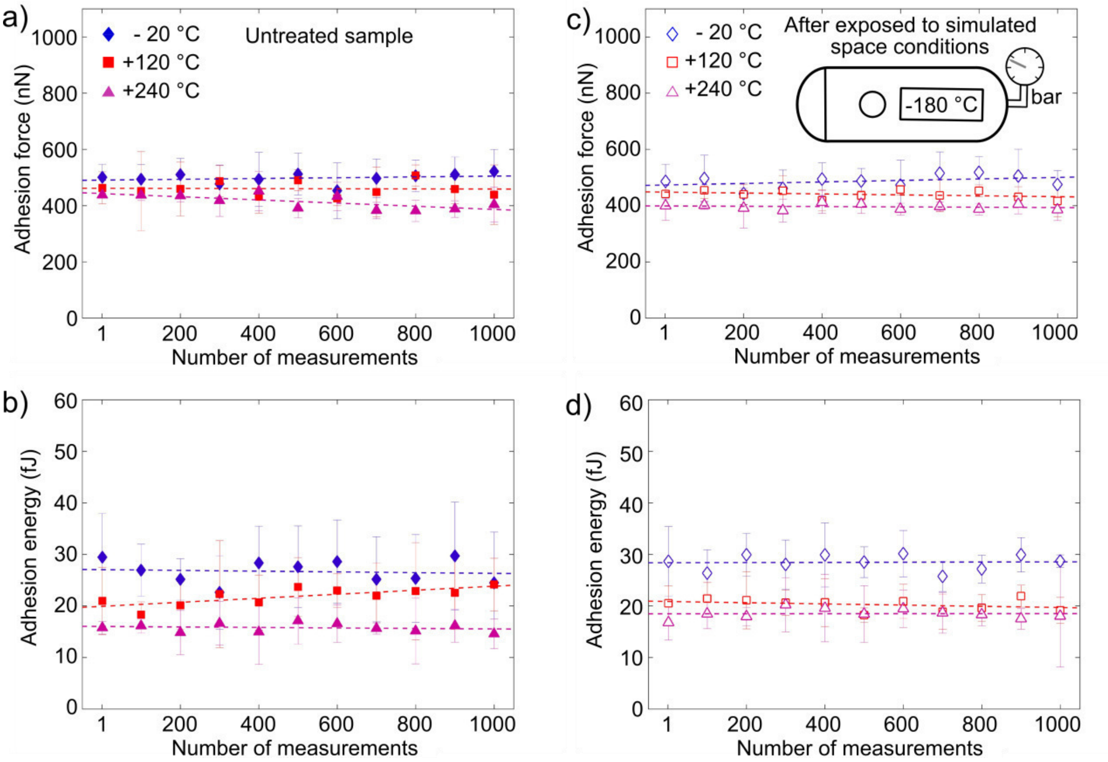

Figure 3.9: Endurance adhesion measurement between CNT arrays and the debris part of the Mars meteorite at different temperatures with a) the adhesion force and b) the adhesion energy. c), d) Show the same measurements after simulated space conditions. The measurements were conducted for 1000 approach/retraction cycles at -20 °C (blue rhombuses), at +120 °C (red squares) and at +240 °C (magenta triangles). Three endurance runs were conducted at each temperature and the mean values were calculated. The error bars represent the standard deviation from the three measurements. The dashed lines in the diagrams represent linear fits. The adhesion forces and energies are nearly constant for the endurance runs at different temperatures.

Additionally, CNTs might be used as a protection for micrometeorites [161]. The force-distance diagrams (Figure 3.6) contain the adhesion force and energy, as well as the absorbed energy (E_{abs}). The absorbed energy was calculated to 80 fJ for the debris part of the Mars meteorite to investigate the potential of the CNT arrays to absorb energy. Equalizing the absorbed energy with the kinetic energy ($E_{kin} = \frac{1}{2}mv^2$) of the Mars micrometeorite with a calculated mass of 1.53 µg (see Chapter 3.2). This results in a velocity of the micrometeorite of 0.01 m/s which could be absorbed by the meteoritic particle. This is much less than the velocities of meteorites which can achieve absolute velocities of several km/s [162]. However, CNT forests with heights of up to 12 mm [163] are assumable more suitable than the investigated CNTs with heights of only 2 µm to absorb more energy and subsequently absorb higher velocities. An envisioned application for the investigated CNT arrays could be ‘catching-boards’ of CNTs on space probes to catch micrometeorites.

3.5 Adhesion measurement between CNTs and micro-ice layers

The following adhesion measurements between CNTs and ice surfaces are motivated by a possible landing on comets which consist mainly of rock and ice material [164]. However, it is not simple to measure the adhesion between CNTs and ice surfaces. Using the same approach as described in Chapter 3.4, where debris parts of meteorites were mounted to AFM cantilevers, would not work with micro-debris parts of ice at a conventional lab with room temperature. The ice particle would melt after a few seconds. However, regulating the lab temperature below 0 °C might enable the transferring process of ice debris but during the measurement, where a laser is focused on the cantilever not far away from the tiny ice debris, the ice would melt, making a measurement impossible.

Therefore, the measurement procedure was inverted, which means that the ice layer was grown on a piece of a Si-wafer placed over the Peltier element and a bundle of CNTs was mounted on a tipless AFM cantilever. However, the CNTs grown with PECVD for the adhesion measurement between meteorites cannot be used for mounting AFM cantilevers due to their small heights of 2 µm and their strong connection with the Si-surface. Therefore, CNTs and CNFs in the shape of a bundle grown with flame synthesis (see Chapter 4.3) were used. The diameters of the CNTs or CNFs in the bundle are in the range of 40 nm with lengths up to 60 µm. The CNT/CNF bundle was transferred to a tipless AFM cantilever using the micro-manipulator as already described in Chapter 2.2.3. Figure 3.10 a) shows the CNT/CNF bundle mounted to an AFM cantilever with b) a magnified view of the CNTs/CNFs.

Determining the resonance frequency of the CNF bundle on the AFM cantilever offers a possibility to calculate the mass of the self-grown CNF bundles with flame synthesis. A resonance frequency of 6.95 kHz was measured for the CNT bundle mounted on a tipless AFM cantilever (Figure 3.11). Using the effective mass of tipless cantilever with 46 ng from Chapter 3.2 and Equation (3.2) leads to a mass of the CNT bundle of 1.272 µg. The CNF bundle has a dimension of 80 x 80 x 110 µm³ as determined from the SEM images leading to a volume of the CNF bundle of 7.04 x 10^5 µm³. Subsequently, a CNF bundle density of 1.807 g/cm³ was calculated. For comparison, the density of single CNFs is 1.78 g/cm³ [44], and very close to this value.

The micro-ice layer was grown on a piece of a Si-wafer from condensed water of the air with a relative humidity of 24 % at 21 °C, resulting in an absolute humidity of 4.4 g/m³. The temperature of the Si-wafer placed on the Peltier element was set to 0 °C leading to condensation of water droplets which aggregate after 2 min to droplets with diameters between 20 – 60 µm (Figure 3.10 c). After 2 min at -20 °C the water droplets change their aggregation state and freeze to ice (Figure 3.10 d), which is stable due to a complete condensation of the air in the camber (volume ~3 cm³) on the Si-surface. To achieve a closed ice layer a pump was used to bring fresh humid air inside the chamber, resulting in a growing ice layer (Figure 3.10 e). The inlet of the pump was closed after a closed ice layer was obtained (Figure 3.10 f). Figure 3.12 shows an AFM topography scan (10 x 10 µm²) of a produced ice layer on the Si-surface. The topography measurement revealed that the ice layer consists grains with sizes between 2 µm and 8 µm.

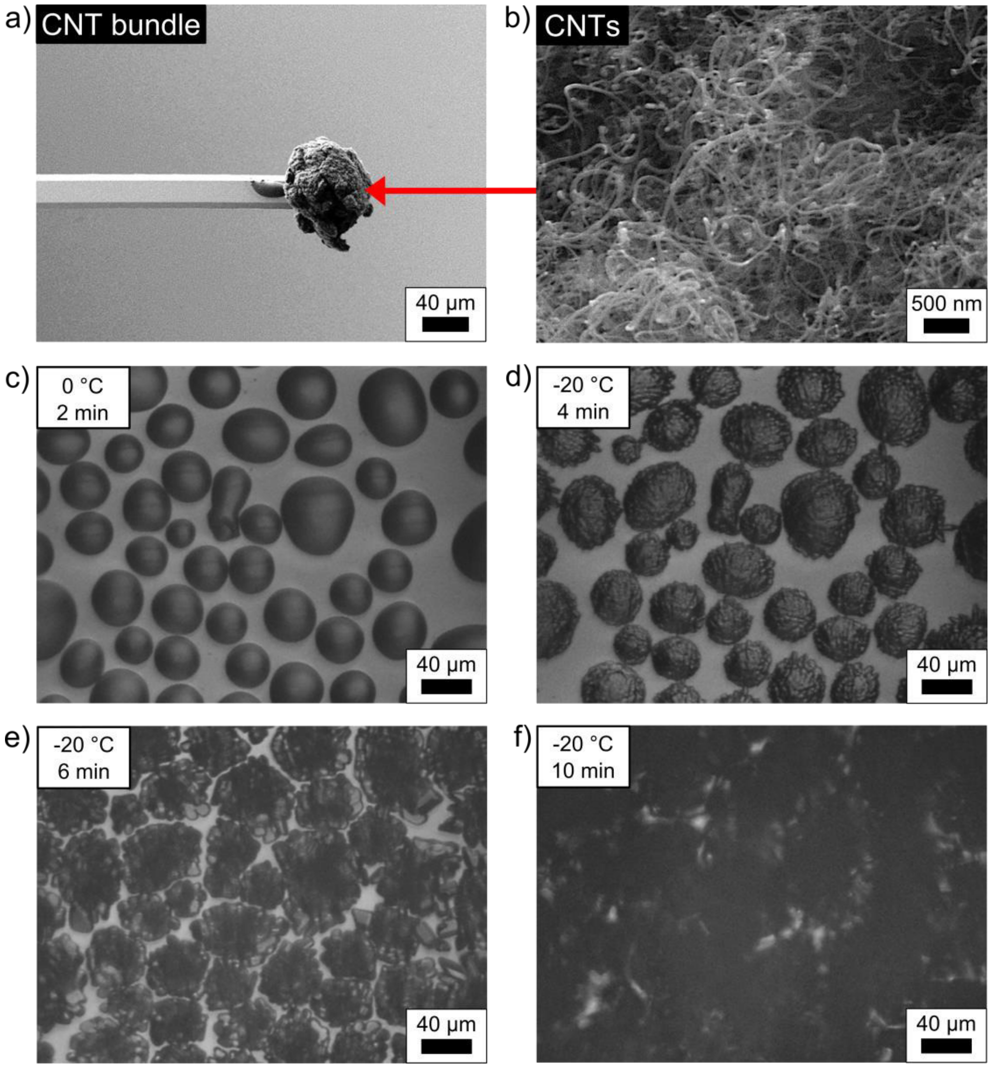

Figure 3.10: Adhesion measurement between CNTs and micro ice layers. SEM images with a) a CNT bundle mounted on a cantilever and b) a higher magnification of the CNTs. Images from a light microscope during the production of micro-ice layers on a silicon sample over the Peltier element. c) Micro water droplets condensed on the silicon substrate at 0 °C and 2 min, d) micro-ice droplets achieved after 4 min by -20 °C, e) growing ice layer with the addition of fresh humid air and f) a nearly closed ice layer usual used for measurements.

It should be mentioned that keeping the ice-layer stable was one of the biggest challenges to conduct the measurement. Therefore, the laser beam used for the detection of the cantilevers bending was placed away from the top with the CNTs near to the base to prevent heating up the area under the CNTs and subsequently melting the ice layer. Additionally, the illumination of the AFM microscope was switched off, to conduct the measurement in darkness, to prevent heating the ice layer. Using these two measurement settings, it was possible to maintain the ice layer for 10 min which is sufficient to conduct about 500 adhesion measurements by using a ramp frequency of 1 Hz. The preload force was set to 1 µN and the temperature was constant at -20 °C during the measurement. Figure 3.13 a) shows a force-distance diagram obtained between CNTs and ice layers with trace (blue dashed line) and retrace (red solid line). The retrace line revealed several tear-offs originating from CNTs loosing suddenly the contact to the ice layer. Three areas of the ice layer were chosen to conduct endurance runs with 500 measurements.

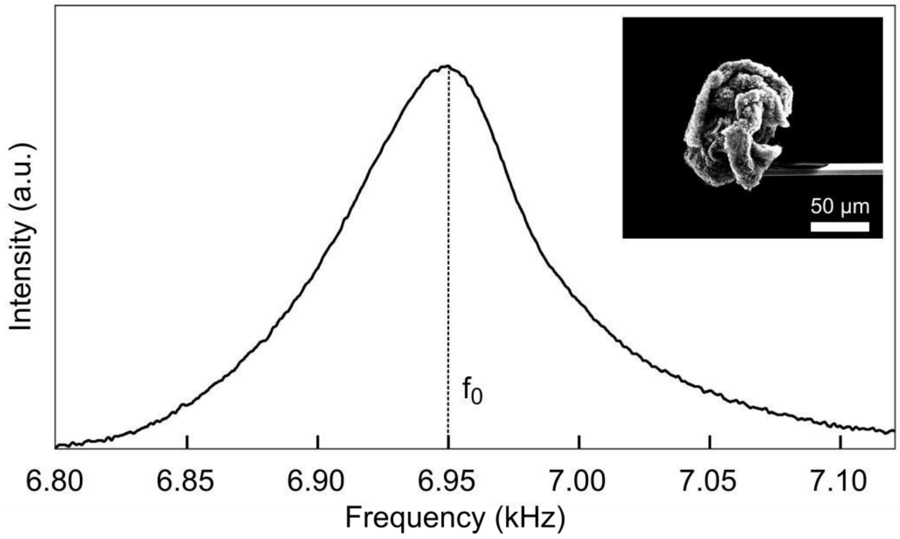

Figure 3.11: Resonance frequency measurement from the CNF bundle mounted on an AFM cantilever. The CNF bundle on the cantilever depicted in the inset SEM image has a dimension of 80 x 80 x 110 µm³. The resonance frequency was measured to 6.95 kHz, leading to a density of the CNFs in the bundle of 1.807 g/cm³.

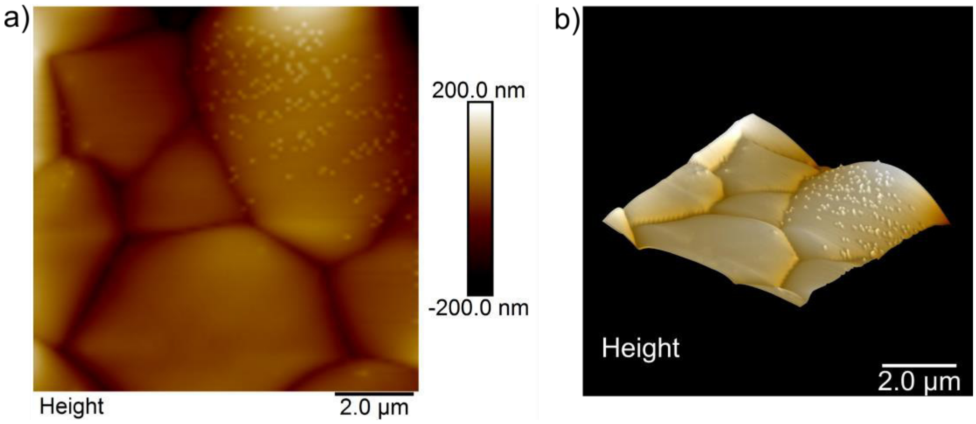

Figure 3.12: AFM scan of micro ice layer topography, with a) a 2D topography scan of a 10 µm x 10 µm ice layer and b) the corresponding 3D topography. The topography measurements revealed ice grains in the range from 2 µm to 8 µm.

Figure 3.13 shows the results of the endurance runs with b) the adhesion forces and c) the adhesion energies. The error bars represent the standard deviations. Different surface geometries of the three ice areas under test may cause the deviations of the adhesion properties. However, the adhesion force as well as the adhesion energy is constant for up to 500 measurements. The adhesion properties were referred to an area as described in Chapter 2.2.5 to achieve comparable results independent from the contact area during the adhesion measurement. The adhesion force was calculated to 2.3 N/cm² and the adhesion energy to 2.5 µJ/cm². The adhesion force is only marginal lower compared with the adhesion force of the debris part of the Mars meteorite with 2.5 N/cm². Subsequently, the adhesion force between CNTs and ice layers is in the same range as between CNTs and micrometeorites. However, the adhesion energy is about 10 times higher, which can be explained by longer CNTs (~60 µm) used in this experiment compared with the CNT arrays (~2 µm) used for the measurement between CNTs and micrometeorites. Longer CNTs lead to a longer contact to the surface under test during lift off and subsequently to a larger area in the force-distance diagrams, resulting in higher adhesion energies.

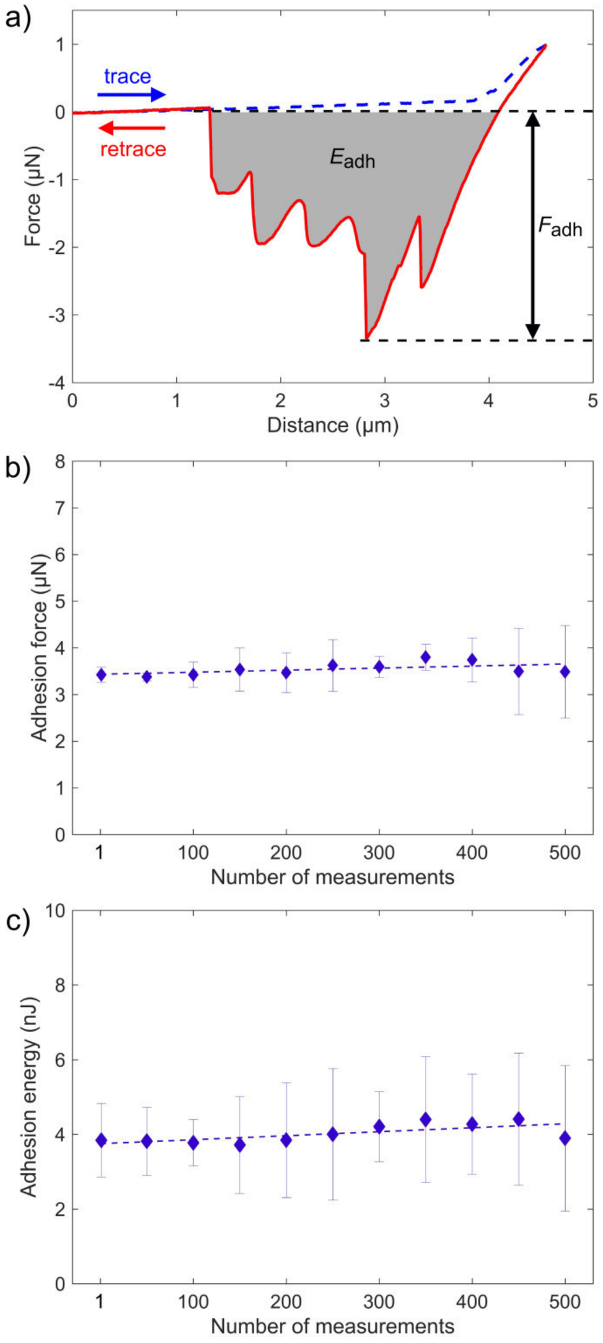

Figure 3.13: Adhesion measurement between CNT bundles and micro-ice layers. a) A force distance diagram indicating up to five tear-offs due to the interaction between CNTs and micro-ice layers. Endurance runs revealed that b) the adhesion forces and c) the adhesion energies are nearly stable for up to 500 measurements. The dashed lines represent linear fits to the data.

A shortened version of the CNF based dry adhesives for space technology investigation in this chapter was published as the article [165] "Analysis of Carbon Nanotube Arrays for Their Potential Use as Adhesives Under Harsh Conditions as in Space Technology", by Christian Lutz, Zeyu Ma, Richard Thelen, Julia Syurik, Oleg Il'in, Oleg Ageev, Pierre Jouanne and Hendrik Hölscher, Tribology Letters, 67, 1-10 (2019)

4 CNF growth with flame synthesis and their use as dry adhesives

CNFs and CNTs are due to their outstanding mechanical properties (see Chapter 2.1.1) very promising materials for several applications, such as dry adhesives [39]. Flame synthesis of CNFs is a simple, fast and cost-effective way to grow CNFs. In this chapter flame synthesis of CNFs is systematically investigated in order to grow dense arrays of CNFs with the possibility to align the CNFs during growth via a magnetic field. The adhesion properties of these structures are investigated by AFM. Endurance runs are performed to demonstrate the long term adhesion stability of the grown CNF arrays.

4.1 Flame synthesis of CNFs

Synthesis of CNFs in an open flame, as described in Chapter 2.1.4, is poorly investigated up to now. Although in this study a standard ethanol or methanol burner was used and the sample was placed inside the flame with the possibility to apply a magnetic field as schematically depicted in Figure 4.1. The sample consists of a piece of a silicon waver with a thin metal layer covered with catalysts from metallic salts ($NiCl_2$, $FeCl_2$ and $CoCl_2$). Surprisingly, this process to grow CNFs with, e.g., $NiCl_2$ on thin Cu substrates allows to grow CNFs without the usual reduction step typically conducted in CVD and PECVD, where hydrogen or ammonia reduces the metal catalysts to a pure state before CNFs can start to grow. This can be explained with the work of Kumar *et al.* [166]. They reported that catalysts made from copper and nickel can produce hydrogen during the exposition to an open ethanol flame. This hydrogen produced in the ethanol flame might work similar as the hydrogen which is pumped into a CVD or a PECVD chamber to reduce the catalysts to pure state.

Zhang and Pan [120] used a similar process with an ethanol flame, where the sample was aligned horizontally with the catalytic side pointing downwards. However, it was observed in this thesis that a vertical alignment of the sample over the flame leads to a much more stable open ethanol flame compared with the horizontal alignment. This can be explained by a better aerodynamic stream of the ethanol flame around the sample, which can be considered as a plate. In general, vertical aligned samples result in less turbulences compared to horizontal aligned samples and hence to a more stable ethanol flame.

It should be mentioned that growing CNFs in an open ethanol flame is not straightforward. First experiments with burning ethanol in a ceramic bowl were not successful, assumably due to flicker of the flame, leading to parts of the sample which are outside the flame for a short time. This results in re-oxidation of the used catalytic centers and subsequently stops CNF growth before it starts. However, there are several other factors deciding between CNFs growth and no growth. Very important are humidity and temperature, the used catalyst or the applied magnetic field which are explained in detail in the following.

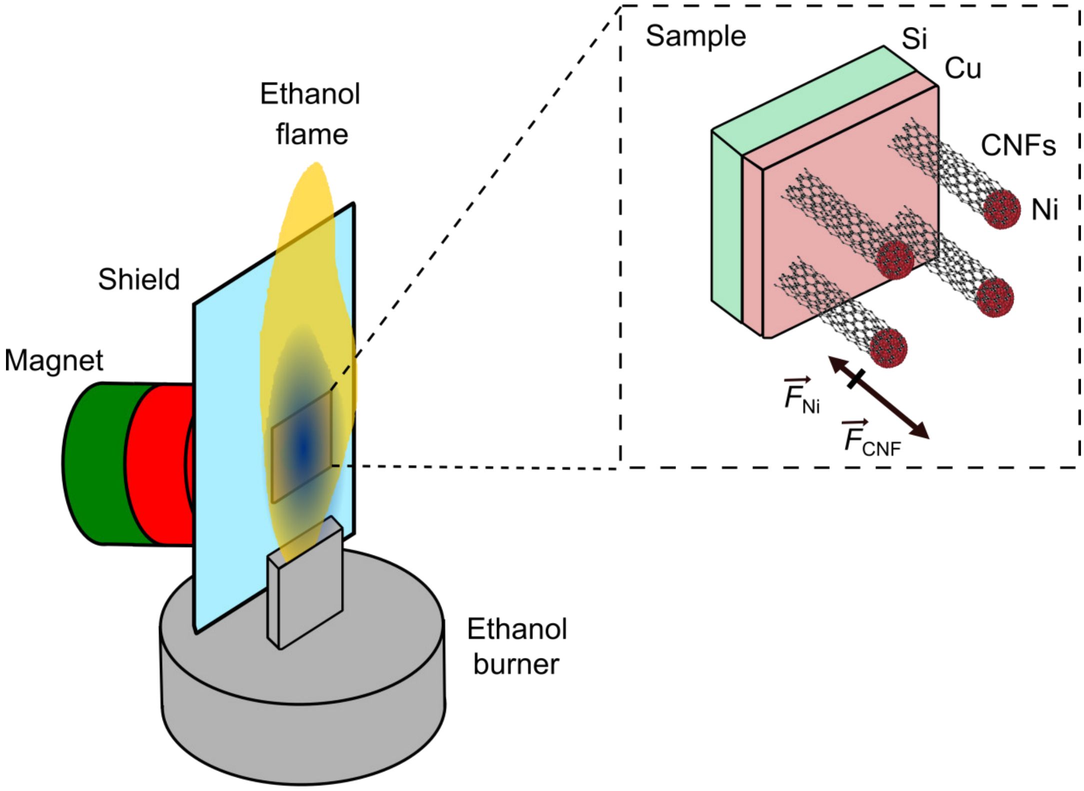

Figure 4.1: Schematic setup for flame synthesis of CNFs and their alignment using a permanent magnet. The setup consists of an ethanol burner and a sample is placed horizontally directly over the wick in the flame. A silicon shield is placed between the magnet and a sample to prevent the magnet from heating up and subsequently losing its performance. A part of a silicon wafer, served as substrate covered with a thin cooper layer. A layer of $NiCl_2$ as catalyst is deposited on the copper layer of the sample to grow CNFs. The CNFs orient in the magnetic field during growth due to diamagnetic forces acting away from the magnet on the CNFs $(\vec{\boldsymbol{F}}_{\boldsymbol{CNF}})$. However, there are small paramagnetic forces $(\vec{\boldsymbol{F}}_{\boldsymbol{Ni}})$ acting to the magnet instead of much higher ferromagnetic forces on the Ni catalysts due to a temperature of 750 °C which is above the Curie temperature of Ni with about 358 °C [167]. The observed alignment of the CNFs away from the magnet revealed that the diamagnetic forces acting to the CNFs are higher than the paramagnetic forces acting to the Ni catalysts.

4.2 Combinatorics flame synthesis of CNFs

In this section, rigorous investigation of flame synthesis of CNFs is presented with the setup from the previous Chapter using a standard ethanol or methanol burner, different substrates and catalysts, to determine the best working parameters to grow CNF arrays with a high and uniform density of CNFs. The challenge in CNT and CNF growth is to find working process parameters under nearly endless possible combinations. Three important parameters in flame synthesis are the fuel which offers the carbon, the substrate which acts as an under layer and the catalysts from which the CNFs grow from. The conducted experiments considered all possible and suitable combinations. Ethanol and methanol were chosen as fuel due to their liquid state at room temperature which allows fueling a flame burner. Especially ethanol was successfully used in several studies to grow CNTs and CNFs [117]–[119] and is therefore in the focus of interest. Seven substrates of Si, SiO_2, Al_2O_3, Cu, Ti, Ta and W which are used in several studies were selected. Three catalysts with $NiCl_2$, $FeCl_2$ and $CoCl_2$ were chosen and solved in ethanol to achieve a 20 mg/mL solution. Additionally, a second $CoCl_2$ solution with methanol as solvent

(20 mg/mL) was produced. Dependent on temperature, concentration and solvent, $CoCl_2$ solutions change very strongly their color in a range from pink to blue [168]. The $CoCl_2$ solution in ethanol is deep blue whereas the solution in methanol is pink (see Figure 4.2). Especially cobalt was in the focus of interest due to its high Curie temperature of 1131 °C [167], which is above the temperature in the ethanol flame, offering a possibility to align the CNFs during growth by applying a magnetic field.

The total amount of experiments n_e dependents on the number of fuels n_f, the number of substrates n_s and the number of catalysts n_c.

$$n_e = n_f n_s n_c \tag{4.1}$$

By using two fuels, seven substrates and four catalyst solutions, 56 combinations of CNF growth experiments with flame synthesis were conducted to consider every possible option. To evaluate the CNF growth experiments, the growth activity g_a was defined, which is dependent on the fuel f, the substrate s and the catalyst c. Its value increases with the amount of CNFs per area.

$$g_a(f,s,c) = \begin{cases} 0, & n_{CNF} = 0 \\ 0.05, & n_{CNF} = 1 \\ 0.1, & n_{CNF} = 2 \\ 0.2, & n_{CNF} = 10 \\ 0.5, & n_{CNF} = 100 \\ & \vdots \\ 1.0, & n_{CNF} > 1000 \end{cases} \tag{4.2}$$

Three SEM images, each of them corresponding to an area of about 50 µm² on random positions of the sample were evaluated and the amount of CNFs was counted (n_{CNF}) to assign the growth activity a value. The growth activity is defined as zero, if no CNF was observed on the SEM images and a growth activity of 0.05, if one CNF was observed. Two CNFs are defined with a growth activity of 0.1 and a growth activity of 1.0 means more than 1000 CNFs on the three SEM images. Consequently, to achieve a defined growth activity of 1.0 leads to a density of ~7 CNFs/µm².

Figure 4.2 shows the results from 56 flame synthesis experiments to grow CNFs with the used catalytic solution on the left side, the growth activity for ethanol flame synthesis in the middle and the growth activity for methanol flame synthesis on the right side. All catalytic solutions have a concentration of 20 mg/mL of the metal salt solved in the solvent ethanol or methanol. The solution with $NiCl_2$ as catalysts a) leads to the highest CNF outcome. All investigated substrates reveal CNF growth independent if ethanol or methanol is used as fuel. However, the highest growth activity was recorded for the ethanol flame synthesis of $NiCl_2$ on copper substrates with a growth activity of 1.0, followed from the tungsten substrate with a growth activity of 0.8. For the $CoCl_2$ catalysts, two solutions were prepared, one with $CoCl_2$ solved in methanol b) and the other one with $CoCl_2$ solved in ethanol c). It was observed that $CoCl_2$ solved in methanol b) showed the highest growth activity during methanol flame synthesis. However, $CoCl_2$ catalysts show less growth activity compared with $NiCl_2$ catalysts. The $FeCl_2$ catalyst d) exhibited the lowest growth activity of the investigated catalysts. Only three experiments out of 14 tests revealed CNF growth.

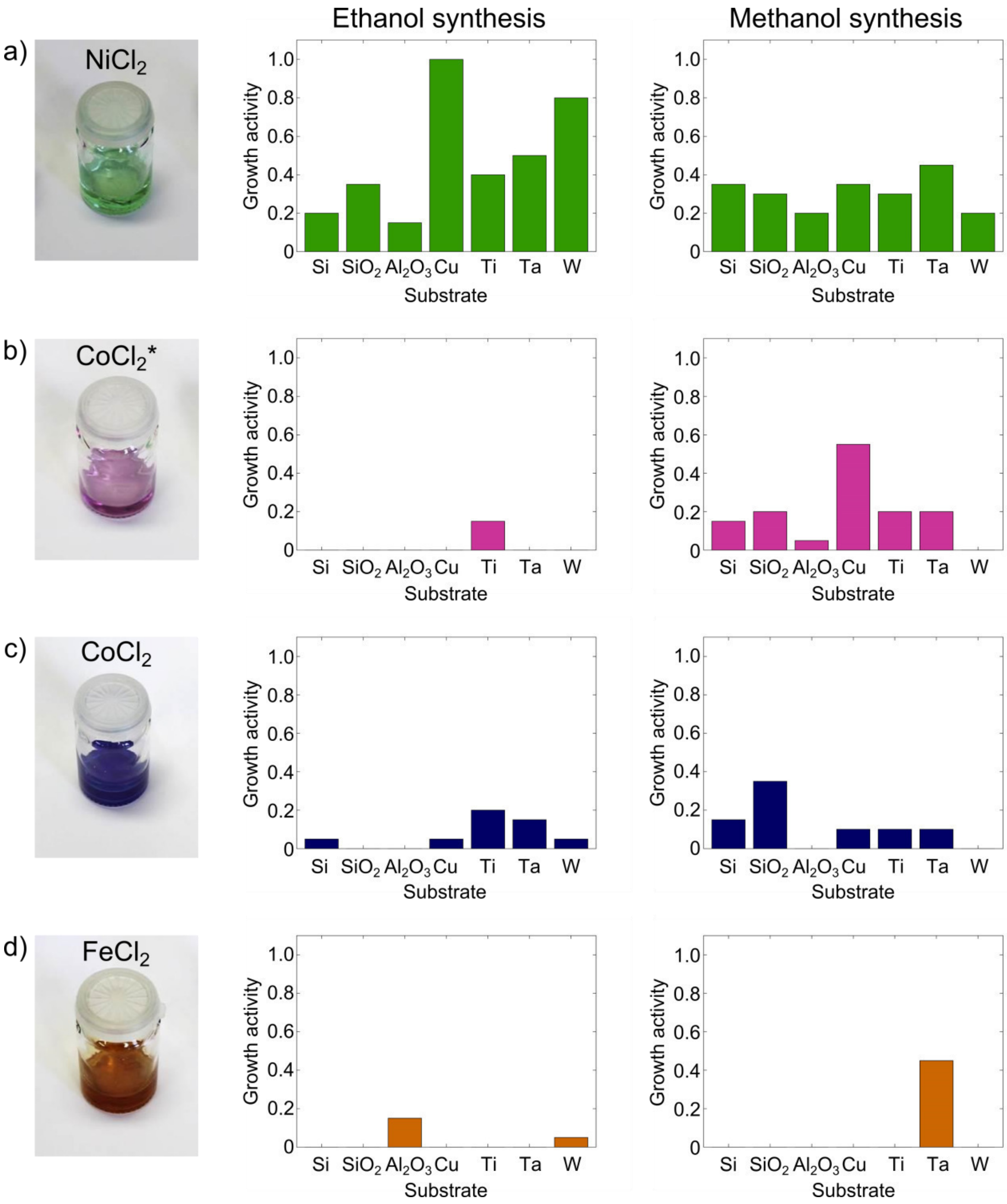

Figure 4.2: Ethanol and methanol based flame synthesis of CNFs, with photos of the solutions on the left side, the results with the growth activity for ethanol synthesis in the middle and for methanol synthesis on the right. Three solutions with metal salts ($NiCl_2$, $CoCl_2$ and $FeCl_2$) as catalysts solved in ethanol and one solution with $CoCl_2$ solved in methanol (marked with '*') were investigated after their ability to grow CNFs on different substrates using flame synthesis with ethanol or methanol as fuel. All produced solutions have a metal salt concentration of 20 mg/mL. The best results were achieved with $NiCl_2$ as catalyst a), exhibiting CNF growth on all investigated substrates. The highest growth activity was achieved with a value of 1.0 on a Cu substrate, followed by a W substrate with a growth activity of 0.8. $CoCl_2$ solved in methanol b) showed the best results for methanol synthesis on Cu substrates. Whereas $CoCl_2$ solved in ethanol c) worked best in methanol synthesis on SiO_2 substrates. $FeCl_2$ as catalysts d) shows the smallest CNF outcome, with three working material combinations out of 14 options.

A compilation of all growth activity values is shown in Table 4.1 for ethanol flame synthesis and in Table 4.2 for methanol flame synthesis. In general 22 experiments showed no CNF growth, whereas 34 experiments showed CNF growth out of a total number of 56 experiments. This means that 60 % of the combinations exhibited CNF growth.

Table 4.1: Growth activity from the ethanol flame synthesis. Three metal salts solved in ethanol and one solved in methanol (marked with '*') were used as catalysts on seven different substrates.

Substrate Catalyst	Si	SiO_2	Al_2O_3	Cu	Ti	Ta	W
$NiCl_2$	0.2	0.35	0.15	1.0	0.4	0.5	0.8
$CoCl_2$*	0	0	0	0	0.15	0	0
$CoCl_2$	0.05	0	0	0.05	0.2	0.15	0.05
$FeCl_2$	0	0	0.15	0	0	0	0.05

Table 4.2: Growth activity from the methanol flame synthesis. Three metal salts solved in ethanol and one solved in methanol (marked with '*') were used as catalysts on seven different substrates.

Substrate Catalyst	Si	SiO_2	Al_2O_3	Cu	Ti	Ta	W
$NiCl_2$	0.35	0.3	0.2	0.35	0.3	0.45	0.2
$CoCl_2$*	0.15	0.2	0.05	0.55	0.2	0.2	0
$CoCl_2$	0.15	0.35	0	0.1	0.1	0.1	0
$FeCl_2$	0	0	0	0	0	0.45	0

Figure 4.3 shows a compilation of six SEM images from CNFs grown with flame synthesis. With CNFs grown in an ethanol flame from a) Ni catalysts on a Cu substrate, b) Ni catalysts on a W substrate and c) Ni catalysts on a Ta substrate. CNFs grown in a methanol flame from d) Co catalysts solved in methanol on a Cu substrate, e) Co catalysts solved in ethanol on a SiO_2 substrate and f) Fe catalysts on a Ta substrate. The flame synthesis of CNFs distinguishes between each other after their size, quality and density of the CNF outcome. In general, the growth quality of the CNFs grown in the ethanol flame is higher, as compared to CNFs grown in the methanol flame. The CNF arrays from a) and b) are due to their high quality and density suitable for dry adhesives.

4.3 Ethanol based flame synthesis of CNFs from nickel chloride

As investigated in the previous section, flame synthesis of CNFs with an open ethanol flame using $NiCl_2$ catalysts on copper substrates is the most promising way to produce large arrays with uniform density and quality of CNFs for their application as dry adhesives by using flame synthesis. Therefore, rigorous investigation of this process to optimize the quality and outcome of CNF arrays for dry adhesives is presented in this section.

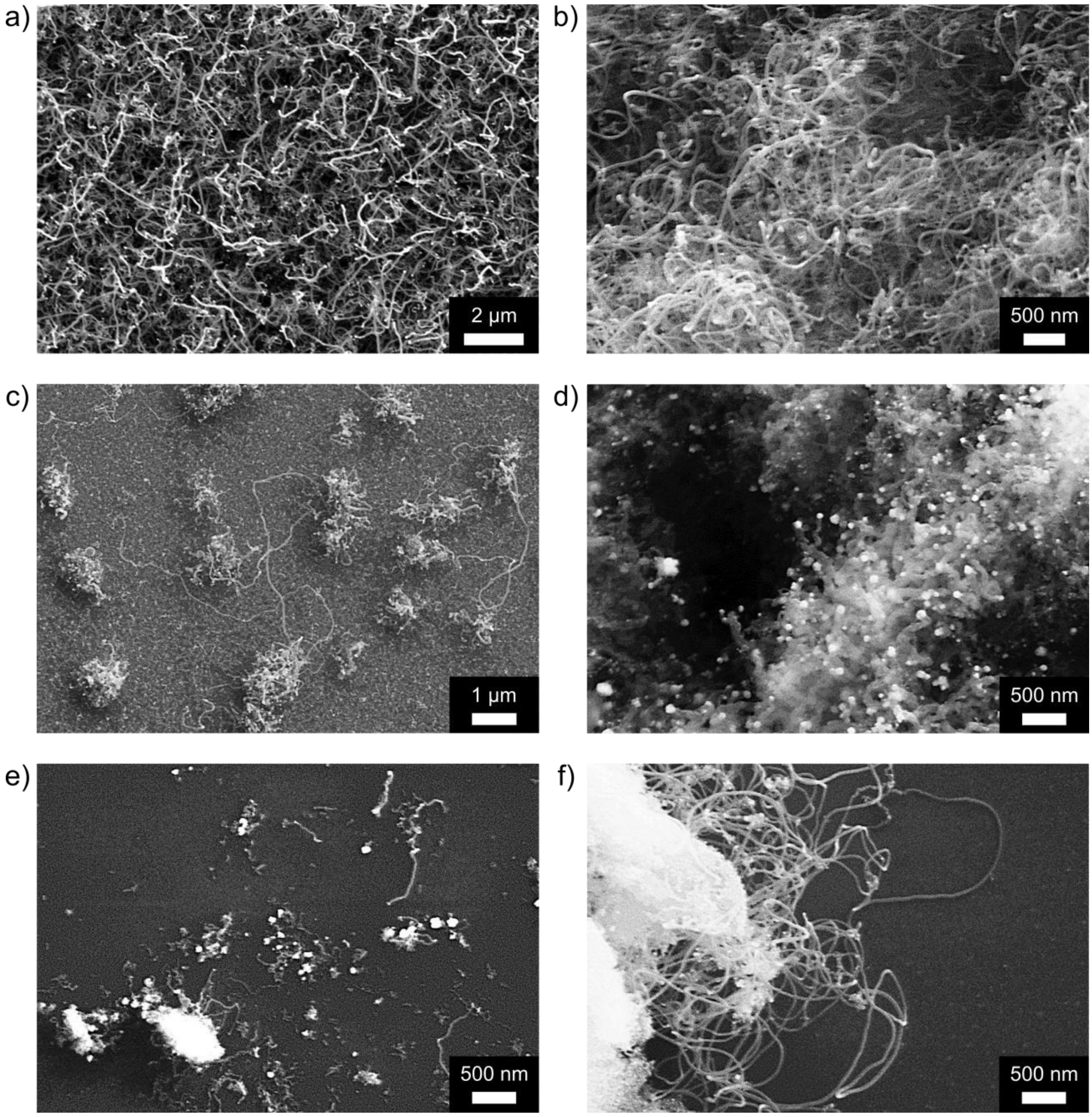

Figure 4.3: SEM images of the flame synthesis of CNFs. CNFs grown in an ethanol flame from a) Ni catalysts on a Cu substrate, b) Ni catalysts on a W substrate and c) Ni catalysts on a Ta substrate. CNFs grown in a methanol flame from d) Co catalysts solved in methanol on a Cu substrate, e) Co catalysts solved in ethanol on a SiO_2 substrate and f) Fe catalysts on a Ta substrate. The density and quality required for dry adhesives were achieved in a) and b).

4.3.1 Experimental setup

To grow CNFs from ethanol based flame synthesis, the same setup as described in Chapter 4.1 was used. The ethanol burner has a wick with a rectangular cross section of 12 x 2 mm² and a combustion rate of 0.4 mL/min. For a demonstration of the process, a reference sample of a 10 x 10 mm² Si substrate and a Si substrate with a 60 nm copper layer of the same size was used (Figure 4.4). The sample to grow CNFs with the 60 nm copper layer was covered with 2 µL of a 20 mg/mL $NiCl_2$ solution in ethanol and dried in air for few minutes. Both substrates were placed vertically in the ethanol flame at a height of 2 mm measured from the top of the wick.

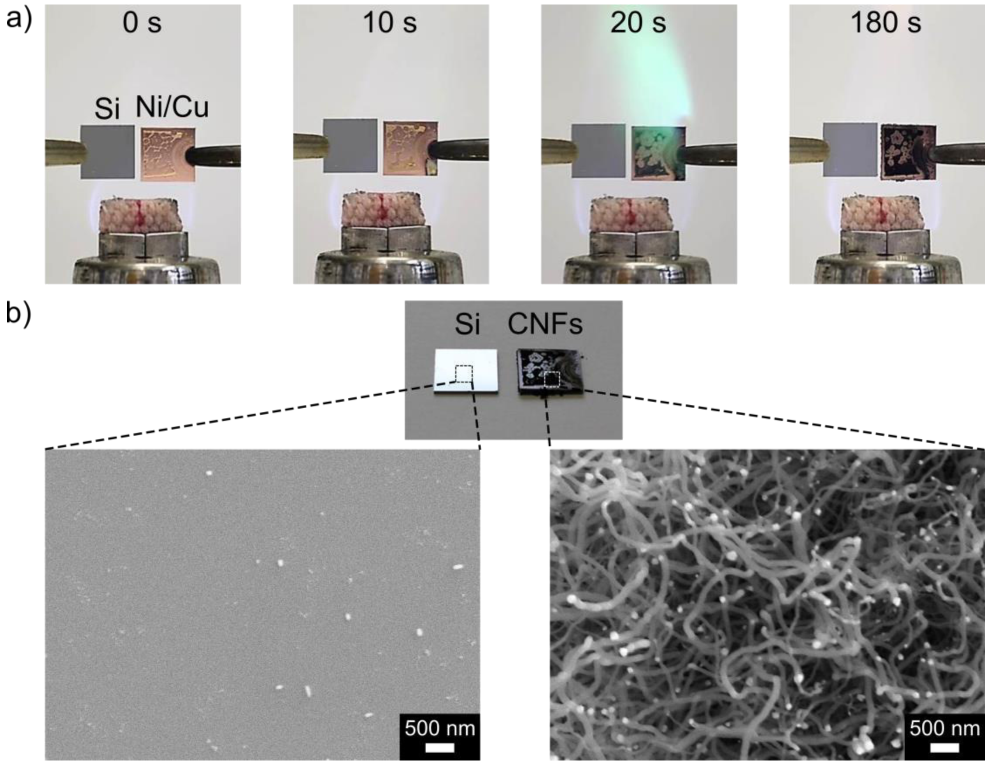

Figure 4.4: CNF growth experiment using an open ethanol flame. a) The time series shows a CNF growth experiment with a Si sample as a reference (left sample) and a Cu substrate with $NiCl_2$ catalysts (right sample) in an ethanol flame. The flame went green after 20 s over the Ni/Cu sample indicating that the $NiCl_2$ is reduced to pure state. b) After 180 s in the ethanol flame, the reference Si substrate did not show CNF growth in the SEM, whereas the Ni/Cu sample revealed some black areas which are identified as CNFs in the SEM.

The growth time of the experiment was 3 minutes. A series of four photos taken at different times (Figure 4.4 a) shows changes of the sample prepared with nickel catalysts. The unprepared reference sample, which consists of pure silicon, does not change the color in the ethanol flame and does not reveal any kind of nanostructures in SEM images (Figure 4.4 b). However, the prepared sample with $NiCl_2$ on a 60 nm copper layer changes the color to black after 20 s in the ethanol flame. It is also visible that the ethanol flame went green over the Ni/Cu sample, which starts after a few seconds in the ethanol flame and goes on for about 20 s. This change in the color might indicate that $NiCl_2$ reduces to a pure state and CNFs starts to grow. After 180 s, the complete area covered with $NiCl_2$ turned black and SEM investigations revealed CNFs growth in random directions. At the end of the CNFs, bright spots can be observed under the SEM, which indicates nickel catalysts and subsequently CNF growth after the tip growth model (see Chapter 2.1.2).

Temperature measurements with a thermocouple (Figure 4.5) revealed a temperature of ~750 °C at the sample center position. The height is measured starting from the wick of the ethanol burner in vertical direction. The temperature increase with height and the temperature ranges from 300 °C (directly over the wick) to 1000 °C at a height of 30 mm over the wick. The height, where the sample is placed, is between 2 and 12 mm over the wick, using a standard sample of 10 x 10 mm^2 placed from the lower edge of the sample 2 mm over the wick in vertical direction. However, the temperature gradient over the whole sample is not constant. That area of the ethanol flame was chosen due to the blue color of the ethanol flame at this position, which assumable contains more carbon from the ethanol which is not burned and can be used for CNF growth.

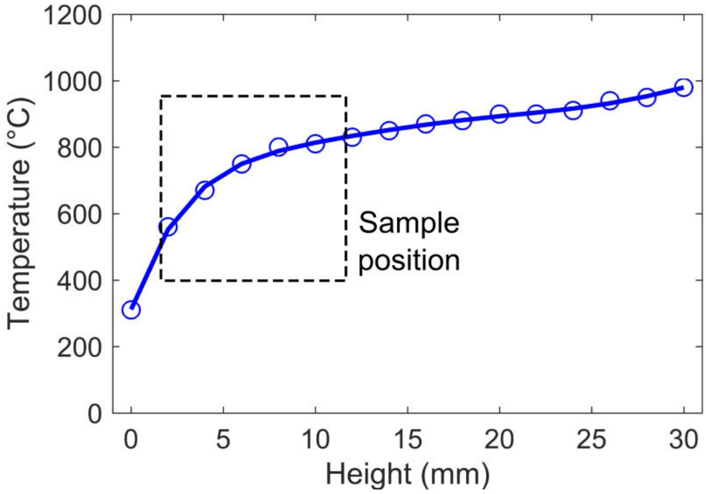

Figure 4.5: Temperature distribution of the ethanol flame measured with a thermocouple. The height is measured starting from the wick of the ethanol burner in vertical direction. The temperature rise with the height and the temperature range is from 300 °C (directly over the wick) to 1000 °C in a height of 30 mm over the wick. The height where the sample is placed is between 2 and 12 mm over the wick, using a standard sample of 10 x 10 mm² placed from the lower edge of the sample 2 mm over the wick in vertical direction.

4.3.2 The role of nickel chloride

To grow CNFs in an open ethanol flame is still a challenge, even if the best material combination with $NiCl_2$ catalysts on copper substrate (see Chapter 4.2) is used. The first challenge before CNF growth can start is to cover the sample with a thin layer of $NiCl_2$ from a 20 mg/mL ethanol solution. If the catalytic layer is too thin, no CNFs will grow due to a lack of catalytic material. However, if the catalytic layer is too thick also no CNFs can grow due to agglutination of the catalytic material forming thick layers instead of tiny islands of catalyst which are necessary to grow CNFs (see Chapter 2.1.3). It was observed that dip coating is a very precise way to cover the sample with a uniform thick layer of nickel catalysts. During dip coating, the layer thickness h_0 can be influenced by the dip coating velocity v as predicted by the Landau-Levich-Derjaguin theory ($h_0 \sim v^{\frac{2}{3}}$) [169], [170]. It states that a higher dip coating velocity leads to a higher layer thickness. It was observed that a dip coating velocity of about 10 mm/min is a suitable velocity to deposit a layer of about 50 nm of catalytic material from the $NiCl_2$ solution. Shortly after the sample is dip-coated with a uniform liquid catalytic layer, the ethanol evaporates leaving some $NICl_2$ arrays on the sample. These areas covered with $NiCl_2$ change their color to black after the ethanol flame synthesis (Figure 4.6). The black parts are identified as CNFs under the SEM. The black appearance of the CNF arrays can be explained with the high light absorption properties of CNTs and CNFs [171].

A detailed AFM topography investigation was conducted to determine the difference between CNF and no CNF growth. Figure 4.7 a) shows two AFM topography scans of a dried $NiCl_2$ layer. The dried $NiCl_2$ have the size of spheres with diameters between 100 – 200 nm. Normally, on the edges of the $NiCl_2$ layer no CNF growth was observed in the SEM images. This can be explained with a lower or higher layer thickness than those necessary to grow CNFs. Therefore, a sample with $NiCl_2$ dip coated on a copper substrate was exposed to an ethanol flame, but for only 20 s. Figure 4.7 b) shows two AFM scans of the edge region after 20 s in the ethanol flame. It is obvious, that catalytic centers occur but agglutinate together with sizes of up to several 100 nm, which is too big to grow CNFs in the flame synthesis process. Figure 4.7 c) shows two AFM scans at the center of a $NiCl_2$ layer where CNFs growth was typically observed. In this region catalytic centers occur in a size between 20 – 120 nm, which is in the suitable range for catalytic centers.

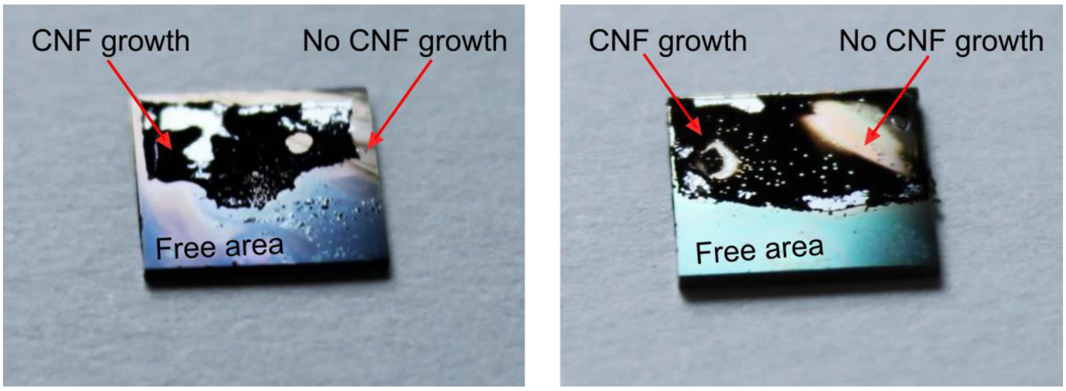

Figure 4.6: Samples with CNFs grown with ethanol flame synthesis from $NiCl_2$ on Cu substrates. The $NiCl_2$ was deposited on one part of the sample by dip coating, the $NiCl_2$ free region is marked as ‘free area’ in the images. During drying of the $NiCl_2$, patterned arrays with $NiCl_2$ free areas appear. The arrays covered with $NiCl_2$ are black after flame synthesis due to CNFs growth. No CNF growth was observed in the $NiCl_2$ free area.

4.3.3 Influence of lab humidity

During flame synthesis of CNFs using an open ethanol flame, the environmental conditions, such as humidity and temperature play an important role. These conditions are decisive for CNF growth. The absolute humidity ρ_w in kg/m³ can be calculated by:

$$\rho_w = \frac{e}{R_w T}. \tag{4.3}$$

Where e the vapor pressure in Pa and R_w the gas constant of water vapor with 461.5 J/(kgK) [172]. The relative humidity φ in % is defined as the ratio between vapor pressure and the saturation vapor pressure E in Pa.

$$\varphi = \frac{e}{E} 100\% \tag{4.4}$$

The saturation vapor pressure dependent on the temperature and can be calculated using the August-Roche-Magnus Equation after Lawrence *et al.* [172]:

$$E(t) = (610.94Pa)e^{\left(\frac{17.625t}{243.04°C+t}\right)}. \tag{4.5}$$

With the temperature t in °C. Subsequently, the absolute humidity can be calculated with the temperature and the relative humidity from:

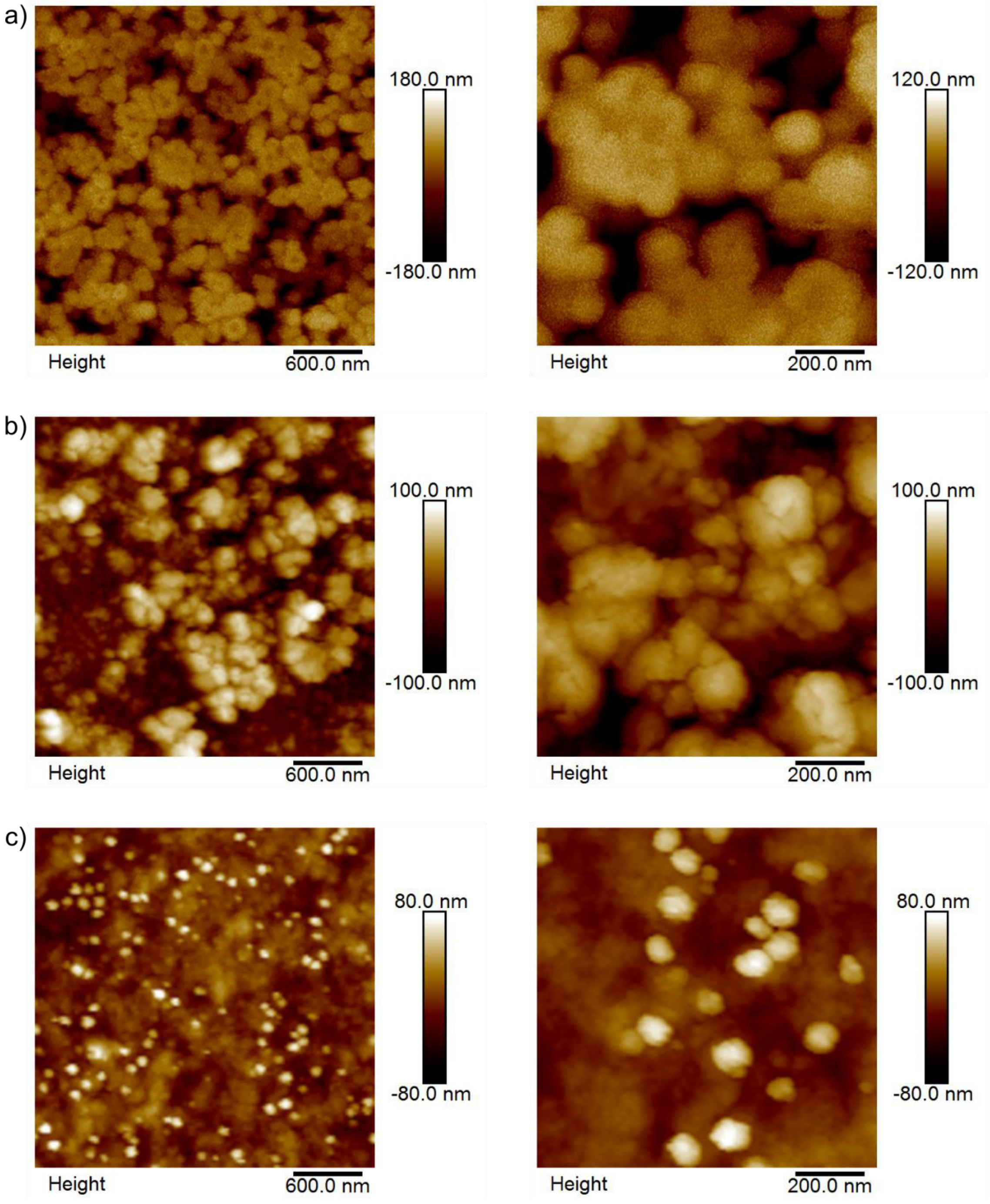

Figure 4.7: AFM investigation of pure $NiCl_2$ and catalytic centers from the $NiCl_2$ after 20 s in an ethanol flame. a) A $NiCl_2$ from a $NiCl_2$ solution of 20 mg/mL in ethanol dip coated on a Si-substrate with a top layer of 50 nm copper after drying on a hotplate for 1 min by 80 °C. b) The arrays without CNF growth do not exhibit catalytic centers in a suitable size for CNF growth after 20 s in the ethanol flame. c) Whereas the arrays with CNF growth exhibit catalytic centers in a suitable size (20 nm – 120 nm) after 20 s in the ethanol flame.

$$\rho_w = \frac{\varphi(610.94Pa)e^{\left(\frac{17.625t}{243.04°C+t}\right)}}{(100\%)R_wT}. \tag{4.6}$$

Where T is the temperature in Kelvin. The absolute humidity dependent on the temperature with different relative humidities (20 – 100 %) calculated with Equation (4.6) is plotted in Figure 4.8. Around 30 CNF growth experiments conducted at different ambient conditions were evaluated concerning CNF growth. Figure 4.8 shows the diagram with CNF growth (green circles) and no CNF growth (red triangles).

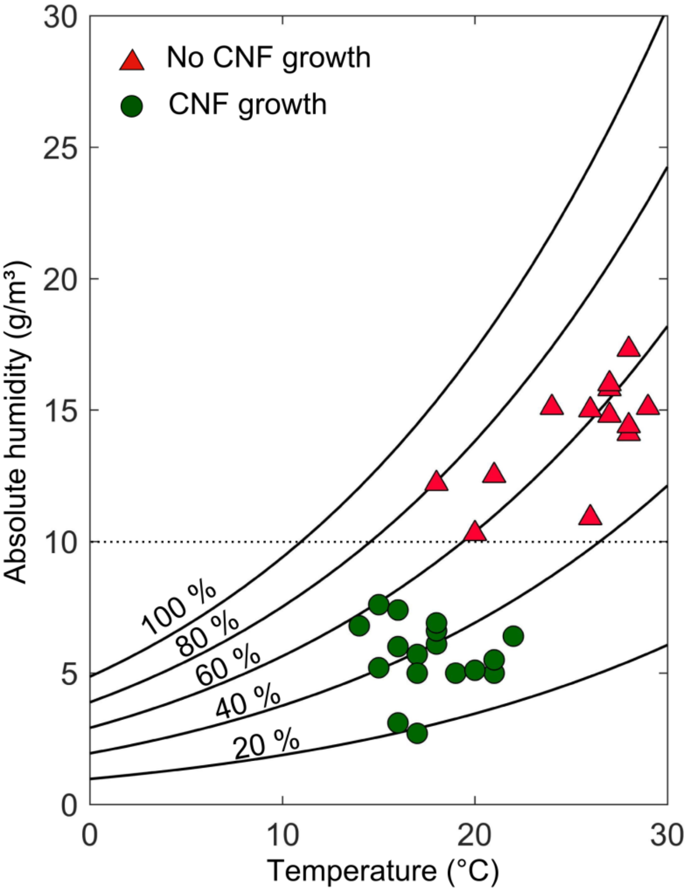

Figure 4.8: Humidity-temperature diagram with successful CNF growth experiments (green circle) and no CNF growth (red triangles). All 30 experiments were conducted over one year in a not air-conditioned lab, resulting in a great range of temperatures and humidities. It was observed that the relative humidity, which is represented by the lines in the diagram from 20 – 100 %, is not a suitable parameter to distinguish between CNF growth and no CNF growth. Rather the absolute humidity is a suitable parameter. CNF growth experiments above an absolute humidity of 10 g/m³ were not successfully, whereas experiments below this limit lead to CNF growth.

It was observed that the absolute humidity is a more suitable parameter compared with the relative humidity or temperature to destinguish between CNF growth and no CNF growth. All CNF growth experiments conducted below an absolute humidity of 10 g/m³ were sucesful whereas all experiments above this limit do not show any CNF growth. A possible explanation for this is, that the used metal salt $NiCl_2$ is hygroscopic. This results in condensed water from the environment on the nickel salt. The critical point where water condensation from the surrunding air starts on the metal salt is 20 °C and a relative humidity of 54 % [173]. Using Equation (4.6), this leads to an absolute humidity of 9.3 g/m³, which is close to the absolute humidity limit to grow CNFs in flame synthesis using $NiCl_2$ on copper substrates of 10 g/m³ obtained from the experiments. A possible assumption is, that the condensed water oxidize the 50 nm copper layer before CNF growth starts. A basic experiment was conducted to discover, if this theory is valid. Therefore, two identical samples, which are used for CNF growth with a 50 nm copper layer on a Si substrate, were covered with 1 µL of a 20 mg/mL $NiCl_2$ solution in ethanol and dried by 80 °C on a hotplate for 1 minute. This results in a thin $NiCl_2$ layer on the copper surface (Figure 4.9). The two identical prepared samples were exposed to different ambient conditions. The sample in a) was exposed the lab conditions with 20 °C and a relative humidity of 16 %. The sample in b) was exposed to 40 °C and a relative humidity of 64 %. Therefore, a closed system with the sample and a water reservoir was heated over a hotplate to 40 °C, resulting also in an increased humidity. After 10 minutes under these ambient conditions, small changes in the color of the $NiCl_2$ exposed to higher temperature and humidity can be observed and after 2 h this sample is oxidized in the area covered with the $NiCl_2$. However, the sample at lower temperature and humidity did not show any changes in color. After 2 h exposed to different ambient conditions, both samples are washed under deionised water for 1 minute and dried in air to get rid of the $NiCl_2$. It is obvious that the copper layer of the sample exposed to the 20 °C and 16 % relative humidity environmant still exists, whereas the copper layer of the sample exposed to the 40 °C and 64 % relative humidity environment got dissolved completely due to oxidation on the area covered with the $NiCl_2$. The copper layer only exists on the edge region where no $NiCl_2$ was deposited. This is experimental evidence that the copper layer oxidizes on the area covered with $NiCl_2$ at high temperatures and humidities. Subsequently, the copper layer which is necessary to grow CNFs does not exist anymore and the experiments are not successfull. Therefore, low lab temperatures and humidities are needed to conduct successfully CNF growth experiments with flame synthesis using $NiCl_2$ on copper layers.

4.3.4 Influence of the magnetic field

Magnetic fields were applied to align the CNFs during growth by two different magnets. Zhang and Pan [120] used a similar setup compared to those represented in my work, where the magnet was placed over the flame protected by a shield (see Figure 2.9 a). However, it was observed in this work that the magnet and the shield can be placed beside the ethanol flame resulting in less heating of the magnet because the hot air rises upwards, resulting in a magnet temperature of only 40 °C after 3 minutes exposed to the ethanol flame. This temperature is still in a suitable range where the magnet does not degrade (<80 °C). The magnet, to align the CNFs during growth, was built of five neodymium magnets from Maqna Otom Group GmbH with a diameter of 25 mm, a thickness of 3 mm and a grade of 45. The magnetic flux B of a cylindrical magnet at a distance z away from the magnets pole can be calculated from:

$$B = \frac{B_r}{2}\left(\frac{D+z}{\sqrt{R^2+(D+z)^2}} - \frac{z}{\sqrt{R^2-z^2}}\right), \tag{4.7}$$

where B_r is the remanence of the magnetic material, D is the height of the cylindrical magnet and R the corresponding radius [174]. The magnetic flux of the surface ($z = 0$) of the built magnet with a remanence of the magnetic material of a N45 neodymium magnet of 1.32 T [175] was calculated to 506 mT.

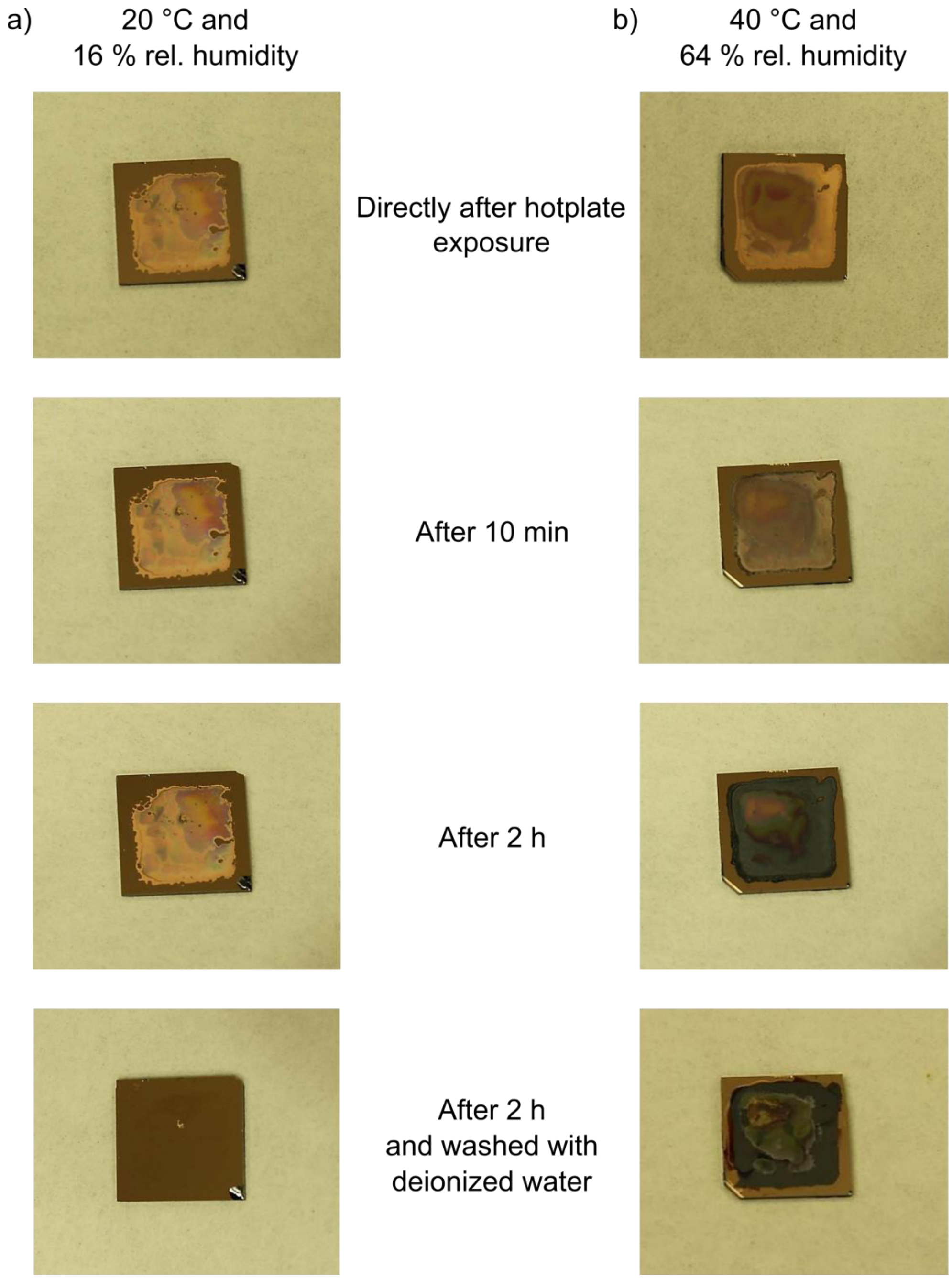

Figure 4.9: Oxidation of 50 nm copper layers covered with $NiCl_2$ and exposed to different ambient conditions. A droplet of 1 µL of a 20 mg/mL solution of $NiCl_2$ in ethanol was brought on two samples with a 50 nm copper layer on a Si substrate and dried at 80 °C on a hotplate for 1 min. The sample in a) was exposed to a relative humidity of 16 % at 20 °C and the sample in b) was exposed to a relative humidity of 64 % at 40 °C. After 10 min under different ambient conditions, small changes in the color of the sample exposed to higher temperature and humidity can be observed and after 2 h it is obvious that the sample exposed to a higher relative humidity and temperature oxidized on the area covered with $NiCl_2$. After washing the samples under deionized water for 1 min and drying in air, the thin copper layer of the sample exposed to the lower temperature and humidity still exist whereas the copper layer of the sample exposed to the higher temperature and humidity dissolved nearly completely on the area covered with $NiCl_2$ due to oxidation.

In a CNF growth experiment, the distance between the magnet surface and the sample surface was 3 mm, resulting in a magnetic flux on the sample's surface of 387 mT. A piece of a silicon wafer was placed vertically aligned between magnet and sample to prevent, that the magnet heats up to fast.

Using no magnet and applying no magnetic field to the experimental setup leads to randomly aligned CNFs (Figure 4.10 a). The growth follows the tip growth mechanism (see Chapter 2.1.2) due to the location of the catalysts at the end of the nanofibers. The catalysts are the bright spots at the end of each nanofiber which can be seen in the SEM images. As nickel is the only used material which can grow CNFs, the catalytic centers at the end of each CNF are most likely made of nickel [176] or an alloy of Ni and Cu. CNT growth experiments using Si, SiO_2 and Cu but without Ni do not show CNF growth. Applying the magnet described above, leads to a better orientation of the CNFs (Figure 4.10 b).

a) Random CNFs (without magnet)

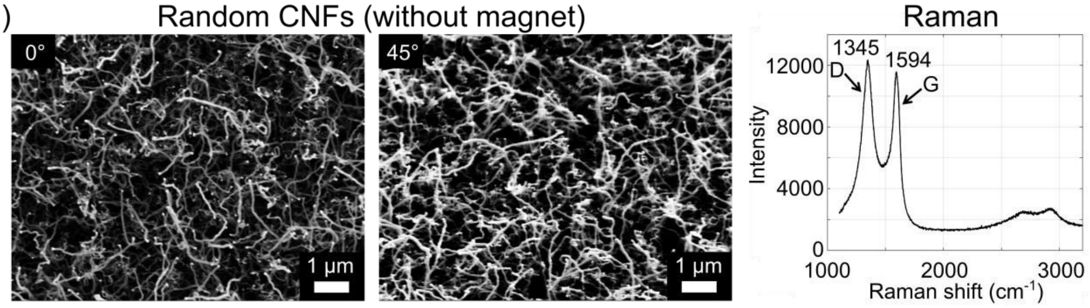

b) Oriented CNFs (with magnet)

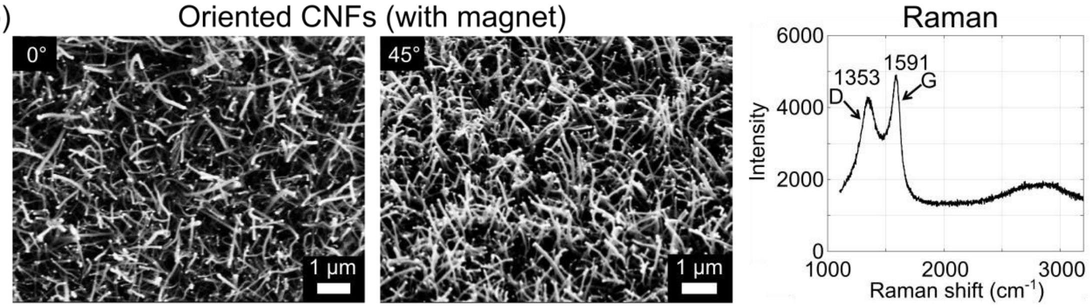

Figure 4.10: SEM images and Raman spectra from the grown CNFs. a) Random CNFs grown without a magnet and b) oriented CNFs grown with a magnet. The SEM images showing the CNFs under different angles with the top view 0° on the left side and a 45° tilted view in the middle. The Raman spectra were obtained using a laser excitation of 532 nm. Both structures show the characteristic D and G bands for carbon materials such as CNFs.

The CNF orients away from the magnetic field. The alignment is assumably due to CNFs diamagnetism [177]. The alignment of CNFs due to paramagnetism of the Ni catalysts is less likely. In general, a ferromagnetic force of the Ni catalysts acts in the direction of the magnet. However, the temperature in the ethanol flame is with about 750 °C higher than the Curie temperature of Ni at 358 °C [167], making ferromagnetic forces impossible. The force acting on the Ni catalyst at this temperature range can only be a paramagnetic force, which is much smaller than the ferromagnetic force. However, the CNFs are diamagnetic, leading to a diamagnetic force on the CNFs away from the magnet. The forces acting during CNF growth are depicted in Figure 4.1. Due to the observation, that the CNFs are mostly oriented away from the magnet, leads to the conclusion that the diamagnetic forces acting on the CNFs are higher than the paramagnetic forces acting on the Ni catalysts.

A better alignment during CNF growth was achieved by using a stronger permanent block magnet, in this case a neodymium block magnet (50x50x30 mm³) with a grade of N52 from MTS Magnete (Germany). For a block magnet, the magnetic flux B at a distance z away from the magnets pole can be calculated with:

$$B = \frac{B_r}{2}\left[\tan^{-1}\left(\frac{LW}{2z\sqrt{4z^2 + L^2 + W^2}}\right) - \tan^{-1}\left(\frac{LW}{2(D + z)\sqrt{4(D + z)^2 + L^2 + W^2}}\right)\right], \tag{4.8}$$

where B_r is the remanence of the magnetic material, L is the length of the block magnet, W is the width of the block magnet and D is the height of the block magnet [178]. This leads to a surface flux of 508 mT for the used magnet calculating with a remanence of the magnetic material of 1.42 T [175]. A similar substrate was used as for the previous experiments, with 60 nm copper on a part of a SiO_2 wafer. For a homogeneous layer of catalytic material, a dip-coating process was used with a $NiCl_2$ solution in ethanol (20 mg/mL) by using a velocity of 10 mm/min for the dip-coating. After drying of the sample at ambient conditions, the sample was placed in the ethanol flame at a height of 3 mm over the wick and in a distance between magnet surface and sample of 3 mm. This experimental arrangement leads to a calculated magnetic flux of 453 mT on the surface of the sample. Figure 4.11 shows vertically aligned CNFs after a growth time of 30 minutes.

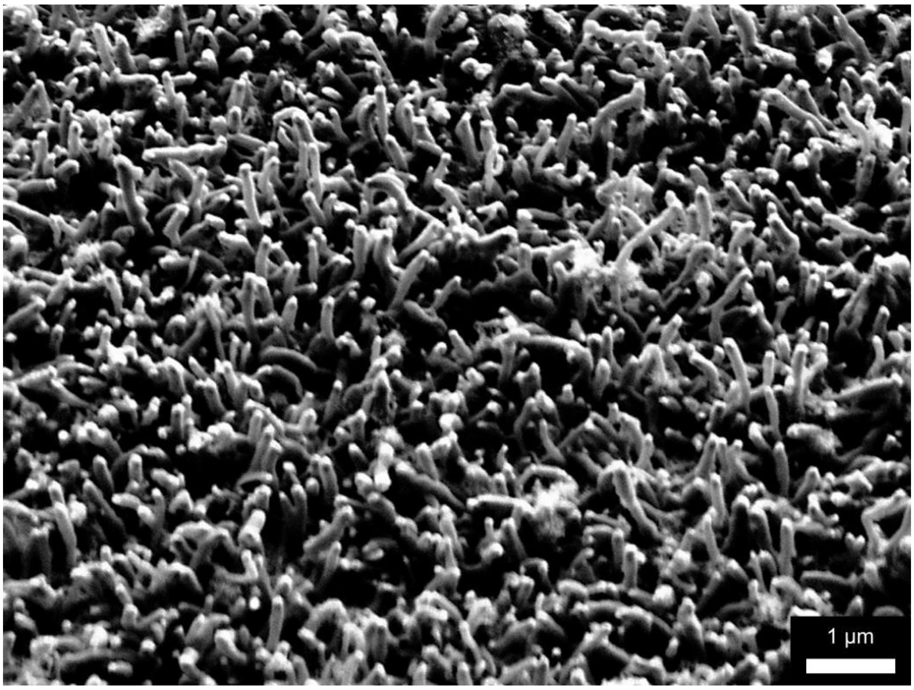

Figure 4.11: Mostly aligned CNFs using a block magnet with a magnetic surface flux of 508 mT. The substrate consisted of a piece of a SiO_2 wafer covered with 60 nm Cu dip coated in a $NiCl_2$ solution in ethanol (20 mg/mL). The dip coating velocity was 10 mm/min to achieve a constant catalytic layer. The sample was placed directly in the ethanol flame at a height of 3 mm over the wick and 3 mm away from the block magnet measured from the samples surface, resulting in a magnetic flux on the samples surface of 453 mT. The growth time was 30 minutes. Most of the CNFs show a more or less vertical alignment.

It was observed, that applying a stronger magnetic field leads to better aligned CNFs. However, the time to grow CNFs with a length in the range between 1 and 2 µm is ten times higher compared to the smaller magnet.

To determine the catalytic material at the top of the CNFs, a basic experiment at room temperature was conducted. For that, grown CNFs were scratched off from the substrate in a glass with ethanol and agitated to achieve a homogeneous solution (Figure 4.12 a). The cylindrical magnet from stacking five cylinder magnets together was places outside the glass directly on the glass wall (Figure 4.12 b-c). Independent from the orientation of the magnet, the CNFs drift towards the magnet. However, placing the magnet with the polar side to the glass wall leads to a better attraction of the CNFs. The strongest attraction to the CNFs showed the block magnet (Figure 4.12 d) indicated with the black CNFs on the inner edge of the glass.

These finding evidences that the catalytic centers on the top of the CNFs contains nickel, because nickel is the only used material with ferromagnetic properties in the CNF structure. This results in a ferromagnetic force from the nickel catalysts to the magnet. A small diamagnetic force can act to the CNFs away from the magnet. However, this force is subsequently smaller than the ferromagnetic force on the nickel catalysts due to the attraction of the structures to the magnet (see Figure 4.12).

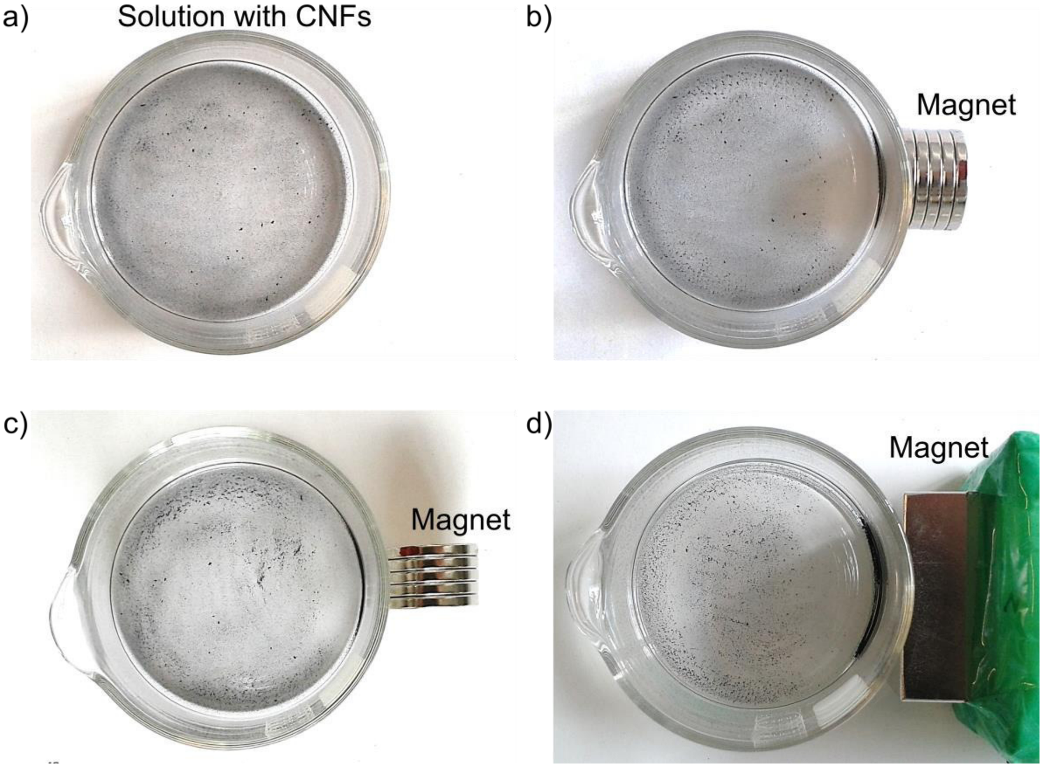

Figure 4.12: Influence of magnets at room temperature on the grown CNFs solved in ethanol. a) Grown CNFs were solved in ethanol in a lab glass. A cylindrical magnet was placed beside the glass with b) the polar side and c) the axial side. It was observed that the CNFs drift in the direction of the magnet in both cases. However, more CNFs drift to the magnet applying the polar side to the glass wall. d) A stronger block magnet was placed beside the glass resulting in much more CNFs drift to the magnet. This finding indicates that the catalytic centers on the top of the CNFs are made by nickel, resulting in a ferromagnetic force in the direction of the magnet. However, a small diamagnetic force can act on the CNFs away from the magnet.

4.3.5 Geometry and properties of the CNF arrays

In this section the geometry and properties of the CNF arrays from Figure 4.10 are investigated in more detail. The SEM images revealed that the grown CNF arrays have diameters between 40 and 80 nm. The length of the CNFs is about 3 µm for a 3 min growth experiment leading to a growth rate of 1 µm/min. The heights of the CNF arrays measured from the substrate surface to the end of the CNFs with the catalytic centers are about 2 µm for randomly aligned CNFs and about 3 µm for aligned CNFs. Raman measurements were conducted with the help of Sharali Malik by using a Renishaw inVia Raman microscope working at an excitation wavelength of 532 nm to obtain information of the material and quality of the grown CNFs. Both CNF structures under test show the characteristic D and G bands. Aligned CNFs reveal D = 1353 cm^{-1} and G = 1591 cm^{-1}, whereas randomly aligned CNFs reveal D = 1345 cm^{-1} and G = 1594 cm^{-1}. These peaks are identical as those for carbon materials such as CNFs and CNTs [179]. The D/G ratio of the intensities for aligned CNFs was 0.87 and 1.06 for randomly aligned CNFs. This indicates that the aligned CNFs belongs a higher graphitic degree of ordering and subsequently less defects in the graphene structure compared with random aligned CNFs.

A X-ray photoelectron spectroscopy (XPS) measurement was conducted with the help of Michael Bruns for randomly aligned CNFs to determine the material properties and chemical arrangement of the grown nanostructures. Therefore, a K-Alpha+ XPS from Thermo Fisher Scientific and a Thermo Advantage software (described in [180]) for data transfer and processing were used. The sample was investigated with a monochromated Al K α X-ray source with a micro-focused spot size between 30 and 400 µm. For the measurement, a charge compensation system from K-Alpha with 8 eV electrons and argon ions of low energy was used to prevent the building of charging effects. Voigt profiles were used to fit the spectra. The spectra for the C1s hydrocarbons with 285.0 eV were referenced by using the well investigated photoelectron peaks of the metallic Cu, Ag and Au. Before the measurement, the sample was cleaned from organic contaminations by using a Thermo Scientific MAGCIS (Mono Atomic and Gas Cluster Ion Source) operating at 8 keV with Ar_{1000}+ clusters. Figure 4.13 a) shows the XPS result with the experimental data points marked with cycles and a fit of the data points (blue solid line). The experimental data was divided into C graphite sp^2 (blue solid line) and adventitious carbon sp^3 (blue dashed line). The C1s main peak was at 284.4 eV, which is the evidence for graphitic carbon (sp^2). The measurement results fit with XPS investigation of CNTs and CNFs from the literature [181], [182]. The adventitious carbon with the weak peak at 285.0 eV compared with C graphite occurs due to hydrocarbon contamination from exposing the CNFs to ambient atmosphere.

Additionally to the XPS investigation, some samples were investigated by high-resolution transmission electron microscopy (HRTEM). These measurements (Figure 4.13 b) were conducted with the help of C. N. Shyam Kumar and Christian Kübel using a FEI Titan 80-300 and a Gatan US1000 CCD camera. Therefore, the investigated nanostructures were scraped from the silica sample to copper grids from Quantifoil. The HRTEM operated at an acceleration voltage of 80 kV. The HRTEM images revealed that some CNFs have a hollow core. The ordering of the graphite layers is from their appearance more similar to herring bone structures. Considering all results of the CNFs investigation with SEM, Raman, XPS and HRTEM, the grown nanostructures can be identified as 1D-CNs. Most of them are CNFs with a minor part of CNTs.

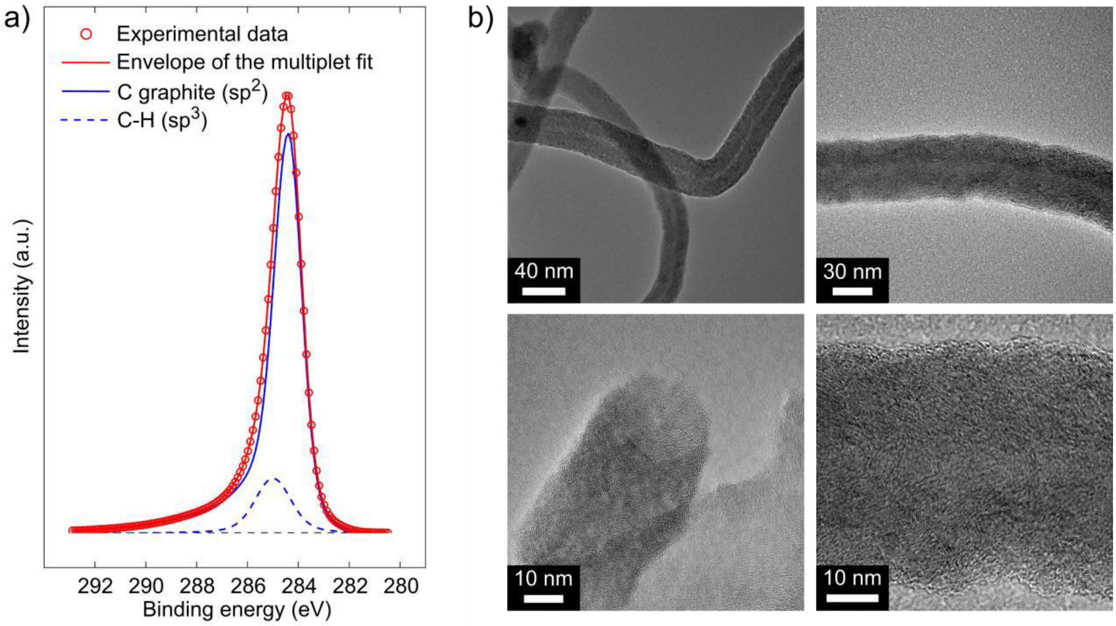

Figure 4.13: XPS and HRTEM characterization of the grown CNFs. a) The XPS measurement (blue solid line) shows the C1s XP spectrum with a peak at 284.4 eV, indicating graphite (sp^2). A weak peak at 285.0 eV (blue dashed line) indicates adventitious carbon (sp^3) caused by hydrocarbon contamination from the contact of the sample with the ambient atmosphere. b) HRTEM images of different CNFs show the graphitic layer and partially CNFs with a hollow core.

4.4 Adhesion properties of CNF arrays from ethanol flame synthesis

CNF arrays using ethanol flame synthesis were produced with different alignments obtained by magnetic-field enhanced growth (see Chapter 4.3.4). The fabricated CNF arrays were investigated for their adhesion properties by AFM. In this section, the measurements reveal a linear increase of the adhesion force and energy by increasing the preload force. The CNF arrays aligned by the magnetic-field reveal 68 % higher adhesion compared with random aligned CNF arrays. Additionally, endurance tests are performed with AFM. Both CNF arrays do not show any kind of damage after 50 000 measurement cycles.

4.4.1 AFM based adhesion measurements

For the AFM based adhesion measurements, an AFM from Bruker (Dimension Icon) was used to obtain the force-distance diagrams. Therefore, a tipless cantilever made from silicon was mounted with a 20 µm SiO_2 sphere, pressed into the surface under test and lift-off. During pressing the silica sphere into CNFs, a bending on the cantilever occurs. A laser beam focused on the cantilever detects the bending and a software calculates the force from the bending over the spring constant. This approach to measure the adhesion was used by Röhrig *et al.* [32] due to their defined contact area and subsequently comparable results of the adhesion measurements. For mounting the sphere to the cantilever a tiny amount of glue was used as described in Chapter 2.2.3. A SEM investigation confirmed that glue contamination on the top of the SiO_2

sphere was avoided in this way. The ramp rate for the adhesion measurement was set to 1.5 µm/s, for all measurements shown here. However, it was observed that the results from the adhesion measurements are fairly independent from the ramp rate. Measurements using ramp rates between 0.2 and 8 µm/s lead to similar adhesion values. The thermal tune method [156] was used to determine a spring constant of 7.74 N/m for the used cantilever. The adhesion forces and energies were calculated as previously described in Chapter 2.2.4.

To achieve comparable results of the adhesion measurements, all measurements presented in this chapter were conducted with the same cantilever. The insert in Figure 4.15 shows a SEM image of the fabricated AFM cantilever mounted with a 20 µm SiO_2 sphere. An AFM was used for the adhesion measurement of the CNF arrays due to the not completely covered CNF arrays caused by the production process (see Chapter 4.3.2). Additionally, an AFM offers the opportunity to conduct adhesion measurements in the nN-range. Adhesion measurements were conducted for randomly and aligned CNF arrays. In addition to the CNF arrays, a reference sample was produced. The reference sample was placed in the ethanol flame for the same time as the sample with CNFs but without catalysts, resulting in a flat copper sample as a reference. This approach was used to show that the ethanol flame does not cover the sample with any kind of sticky secretion which could influence the adhesion measurement. Figure 4.14 shows measured force-distance diagrams for a) the reference copper surface, for b) the randomly aligned CNFs and c) for aligned CNFs. Each force-distance curve consists of two parts with trace (blue dashed line) and retrace (red solid line). Trace contains information about the approach with the preload force and retrace gives information about the withdraw with adhesion force and energy. A constant preload force of 2 µN was used for all three measurements. The adhesion force is the lowest negative force obtained from the retrace curve and describes the force which is necessary to lift the sphere on the cantilever from the CNF surface. The adhesion energy is the area in the force-distance diagram between the zero line and the retrace curve. It describes the energy to lift the sphere on the cantilever from the CNF surface. Aligned CNF arrays showed the highest adhesion forces and energies, followed by randomly aligned CNF arrays. Whereas the reference copper sample showed the lowest adhesion properties.

The influence of the preload force on the adhesion force and energy was investigated by conducting six adhesion measurements for each preload force on different positions of the sample to calculate a mean value of the adhesion force and energy. Therefore, a preload force range between 0.2 and 4.0 µN with 0.2 µN steps was investigated. Figure 4.15 shows a) the adhesion force and b) the adhesion energy for aligned CNFs (blue squares), randomly aligned CNFs (red triangles) and the reference copper sample (green circles). Six measurements were conducted for each preload force at different positions and the error corresponds to the respective standard deviation.

Differences in the quality and density as well as inhomogeneous alignment of the CNFs on different areas of the sample lead to a scatter of the measured adhesion force and energy. In general and independent of the preload force, the adhesion forces and energies for the aligned CNFs are higher than those of randomly aligned CNFs and the reference copper sample. However, there is a small range of preload forces (< 1 µN) where the reference copper sample shows similar or higher adhesion properties than the CNF arrays. This can be explained with the low preload force, which leads to a larger contact area for the reference sample but only a few CNFs are contacted by the silica sphere on the AFM cantilever.

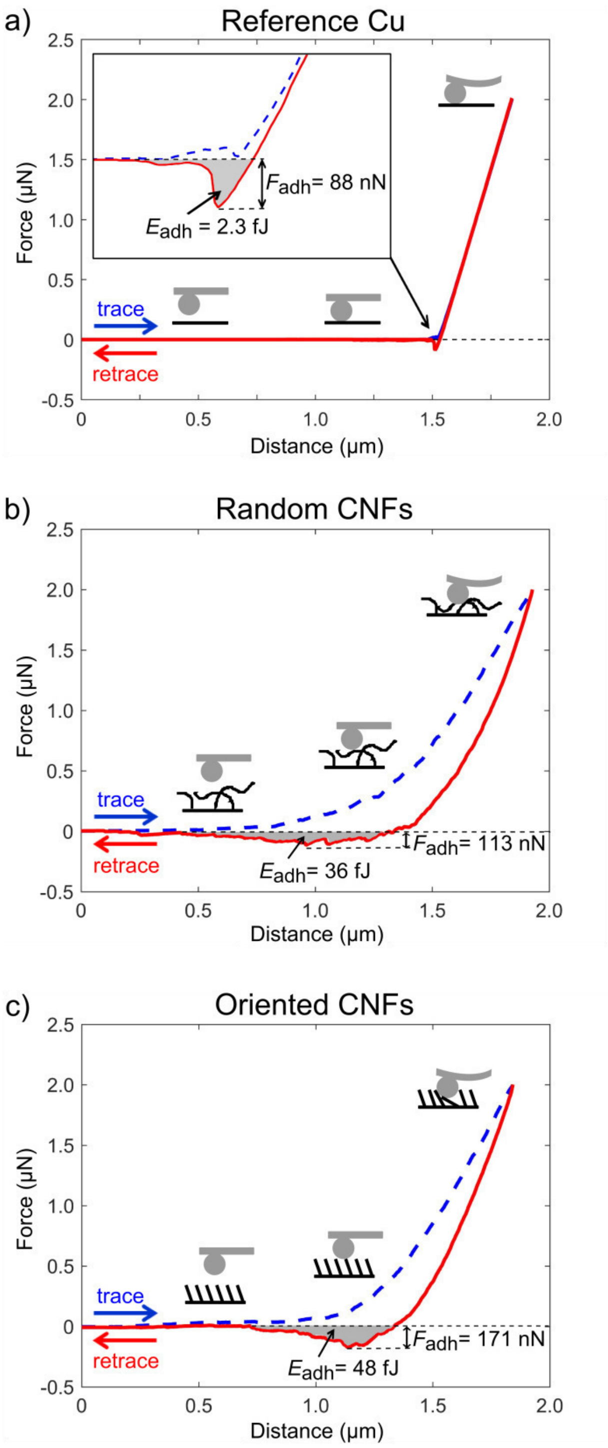

Figure 4.14: AFM based force-distance diagrams from adhesion measurements. The force-distance diagrams are obtained during an approach, the so-called trace (blue dashed line) and a lift off, the so-called retrace (red solid line). These two parts built a measurement cycle. The adhesion measurements were conducted with a 20 µm silica sphere glued on an AFM cantilever. The used preload force was 2 µN for all three measurements of a) the reference consisting of a flat copper surface, b) random CNFs and c) oriented CNFs. The diagrams contains the adhesion force (F_{adh}) and the adhesion energy (E_{adh}). It is obvious, that oriented CNFs have higher adhesion properties than random CNFs and the reference copper surface.

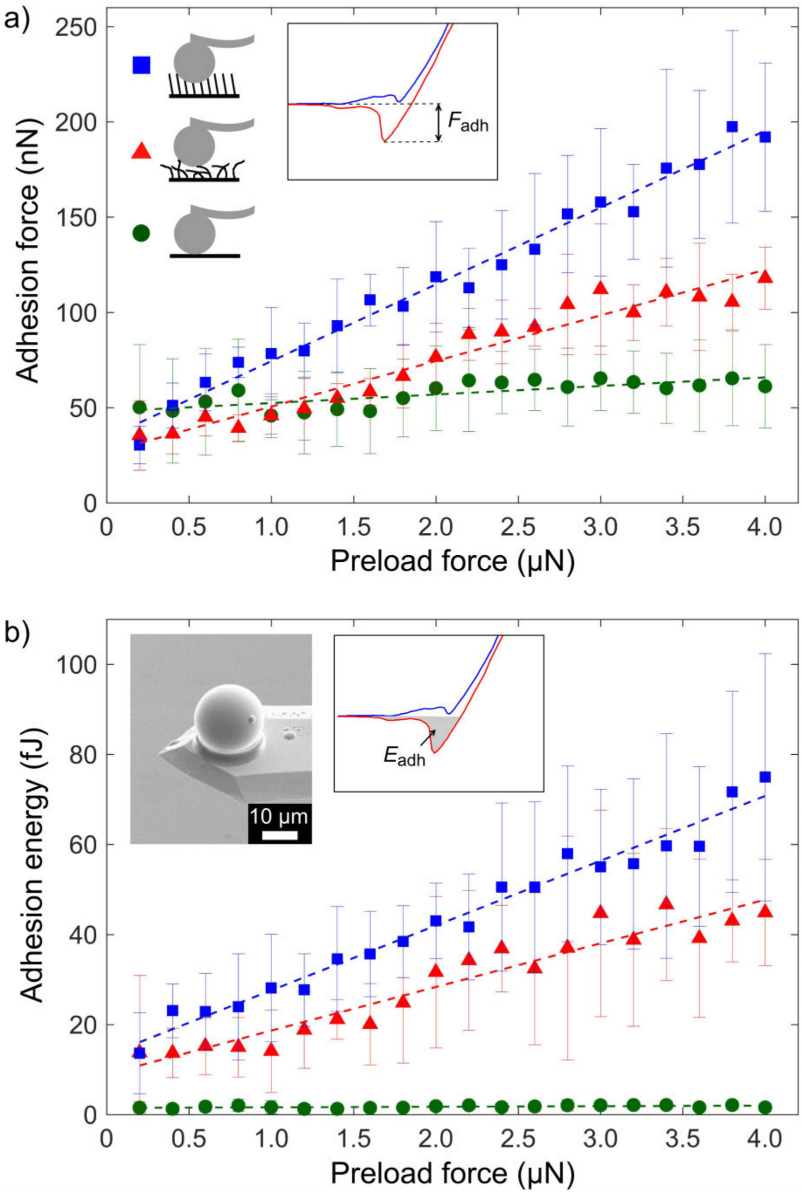

Figure 4.15: Evaluation of the adhesion measurements, with a) the adhesion force and b) the adhesion energy over the preload force. Representing the averaged measurement points for oriented CNF arrays (blue squares), random CNFs arrays (red triangles) and the copper reference surface (green circles). The linear fits are visualized by the dashed lines. A SEM image of the 20 µm silica sphere (b) glued to an AFM cantilever used for the whole measurements is shown in the insert.

The adhesion forces and energies for the reference copper sample are nearly constant. The adhesion force is in the range between 50 and 60 nN and can be described as a function of the preload force: $F_{adh} = 0.004F_{pre} + 48nN$. The adhesion energy is in the range between 1 and 2 fJ and can be described as a function of the preload force: $E_{adh} = 0.0001(\frac{fJ}{nN})F_{pre} + 1.5fJ$. Whereas the adhesion of the CNF arrays rise linear with the preload force. For randomly aligned CNFs arrays, the adhesion force can be described by $F_{adh} = 0.024F_{pre} + 27nN$ and the adhesion energy by $E_{adh} = 0.007(\frac{fJ}{nN})F_{pre} + 9fJ$. For aligned CNF arrays, the adhesion force can be described by $F_{adh} = 0.040F_{pre} + 34nN$ and the adhesion energy by $E_{adh} = 0.014(\frac{fJ}{nN})F_{pre} + 13fJ$. Where F_{adh} is defined as the adhesion force in nN, E_{adh} is the adhesion energy in fJ and F_{pre} the preload force in nN.

The linear fits are depicted as the dashed lines in Figure 4.15. The increase in adhesion by increasing the preload force agrees with the investigation of adhesion behavior of CNTs by Ge *et al.* [183]. A higher preload force leads to more contacts between the CNFs and the silica sphere, leading to an increase in the adhesion force and energy.

In general, aligned CNFs reveal a 68 % higher adhesion force than randomly aligned CNFs, which can be explained by the contact splitting theory [20] (see Chapter 1.1). This increase in the adhesion force result from an increase in the number of contacts for aligned CNFs. The number of CNFs per area (density) was calculated from SEM investigations. Randomly aligned CNFs have a density on the top of the CNF layer of 5 CNFs/µm^2 due to CNFs laying over each other leading to less CNF contacts on the top. Whereas aligned CNFs have a density of 8 CNFs/µm^2. Therefore, aligned CNFs have more contacts with the silica sphere (see insert of Figure 4.16 a) and consequently higher adhesion forces and energies.

4.4.2 AFM based endurance adhesion measurements

Using dry adhesives in endurance applications, such as climbing robots, make it necessary to investigate the long term stability of the dry adhesives. However, endurance runs with dry adhesives from CNFs are normally limited to few cycles [184] due to their time consumption. In this section the endurance properties of arrays with aligned and randomly oriented CNFs were investigated to characterize these structures after their long term stability. Therefore, three endurance runs on different positions of the sample with up to 50 000 cycles of approach and retraction were conducted for both CNF arrays. For the endurance runs, a 20 µm silica sphere on an AFM cantilever was used with a constant preload force of 2 µN. The used ramp rate was 1 Hz, which means that one cycle consisting of an approach and retraction takes one second. Subsequently, 50 000 cycles leading to a measurement time of nearly 14 hours. Figure 4.16 shows the results of the endurance runs with a) the adhesion force and b) the adhesion energy for aligned CNFs (blue squares) and randomly oriented (red triangles). The adhesion forces and energies are nearly constant during the endurance runs with 50 000 cycles. The error bars represent the standard deviation. The insert in Figure 4.16 b) shows a SEM image of a CNF array after 50 000 cycles. The SEM image revealed no visible damage.

Similar to the adhesion investigation with varying the preload force (see Chapter 4.4.1), the aligned CNFs revealed higher adhesion forces and energies compared with randomly oriented CNFs. During the endurance runs, a maximum adhesion force of 280 nN was recorded for the sample with aligned CNFs. The contact area of the silica sphere with the CNFs was determined to 42 µm^2 with a penetration depth of 1 µm estimated from the force distance diagrams. This corresponds to an adhesion force referred to an area (see Chapter 2.2.5) of 0.66 N/cm^2. However, this value is still improvable compared with the adhesion of a real gecko of 10 N/cm^2 [5]. The adhesion properties can be increased by an improvement in the orientation of CNFs and smaller diameters of the CNFs leading to a rise in the adhesion after the contact splitting theory [19]. Another way to improve the adhesion properties, which is inspired by the hierarchical structures of a gecko (see Chapter 1.1) is to grow hierarchical CNFs, e.g., CNF structures featuring a Y-shape [48], [50]. The overall outcome of the endurance runs is, that both CNF structures, independent from their orientation, withstand up to 50 000 attachment/detachment cycles, which makes CNFs a promising material for long term applications, such as climbing robots.

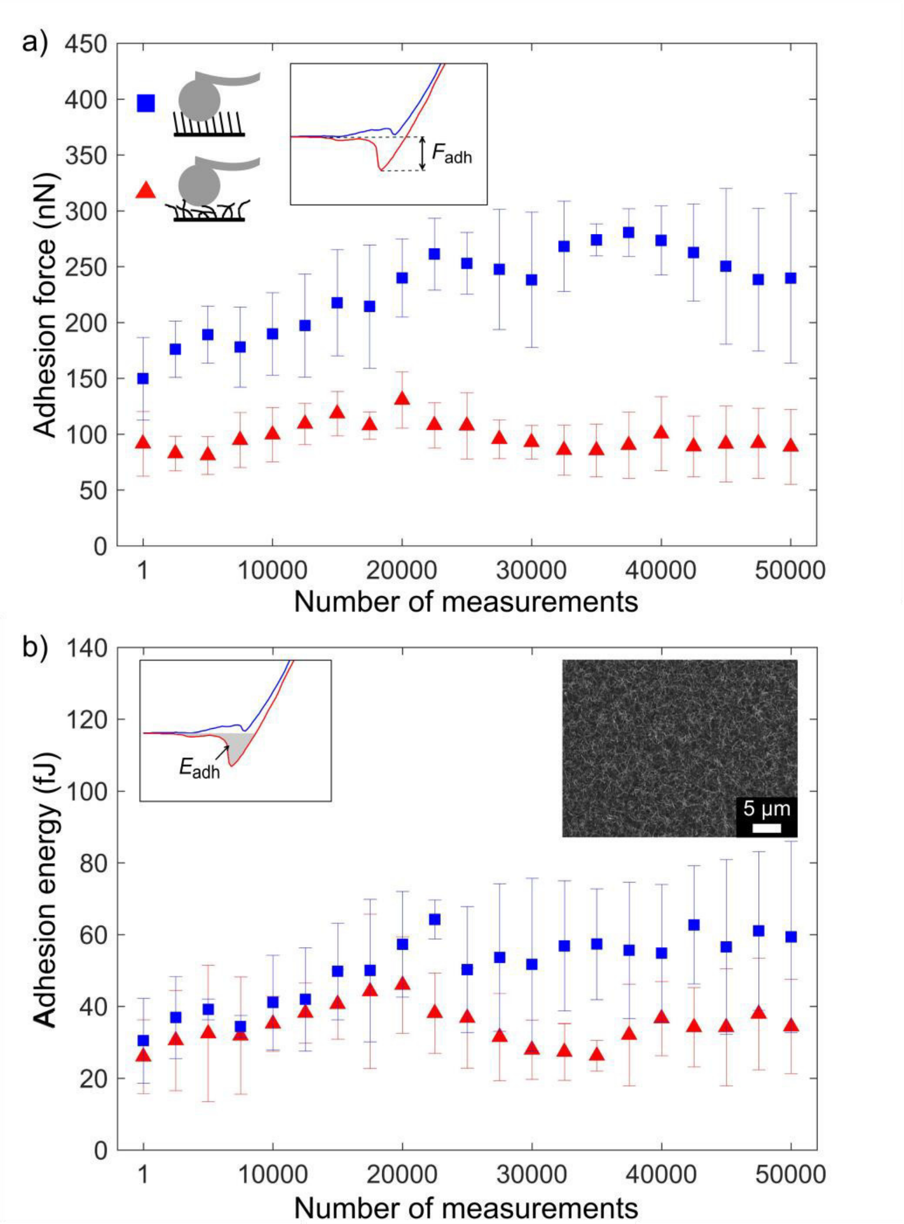

Figure 4.16: Endurance adhesion measurements conducted with an AFM with 50 000 cycles. a) The adhesion force and b) the adhesion energy are represented for arrays with aligned CNFs (blue squares) and randomly oriented CNFs (red triangles). The AFM based adhesion measurement were performed with a 20 µm silica sphere on an AFM cantilever by using a ramp rate of 1 Hz and a constant preload force of 2 µN. Both CNF arrays show adhesion properties after 50 000 measurements in a suitable range for dry adhesives. A SEM image of the array with random CNFs under test is shown in the insert after conducting 50 000 measurements. No visible damage of the CNF array was observed.

To investigate the development of AFM force distance diagrams over time, two endurance runs with 100 000 adhesion measurements (Figure 4.17) were conducted with a) CNF arrays of aligned CNFs and b) CNF arrays with randomly oriented CNFs. The diagrams include force-distance curves for the first measurement (cyan line), after 25 000 measurements (blue line), after 50 000 measurements (green line), after 75 000 measurements (orange line) and for the last measurement at 100 000 (red line).

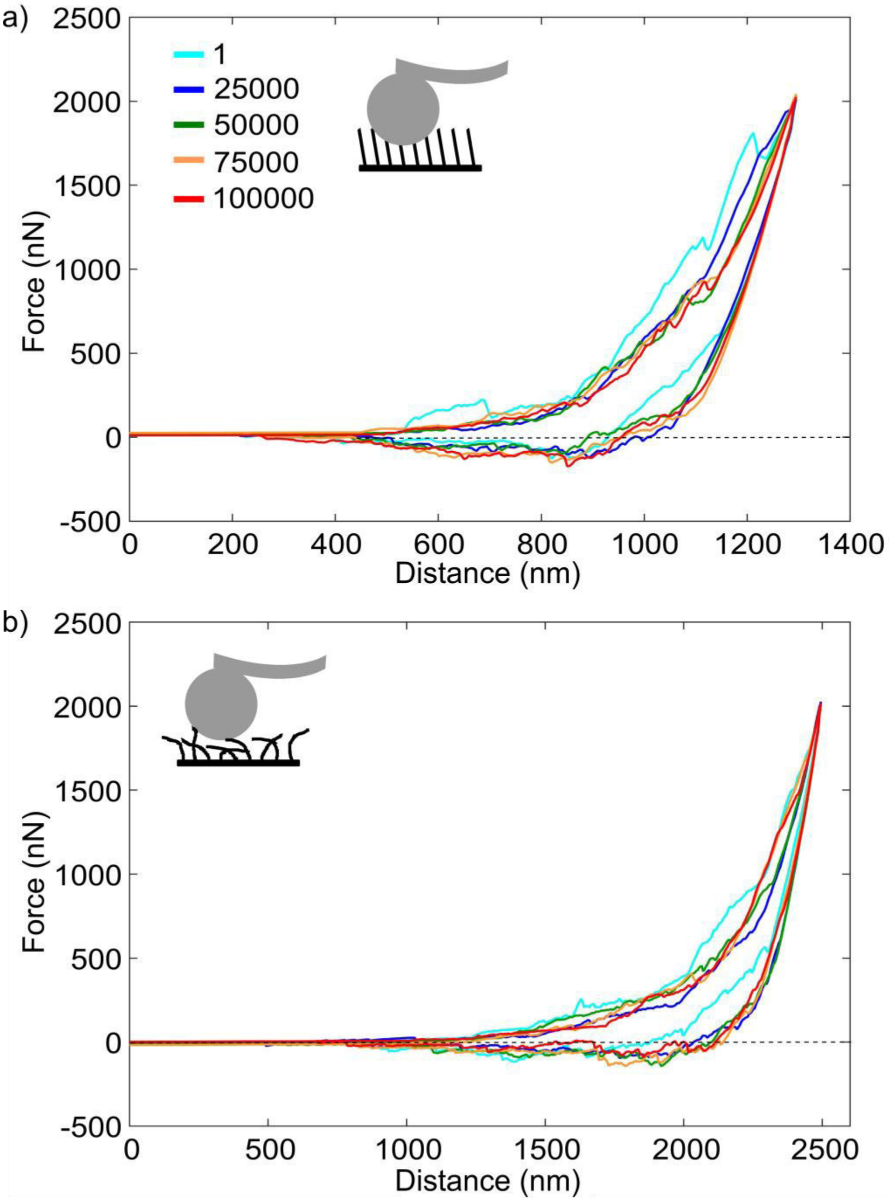

Figure 4.17: Development of AFM force distance diagrams during an endurance run with 100 000 adhesion measurements for a) aligned CNFs arrays and b) randomly aligned CNFs arrays. The diagrams include force-distance curves for the first measurement (cyan line), after 25 000 measurements (blue line), after 50 000 measurements (green line), after 75 000 measurements (orange line) and for the last measurement at 100 000 (red line). The adhesion measurements were conducted with a 20 µm silica sphere on an AFM cantilever with a constant preload force during the whole measurements of 2 µN and a measurement frequency of 1 Hz, resulting in a total time for 100 000 measurements of nearly 28 h. The force distance curves change only marginal during the whole endurance measurement.

The adhesion measurements were conducted with a 20 µm silica sphere on an AFM cantilever with a constant preload force during the whole measurements of 2 µN and a measurement frequency of 1 Hz, resulting in a total time for 100 000 measurements of nearly 28 h. Both force distance curves change only marginal over time. However, small changes in the force distance curves over time can be explained by changing environmental conditions, such as temperature and humidity, over the 28 h experiment. Additionally, small uncertainties in the AFM based measurement can slightly vary the force distance curves. In general, the used AFM based endurance adhesion measurement principle is very precise with only marginal changes over 28 h with 100 000 attachment/detachment cycles.

A shortened version of this Chapter on the flame synthesis CNF growth as dry adhesives was published as the article [39] *"Dry adhesives from carbon nanofibers grown in an open ethanol flame", by Christian Lutz, Julia Syurik, C. N. Shyam Kumar, Christian Kübel, Michael Bruns and Hendrik Hölscher, Beilstein Journal of Nanotechnology, 8, 2719-2728 (2017).*

5 Controlled growth of lambda shaped CNFs with flame synthesis

Nature developed hierarchical structures in different ways, such as branches of trees and plants. As introduced in Chapter 1.1, geckos exhibit hierarchical nanostructures at the end part of their feet, which are responsible for their ability to adhere. The production of artificial hierarchical nanostructures is a very promising approach for mimicking the adhesion of a gecko. CNTs and CNFs are due to their size and mechanical properties the material of choice for this approach. Several research groups reported splitted or hierarchical CNT or CNF structures. The first branched CNTs revealing L-, Y- and T-branches go back to the work of Zhou and Seraphin [185]. Moreover, branched CNTs with more than two branches were obtained by pyrolysis by Wei *et al.* [50]. Tire pyrolysis oil in CVD was used to grow CNTs with Y-branches [186]. A gas mixture of ferrocene, xylene and a Ti-containing gas was used by Gothard *et al.* [187] to grow Y-shaped CNTs in CVD. The expose of MWCNTs to heat with a subsequent sonication process lead to splitted MWCNTs [188]. Moreover, SWCNTs with Y-shapes were reported several times [47], [189], [190]. Y-shaped SWCNTs are very promising for potential electrical applications such as novel kinds of a nano-transistors based on their special conductivity behavior (metallic or semiconducting) as described in Chapter 2.1.1. MWCNTs and SWCNTs are due to their size not easy to investigate. However, CNFs are much bigger and ideal investigation objects to understand the growth mechanism behind Y-shaped CNTs, which is not completely understood up to now. Once the mechanism behind the Y-shapes is understood, it might be transferred to smaller structures such as SWCNTs. In this chapter, the growth of a novel kind of CNF is introduced and the structures are rigorously investigated. The novel CNFs were named lambda-shaped CNFs (ΛCNFs or λCNFs, independence of their geometry) due to their similarity to the Greek letter lambda.

5.1 Substrate fabrication

A substrate with copper micro-bars on a silicon substrate (Figure 5.1) was designed by Julia Syurik and fabricated by the IMT clean room team as the support layer for the growth of lambda shaped CNFs. For that, a silicon wafer with 1 µm SiO_2 was covered with 7 nm Cr and 50 nm Au. A positive photoresist (AZ 4533, Microchemicals GmbH) was coated on the substrate, before a UV-Lithography process with a mask containing openings in the shape of micro-bars was used for illuminating of the resist. Micro-bar cavities were achieved in the photoresist after development. An electroplating process was used to fill the cavities with copper. Finally, the resist was stripped and the Au layer was etched, to achieve a substrate with copper micro-bars (Figure 5.2). The produced copper micro-bars have widths of 14 µm and heights of 3 µm. The period between the micro-bars is 60 µm.

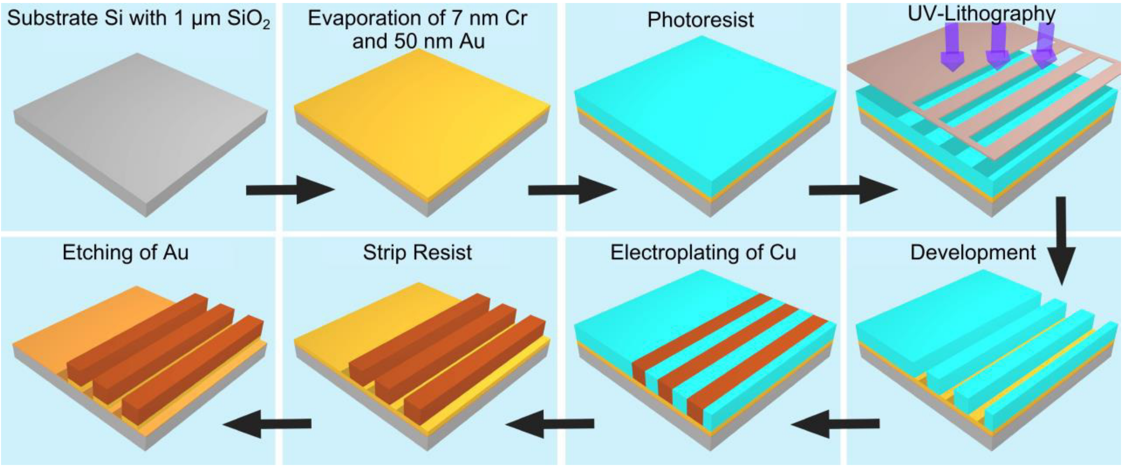

Figure 5.1: Fabrication of the substrate for the growth of lambda shaped CNFs. The base material consists of a silicon wafer with 1 µm SiO_2 on the top. Two metal layers were evaporated over the SiO_2, with 7 nm Cr and 50 nm Au. A positive photoresist (AZ 4533) was coated on the substrate, before a UV-lithography process with a mask containing micro-bars was used for structuring. After development of the resist, cavities were achieved in the photoresist. An electroplating process was used to fill the cavities with copper. Finally, the resist was striped and the Au layer etched to achieve a substrate with copper micro-bars.

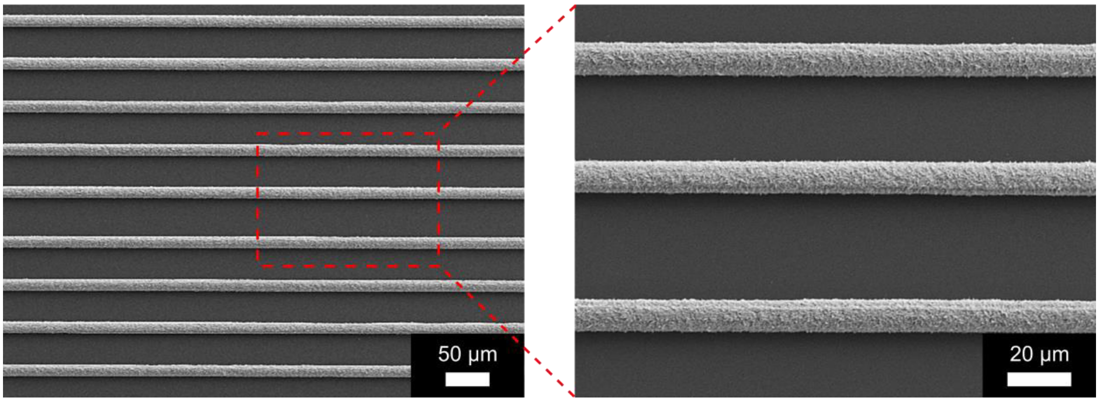

Figure 5.2: Fabricated substrate made by copper bars acting as a support layer for the growth of lambda shaped CNFs. The produced copper micro-bars have widths of 14 µm and heights of 3 µm. The period between the bars is 60 µm.

5.2 Construction of a machine for lambda shaped CNF growth

As described in Chapter 4, CNFs can be successfully grown in an open ethanol flame. However, it is a challenge to achieve a stable flame. Flicker of the flame can expose the sample for a short time to atmosphere where the nickel catalysts might oxidize and hence stop CNF growth. Therefore, a machine offering a constant flame with additional facilities like flame extinguishing was built up to conduct the experiments under controlled conditions. The machine was designed with CAD software (Figure 5.3 a) and built up after this design (Figure 5.3 b) by Tobias Loritz during his Master's thesis [191]. An ethanol burner was placed in the center of the machine. The wick size of the burner is 2 x 12 mm² with an ethanol combustion rate of 0.4 mL/min. A closed system around the burner keeps the flame as stable as possible. To achieve a constant air flow and hence a stable vertically aligned flame, the machine is equipped with a base plate with tiny holes for air inlet and a big hole in the ceiling for air outlet. A nitrogen pipe with holes is placed under the ethanol flame to extinguish the flame and stop the experiment (Figure 5.3 c). The sample is placed vertically directly in the ethanol flame and fixed with an aluminum oxide holder. During growth, a magnetic field can be applied. The magnet is protected from the ethanol flame with heat protection plates made from aluminum oxide. The magnet is additionally water cooled to prevent it from heating up and losing its performance. The possibility to apply the magnet offers options for further experiments, such as alignment of the CNFs with an external magnetic field during growth [39], [120]. Figure 5.3 d) shows the ethanol flame with the typical for ethanol combustion blue color.

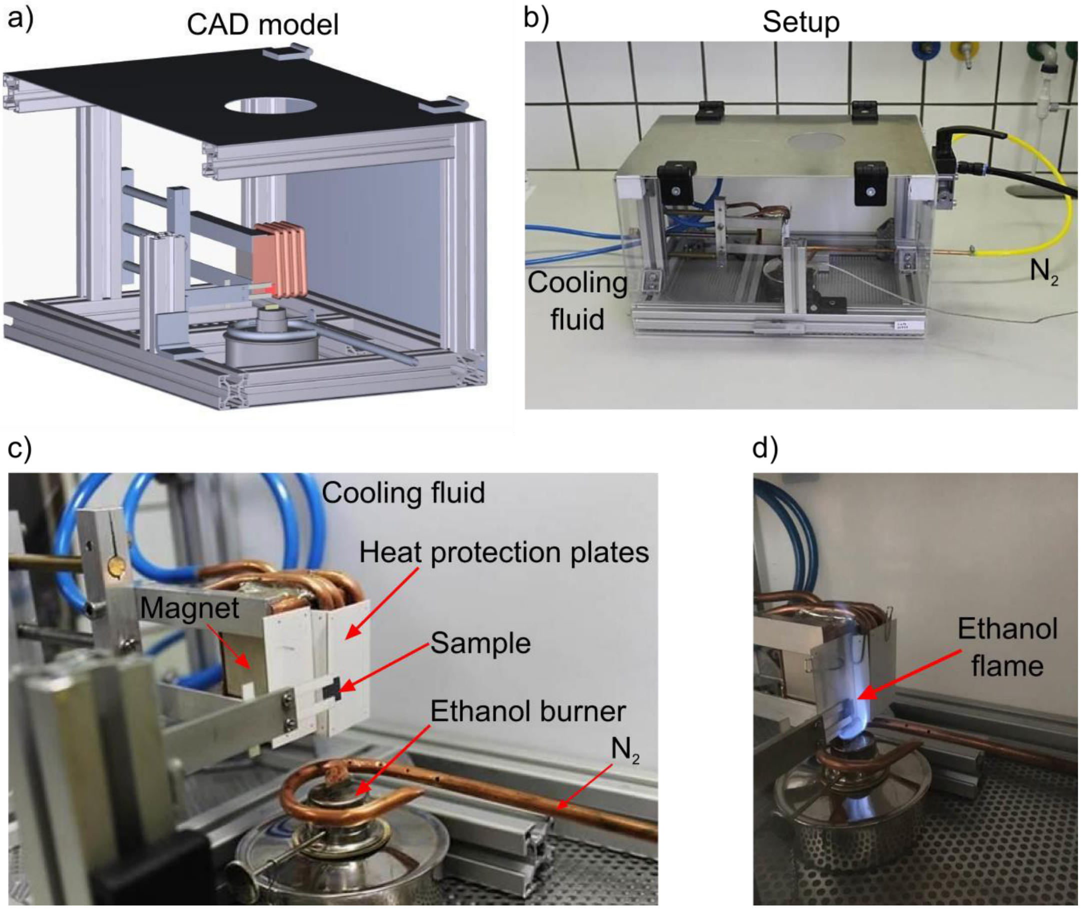

Figure 5.3: Self-built machine to grow lambda shape CNFs. a) A CAD model of the machine and b) the built-up machine. The machine consists of an open ethanol flame produced by an ethanol burner placed in the center and a closed system around the burner to keep the flame as stable as possible. To achieve a constant air flow and subsequently a stable vertically aligned flame, the machine is equipped with a big hole in the ceiling and a base plate with tiny holes for the air inlet and outlet. c) A nitrogen pipe with holes is placed under the ethanol flame to extinguish the flame and stop the experiment. The sample is placed vertically directly in the ethanol flame fixated with an aluminum oxide holder. During growth, a magnet can be applied. The magnet is protected from the ethanol flame with heat protection plates made from aluminum oxide and water cooling to prevent the magnet from heating up and losing its performance. d) The ethanol flame with the typical blue color.

5.3 Growth of lambda shaped CNFs

The first lambda shaped CNFs were achieved in an experiment using the fabricated substrate from Chapter 5.1. A droplet of $NiCl_2*6H_2O$ solved in ethanol (20 mg/mL) was placed on the substrate and dried in air. CNF growth was performed in the machine with the ethanol flame (see Chapter 5.2) for 10 minutes. This procedure resulted in the growth of a novel kind of CNF, which I named lambda shaped CNF. The fabricated substrate has a Cr surface in addition to the copper bars for the deposition of the $NiCl_2$ catalysts. However, lambda shaped CNFs were also obtained on Cu, Au and SiO_2 surfaces, which make a Cr surface obsolete. A magnet can be applied to the growth setup. However, the magnet is not necessary to grow lambda shaped CNFs. Experiments without a magnet also revealed growth of lambda shaped CNFs. Nevertheless, after my investigations a weak magnetic field influenced the CNF growth with flame synthesis in a positive way (see Chapter 4.3.4).

Several lambda shaped CNFs were found over the whole substrate. Figure 5.4 a) shows one of the achieved lambda shaped CNFs. The two CNFs of the λCNF are named branch 1 and branch 2 and are connected with the substrate. The third CNF (branch 3) with the catalytic particle at the top is free standing on the two other branches. For a geometry analysis, 32 λCNFs were investigated for their diameters (Figure 5.4 b) and angles between the branches (Figure 5.4 c). The diameters range from 290 nm to 570 nm, with the diameters: $d_1 = 413.1$ nm ± 81.6 nm, $d_2 = 409.4$ nm ± 72.5 nm and $d_3 = 437.8$ nm ± 68.9 nm, where indices 1-3 correspond to the branch number. The angles are defined between the three branches to build a full cycle of 360° ($\alpha_{12} + \alpha_{13} + \alpha_{23} = 360°$), with the average angles: $\alpha_{12} = 101.6° \pm 20.0°$, $\alpha_{13} = 128.4° \pm 18.4°$ and $\alpha_{23} = 128.4° \pm 18.9°$.

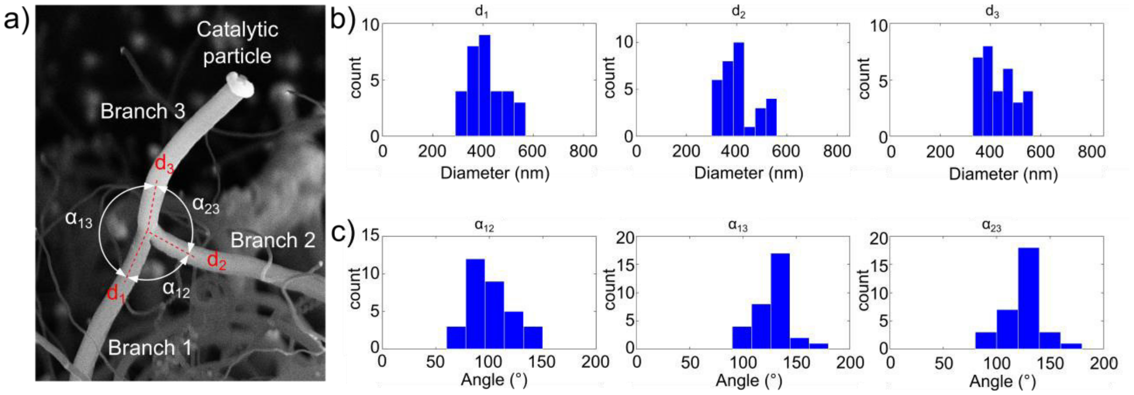

Figure 5.4: Geometry analysis of λCNFs. a) The λCNFs consist of three branches. Branch 1 and branch 2 are connected with the substrate, whereas branch 3 is free standing on the two others with the catalytic particle at the top. For the analysis, 32 λCNFs were analyzed for their diameters and angles between the branches. b) The diameters range from 290 nm to 570 nm, with the average diameters: $d_1 = 413.1$ nm, $d_2 = 409.4$ nm and $d_3 = 437.8$ nm. c) The angles are defined between the three branches to build a full cycle of 360°, with the average angles: $\alpha_{12} = 101.6°$, $\alpha_{13} = 128.4°$ and $\alpha_{23} = 128.4°$.

5.4 Controlled growth of lambda shaped CNFs from catalyst deposited by dip-pen nanolithography

As explained in Chapter 5.3, lambda shaped CNFs can be grown in an uncontrolled way by the deposition of a big ethanol droplet (in the µL range) containing the Ni-catalysts for the lambda shaped CNF growth on the substrate in the presence of copper. However, AFM offers a possibility for the controlled deposition and downscaling of such droplets. Dip-pen nanolithography (DPN) and microchannel cantilever spotting (µCS) are two common possibilities for the controlled deposition of micro- and nanodroplets (Figure 5.5). DPN uses a tip of an AFM cantilever dipped in a droplet to collect the fluid followed by writing points with an exponential decrease of the droplet size [192]. Moreover, µCS uses an AFM cantilever needle with a reservoir for fluids allowing the controlled deposition of droplets, all with the same size, preconditioned the reservoir is properly filled [193]. DPN and µCS were performed with the support of Michael Hirtz and Uwe Bog at INT.

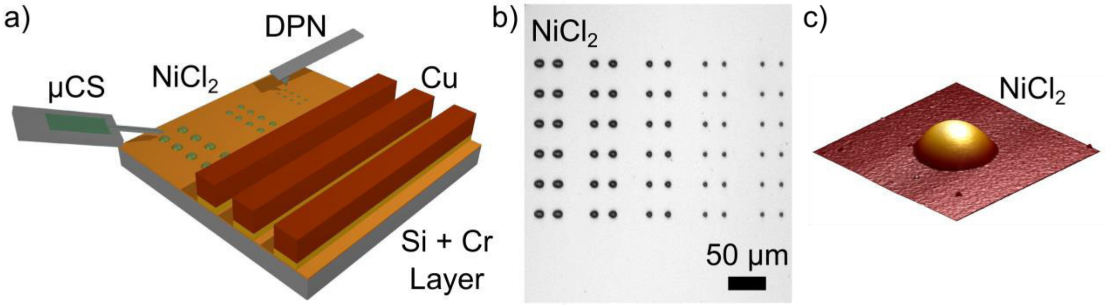

Figure 5.5: DPN and µCS deposition of $NiCl_2$ catalysts solved in ethanol. a) Schematic of the DPN and µCS deposition on the substrate. b) Optical image from the deposited $NiCl_2$ catalysts ranging from 15 µm to 3 µm. c) AFM topography scan of one deposited $NiCl_2$ catalyst.

5.4.1 Ordered arrays with multiple lambda shaped CNFs

Ordered arrays were written with µCS with $NiCl_2$ solved in ethanol (2 mg/mL) and diluted with glycerol (1:10). Figure 5.6 shows the µCS writing process with different dwell times and the corresponding CNF outcome after flame synthesis. The $NiCl_2$ droplet size can be increased by increasing the dwell time. A dwell time of 1 s leads to smaller droplets than a dwell time of 2 s. After flame synthesis of the samples, ordered arrays with CNFs grow on the same position on the substrate where the $NiCl_2$ catalysts were deposited.

Figure 5.7 a) show another example of µCS writing with the controlled growth of lambda shaped CNFs from ordered arrays building INT/IMT logos. The distance between the deposited spots was 20 µm using a dwell time of 0.5 s with a relative humidity of 40 %. The growth was performed using the self-built machine with the ethanol flame from Chapter 5.2 with a growth time of 10 min. A human hair (diameter ~80 µm) was placed beside the arrays with lambda shaped CNFs to illustrate their size during gradually zoom in.

A Raman spectroscopy was conducted with the help of Sharali Malik (Figure 5.7 b). The measurement shows the D-band by 1356 cm^{-1} and the G-band by 1587 cm^{-1}, indicating that the lambda shaped CNFs are made of carbon. Additionally to the Raman investigation, Michael Bruns performed a XPS measurement. Figure 5.7 c) shows the XPS measurements with the

C1s XP spectrum. The experimental data are represented by the red cycles with the envelope line of the experimental data (red solid line). The lambda shaped CNFs mainly consists of graphite (sp^2) indicated by the blue solid line with a peak at 284.4 eV binding energy. The lower second component represented by the blue dashed line at a binding energy of 285.0 eV detect adventitious carbon.

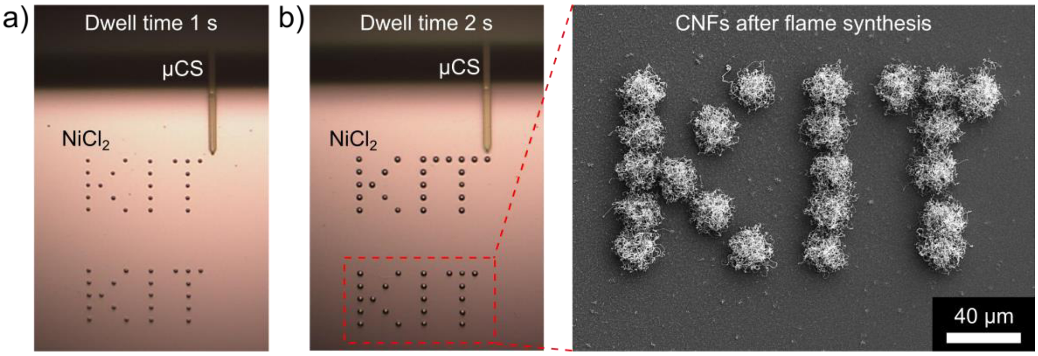

Figure 5.6: Ordered arrays of CNFs arranged as KIT logos written with µCS with $NiCl_2$ solved in ethanol (2 mg/mL). The $NiCl_2$ droplet size can be increased by increasing the dwell time. a) A dwell time of 1 s leads to comparable small droplets compared with b) where a dwell time of 2 s was used. After flame synthesis of the samples, ordered arrays with CNFs grow at the same position on the substrate where the $NiCl_2$ catalysts were deposited.

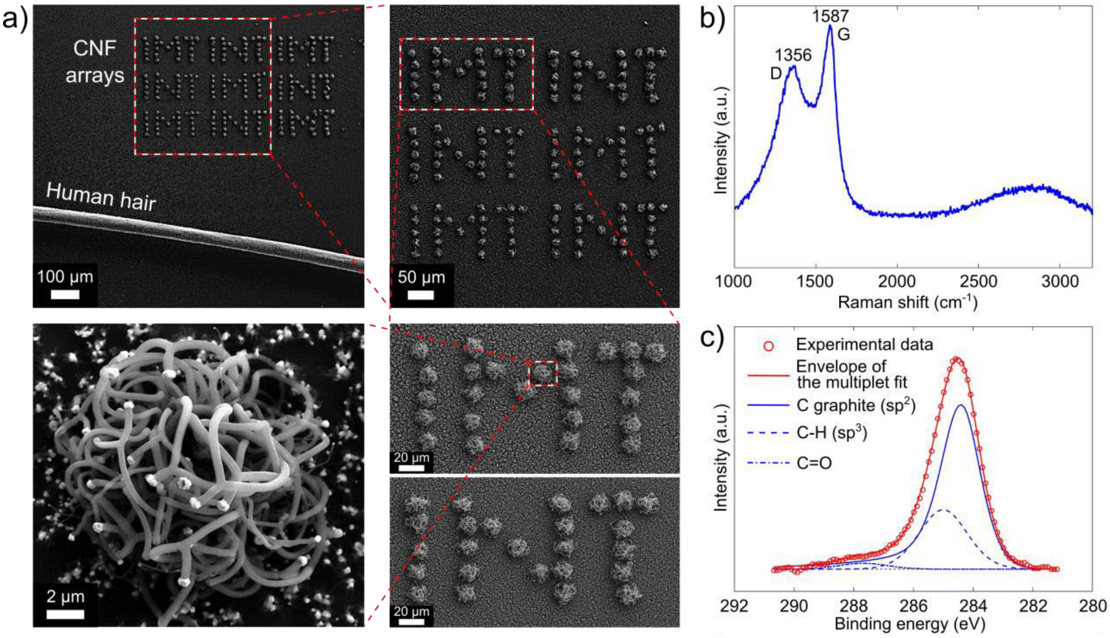

Figure 5.7: Lambda shaped CNF growth from $NiCl_2$ catalysts deposited by µCS. a) Structured writing of catalysts with µCS leads to the controlled growth of lambda shaped CNF arrays on defined positions on the substrate. To imagine the size of the CNFs, a human hair (diameter ~80 µm) was placed beside arrays with lambda shaped CNFs. The last image of the gradually zoom in shows a bundle of lambda CNFs. b) Raman spectra with the characteristic D and G bands for carbon materials such as CNFs. c) A C1s XP spectrum obtained from lambda shaped CNFs. The experimental data are represented by the red cycles with the envelope line of the experimental data (red solid line). The lambda shaped CNFs mainly consists of graphite (sp^2) indicated by the blue solid line with a peak at 284.4 eV binding energy.

Energy dispersive X-ray spectroscopy (EDX) measurements were performed by Sharali Malik on different positions of the λCNFs, to investigate their elementary composition. A Zeiss Leo 1530 SEM with an EDX detector (Oxford X-MaxN 50) was used. Table 5.1 shows the EDX measurements on different parts of λCNFs. The body and junction of the λCNFs have nearly the same material compositions. The main part is carbon with 64 – 65 wt % and some residuals with silicon and copper. A certain amount of oxygen (~20 wt %) assumable arise during exposure of the λCNFs to ambient conditions after growth. The catalytic center consist of ~52 wt % carbon, which fits with the literature, where carbon is solved in the catalyst [73]. Beside some oxygen and silicon residuals, the catalytic centers consist of the metals of an alloy made by nickel/copper (1:20). Therefore, copper assumable influence the growth of lambda shaped CNFs in a strong way.

Table 5.1: EDX measurement on different parts of λCNFs. The error bars in the table represent the confidence limits obtained from the EDX software.

Part of λCNFs	Carbon (wt %)	Oxygen (wt %)	Silicon (wt %)	Copper (wt %)	Nickel (wt %)
Body	64.25 ± 0.14	20.28 ± 0.14	15.22 ± 0.06	0.24 ± 0.02	-
Junction	65.30 ± 0.14	20.05 ± 0.14	14.38 ± 0.05	0.27 ± 0.02	-
Catalyst	52.18 ± 0.15	29.72 ± 0.14	9.71 ± 0.04	7.99 ± 0.06	0.39 ± 0.02

5.4.2 Downscaling for the controlled growth of single lambda shaped CNFs

To discover the secret behind lambda shaped CNFs, it would be desirable to switch from lambda shaped CNF bundles as shown in Chapter 5.4.1 to single lambda shaped CNFs. DPN offers the controlled downscaling of the $NiCl_2$ catalysts until a critical catalytic volume arise where only one separated lambda shaped CNF grows. Therefore, µCS was used for the deposition of $NiCl_2$ droplets acting as a reservoir for the following DPN writing cycles. Figure 5.8 a) shows the first five DPN writing cycles and Figure 5.8 b) shows the DPN writing cycles form six to ten. AFM was used to scan the $NiCl_2$ catalysts deposited by DPN for size determination which was used to calculate the catalytic volume. The AFM topograhy scans revealed a decline in the catalyst size with each cycle. Therefore, the AFM scan field was initially set to 6 x 6 µm² and adjusted to 2 x 2 µm² from DPN cycle six upwards.

The AFM topography measurements contain height information of each position of the scan, as schematically illustrated in Figure 5.9. This allows calculating the volume V of the DPN deposited $NiCl_2$ microdots from the AFM topography scans by using the following Equation based on an integral calculus expressed with sum formulas:

$$V = \sum_{i=1}^{n} \sum_{j=1}^{k} h_{ij} A_{ij}, \tag{5.1}$$

where n and k are the total amount of measuring points of the two lateral scan directions. The single volume on each position is calculated by the height h_{ij} multiplied with the corresponding base area A_{ij}. In the case that the sizes between the measuring points do not change over the scanned area, the base area can be calculated by using the two lateral lengths L_n and L_k of the measurement.

$$A_{ij} = \frac{L_n L_k}{nk} \tag{5.2}$$

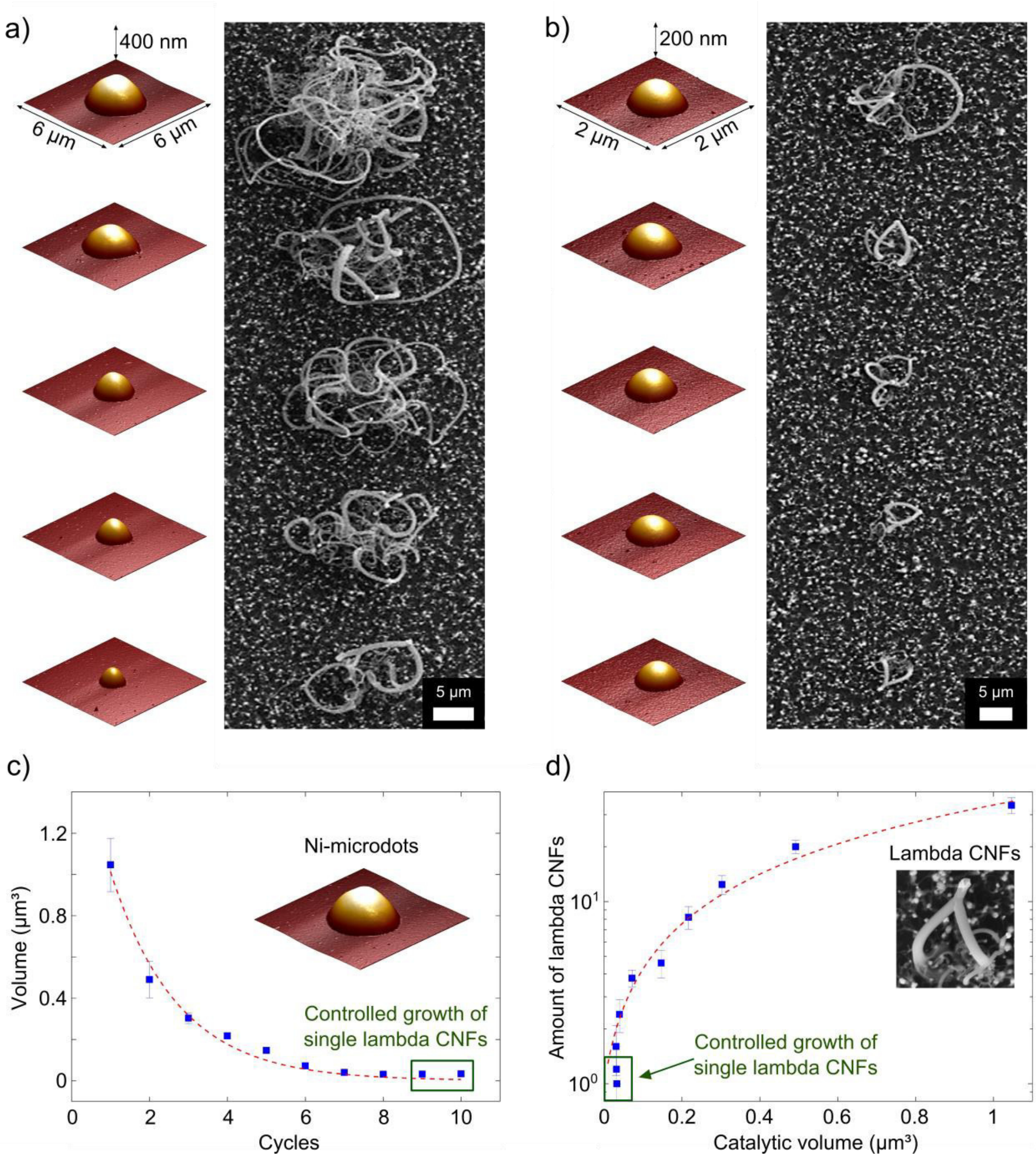

Figure 5.8: DPN based downscaling of the $NiCl_2$ catalysts to grow separated single lambda shaped CNFs. a) The first five cycles of DPN resulting in decreased volumes of the catalysts after each cycle represented by AFM topography scans of the catalysts on the left side and the corresponding CNF growth from the catalysts on the right side. b) The DPN cycles from six to ten. Single lambda shaped CNFs were achieved after 9 DPN cycles. c) The catalytic volume over the DPN cycles follows an exponential decline, revealing an average critical catalytic volume of ~0.0336 µm³ to grow one lambda shaped CNF. d) The amount of lambda shaped CNFs over the catalytic volume.

In the case of a square scan in the lateral direction $(L = L_n = L_k)$ and $(n = k)$ leading to the following simplification of the Equation to calculate the volume from the AFM topography scans.

$$V = \frac{L^2}{n^2}\sum_{i=1}^{n}\sum_{j=1}^{n} h_{ij} \tag{5.3}$$

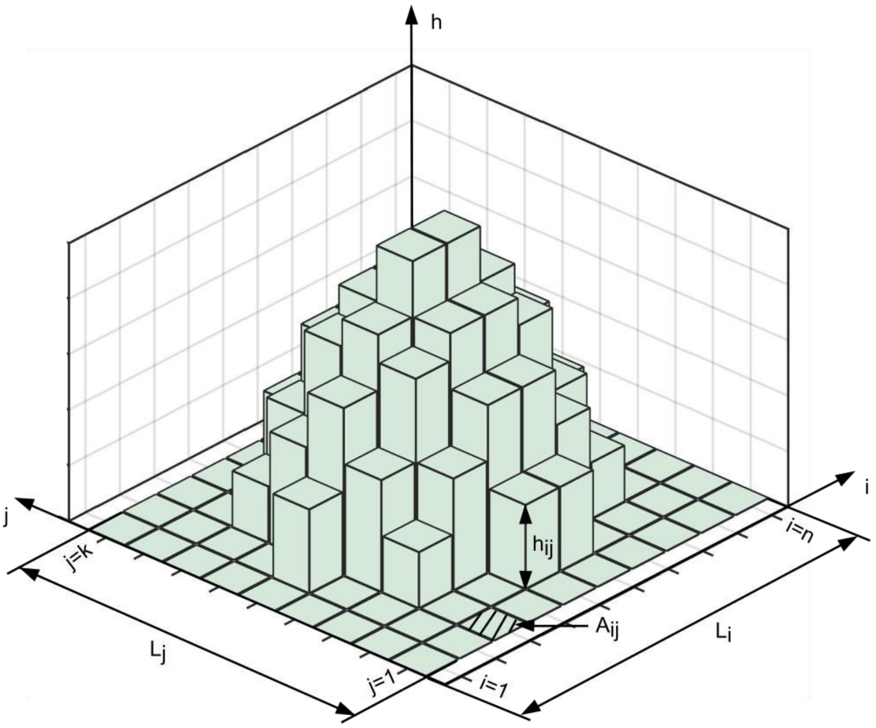

Figure 5.9: Schematic illustration of the data points from an AFM topography scan for the volume calculation. The scan field is defined by the lateral positions L_i and L_j. The pillars represent the heights for each data point. The corresponding area A_{ij} can be calculated from the scan lengths and the samples per line. Multiplying the single areas with the corresponding heights, leading to the volume of a pillar. Adding of all the pillar volumes lead to the total volume.

Figure 5.8 c) shows the calculated catalytic volume using Equation (5.3). The catalytic volume follow an exponential decline: $V_{Ni}(c) = 1.812e^{-0.5816c}$, starting with a catalytic volume of (1.05 ± 0.14) μm^3 (n=5) for the first cycle down to (0.0336 ± 0.0081) μm^3 (n=5) for cycle number ten. This exponential decline in DPN fits with the work of Förste *et al.* [192].

The produced catalytic centers were processed in the ethanol flame for 10 min resulting in lambda shaped CNFs bundles down to the controlled growth of single lambda shaped CNFs. The SEM images from the lambda shaped CNF are placed next to the corresponding catalytic centers in Figure 5.8 a-b). Bundles of lambda shaped CNFs grow from the first DPN writing cycles, whereas separated single lambda shaped CNFs grow from DPN cycle 9 upwards until cycle 13. After DPN cycle 13, no CNF growth was observed assumable due to a too small catalytic volume. The critical volume, where only one lambda shaped CNF grows, was determined to ~0.0336 μm^3 of $NiCl_2$. Figure 5.8 d) shows the counted amount of lambda shaped CNFs from the SEM images over the catalytic volume. The controlled growth of single lambda shaped CNFs starting from DPN cycle 9 is marked with the green box.

Figure 5.10 shows a compilation of different single lambda shaped CNFs grown on defined positions of the substrate by DPN deposition of $NiCl_2$. The shape of the achieved lambda shaped CNFs can be controlled over the growth time. Growth times between 5 – 10 min resulting in ΛCNFs (Figure 5.10 a), whereas increasing the growth time above 10 min resulting in λCNFs (Figure 5.10 b). Figure 5.10 c) shows twisted lambda shaped CNFs, with twisted feet CNFs and not twisted head CNFs with the catalytic centers at the top, achieved in a channel structure with higher flame velocities.

HRTEM measurements were conducted with the help of C. N. Shyam Kumar and Christian Kübel to investigate the interior of some typical λCNFs (Figure 5.10 d). The HRTEM images revealed partially dens black parts, assumable from carbon located in the center of the junctions. A focused ion beam (FIB) from FEI Helios Nanolab 650 with an current of 40-80 pA and an acceleration voltage of 30 kV was used with the help of Christian Greiner to cut twisted and not twisted lambda shaped CNFs (Figure 5.10 e). The ΛCNF revealed no stress after cutting, whereas the twisted lambda shaped CNF changed their geometrical arrangement after cutting which might originate from stored tension in the structures.

5.5 Theory for the growth of lambda shaped CNFs

Two growth theories were developed to explain how lambda shaped CNFs can grow. In the first theory, two CNFs grow from two different nickel catalysts located close to each other. After a short growth time the two CNFs growing with the nickel catalysts together. This can be induced by the thermal fluctuation from the ethanol flame. Although, CNTs and CNFs are stiff at room temperature, they are ductile at high temperatures [194], which assumably allows them to oscillate in the ethanol flame. Once the two nickel catalysts are touching each other and building a ΛCNF, they probably melt together. However, the temperature in the ethanol flame of 750 °C is lower than the melting point of bulk nickel (1453 °C), the catalysts can melt together due to a reduced melting point of nanoparticles as describes in Chapter 2.1.3. The newly formed catalytic center at the top grows a new CNF upwards resulting in a λCNF.

However, there are three main findings speaking against this theory. At first, the entire lambda shaped CNFs have nearly the same diameter and lengths of the feet CNT. Additionally, in over 50 experiments with different growth times the state shortly before two CNFs touching each other was never observed. Especially in the lambda shaped CNF bundles (Figure 5.7 a), nearly every CNF is a lambda shaped CNF, which means that every CNF have to find a suitable partner CNF.

Therefore, a second growth theory for lambda shaped CNFs was developed (Figure 5.11 a). In this theory two CNFs grow from one nickel catalyst in opposite directions. The two CNFs adhering with their end parts to the substrate. The still growing CNFs induced by the nickel catalyst building an arc (ΛCNF). The two CNFs of the ΛCNF touching each other under the nickel catalyst, giving the catalyst only the possibility to grow upwards with another CNF resulting in a λCNF. Figure 5.11 b) shows two SEM images from an early growth state of the lambda shaped CNFs, with the catalytic center (bright parts) and two CNFs growing from it in opposite direction, supporting the growth theory from Figure 5.11 a).

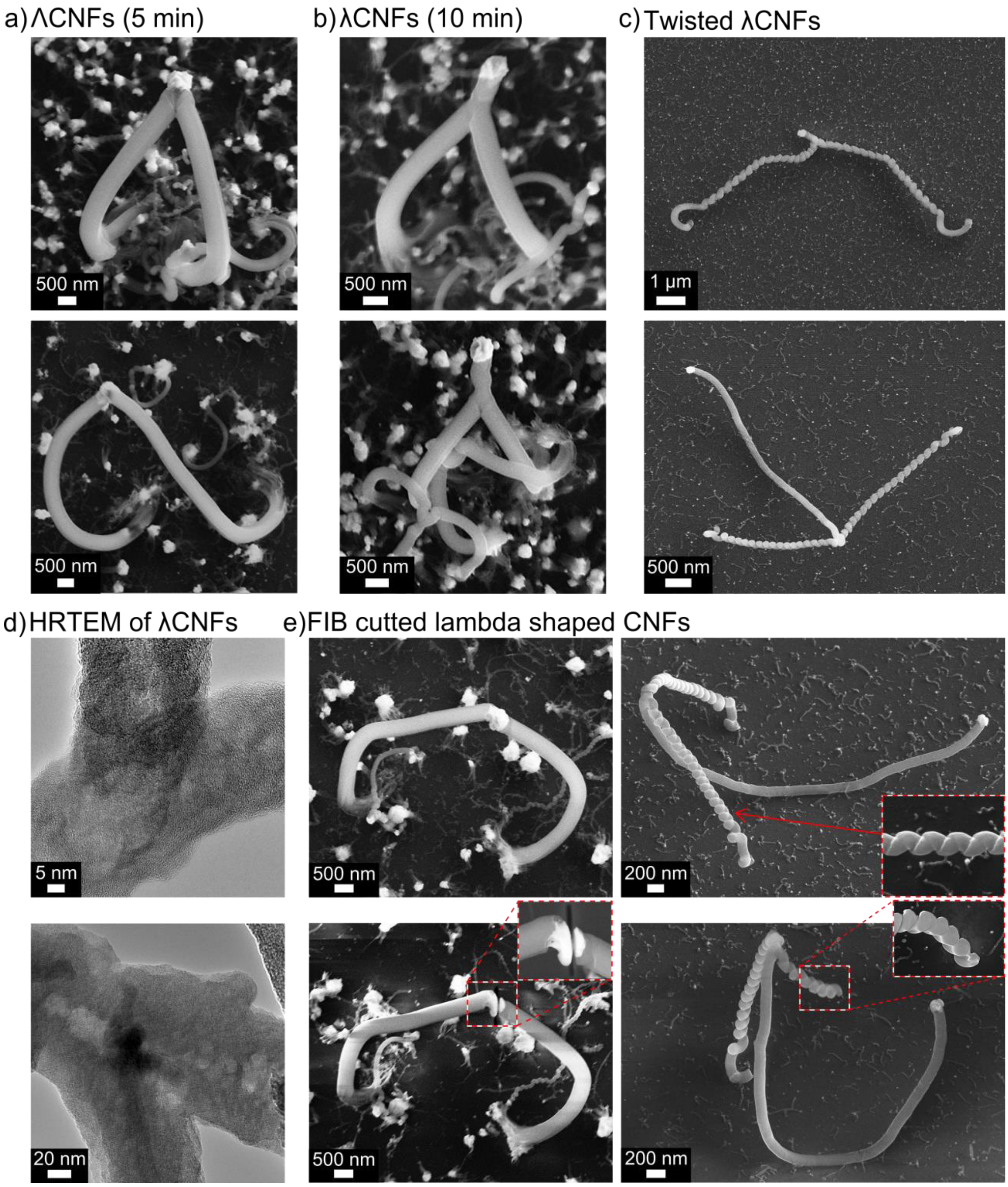

Figure 5.10: Compilation of different separated lambda shaped CNFs. SEM images of a) ΛCNFs and b) λCNFs. c) Higher flame velocities achieved in a channel lead to twisted lambda shaped CNFs, with twisted feet CNFs and the not twisted head CNFs with the catalytic centers at the top. d) HRTEM images of lambda CNFs revealing partially a dense black part (probably carbon) in the middle of the junctions. e) FIB cut of twisted and not twisted lambda shaped CNFs. The ΛCNF revealing no stress after cutting whereas the twisted λCNFs changed their geometrical arrangement after cutting which might originate from stored tension in the structures.

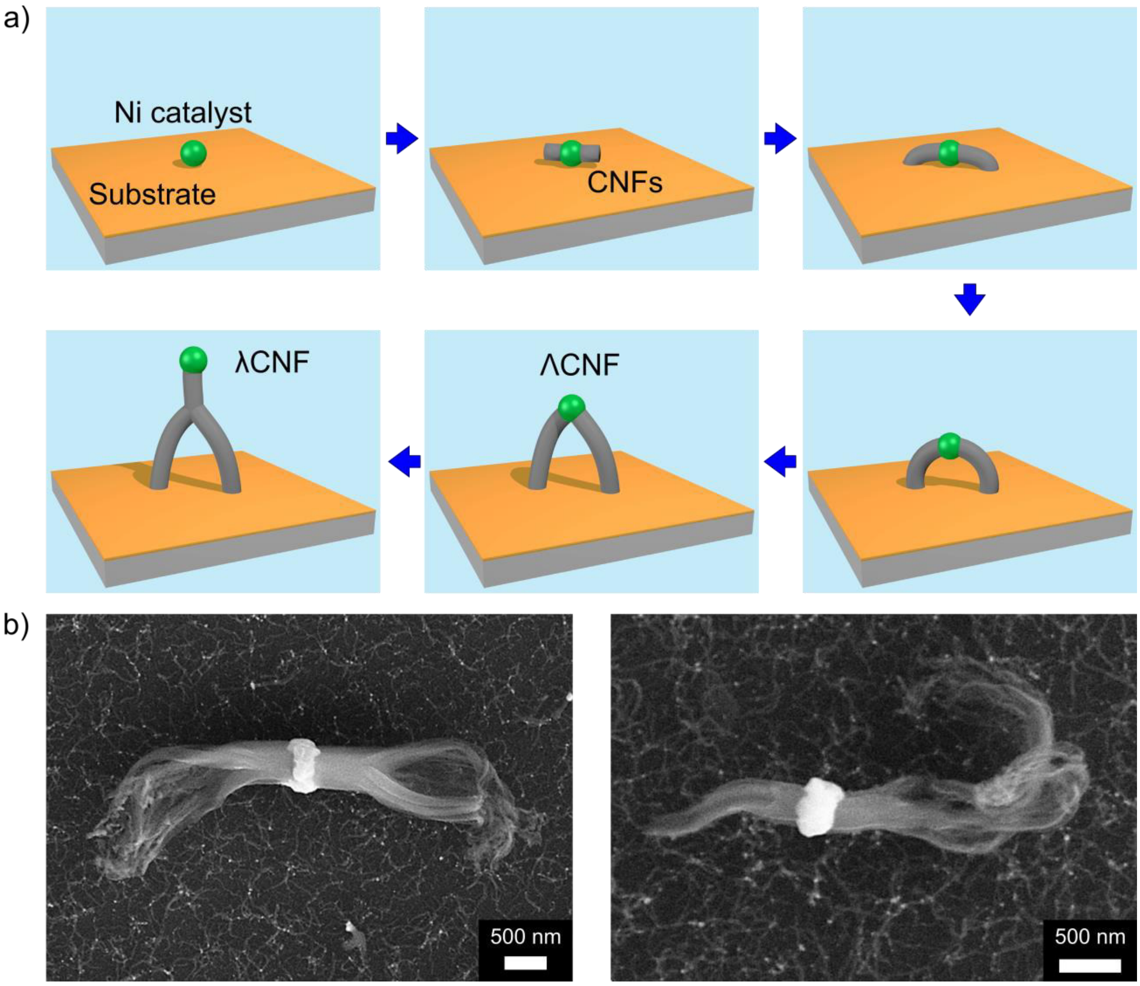

Figure 5.11: A possible theory for the growth of a lambda shaped CNFs. a) A nickel catalyst is deposited on a substrate and exposed to an ethanol flame. Two CNFs are growing from the nickel catalyst in opposite directions. The end parts of the two CNFs are adhering to the substrate and the CNF growth continue induced from the nickel catalyst resulting in an arc (ΛCNF). The two CNFs are touching each other under the nickel catalyst. The nickel catalyst has only the possibility to grow upwards with another CNF resulting in a λCNF. b) Two SEM images from an early growth state of lambda shaped CNFs supporting the theory in a).

5.6 Twisted lambda shaped CNFs

A special kind of lambda shaped CNF, the so named twisted λCNF (Figure 5.10 c) was observed, using higher flame velocities produced in a channel due to the dynamic pressure at the inlet (Figure 5.12 a). Due to a higher force from the ethanol flame to the ductile λCNF, the head CNF is assumable rotating through its feet and twisting them. A twisted λCNF have two twisted CNF feet and a not twisted CNF head with the catalytic center at the end. The diameters of the twisted λCNFs range from 100 nm to 250 nm, which is approximately only 50 % of the not twisted λCNFs. Measuring 50 twisted lambda shaped CNFs using the notation from Figure 5.4 a), the diameters are: d_1 = 152.2 nm ± 32.7 nm, d_2 = 166.3 nm ± 39.7 nm and d_3 = 171.0 nm ± 42.1 nm. The lengths of the three CNFs in a twisted λCNF are much larger than in case of not twisted λCNF. The distance between the two feet connected with the ground can achieve up to 10 µm and the head CNF have lengths up to 5 µm. The lengths are: $l_1 = 4.2$ µm ± 2.3 µm, $l_2 = 2.8$ µm ± 1.2 µm and $l_3 = 2.8$ µm ± 1.2 µm. The higher growth rate can be explained due to a higher flame velocity delivering more carbon from the ethanol to the CNFs and enhance their growth.

The fact that the head CNF is not twisted speaks for the presented growth theory. Moreover, if the head CNF is moving through its feet CNFs, both feet CNFs should have the equal amount of twists, which was observed in most but not all cases. The amounts of twists are: $t_1 = 0.0 \pm 0.0$, $t_2 = 14.0 \pm 7.5$ and $t_3 = 14.1 \pm 8.3$. Figure 5.10 c) shows two twisted lambda CNFs with 17 twists for both feet (for the λCNF on the top) and 16 twists for both feet (for the λCNF on the bottom). However, some head CNFs appear so large that they cannot rotate through their feet CNFs. In this case, it might be possible that the head CNF is growing during the rotation as long as they cannot longer rotate due to an increased length. Then the head CNF is still growing on the ground without rotating through its feet CNFs. Figure 5.12 b) shows a twisted lambda shaped CNF from the top view and a 52° tilted view of the same structure revealing that the long head part touching the ground on a certain distance which speaks for this theory.

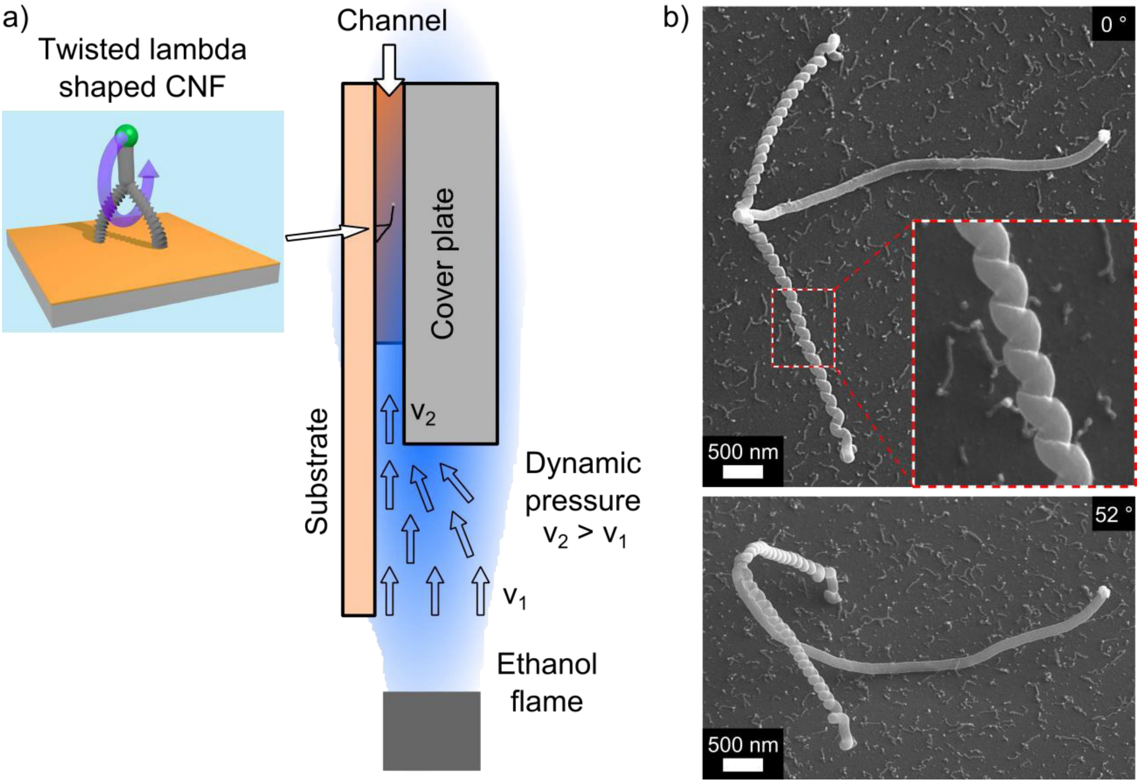

Figure 5.12: Growth of twisted lambda shaped CNFs in a channel structure with increased flame velocity. a) The schematic setup with the channel where twisted lambda shaped CNFs grow between the substrate and a cover plate. The dynamic pressure at the inlet of the channel leading to a higher flame velocity in the channel compared with the flame velocity outside. An increased velocity of the ethanol flame forces the head CNF with the nickel catalyst on the top to rotate through its two feet CNFs resulting in a twisted lambda CNF with two twisted feet and a not twisted head CNF. b) Two SEM images of the same lambda shaped CNF with different views. The top view (0°) is placed at the top with a magnified view of one twisted foot CNF. A 52° tilted view on the bottom revealed that the head CNF part touching the substrate at half length.

A shortened version of the lambda shaped CNFs growth presented in this Chapter is accepted for publication in Small (2019) as the article "Locally controlled growth of single lambda-shaped carbon nanofibers", by Christian Lutz, Uwe Bog, Tobias Loritz, Julia Syurik, Sharali Malik, C. N. Shyam Kumar, Christian Kübel, Michael Bruns, Christian Greiner, Michael Hirtz and Hendrik Hölscher.

6 Conclusion and outlook

In conclusion, the adhesion of CNFs for their use in space technology was investigated and a new process to grow CNFs with an open ethanol flame was developed resulting in the discovery of lambda shaped CNFs.

For the investigation of the adhesion under harsh conditions, such as in space, micro-debris parts of meteorites were mounted on AFM cantilevers and adhesion properties during interacting with CNT surfaces grown in PECVD were investigated. It was observed that the adhesion properties, such as the adhesion force with ~2.5 N/cm², is independent from the temperature in the investigated range from -20 °C to +240 °C. Additionally, the interaction between micro-ice layers created with a Peltier element in an AFM and CNTs mounted to AFM cantilevers was investigated. The measured adhesion force of about 2.3 N/cm² is constant even during thousands of endurance runs. Consequently, CNTs are a perfect material for adhesives working under harsh condition such as in space.

However, CNTs grown with conventional CVD or PECVD processes require a complex infrastructure, a certain amount of process gases and energy to heat an oven and to run control units over a computer. Therefore, an alternative process to grow CNFs in an open ethanol flame was developed. The substrate consists of a part of a Si wafer with a ~50 nm Cu layer. $NiCl_2$ was coated on the substrate acting as a catalyst to grow CNFs. The growth was conducted in an open ethanol flame using a standard ethanol burner offering the heat (~750 °C) and carbon for CNF growth. Due to a growth time of 3 min, only 1.2 mL ethanol is necessary for one experiment, demonstrating the environmental friendly and cost-efficient of the developed process. The produced CNF samples were investigated by AFM for their adhesion properties, revealing an adhesion force of 0.66 N/cm². Additionally, endurance tests demonstrated their long-term stability in 50 000 attachment/detachment cycles.

Rigorous further development of the process led to the invention of novel lambda shaped CNFs, revealing Λ- and λ-shapes. Using AFM based µCS and DPN for $NiCl_2$ deposition it was possible to grow lambda shaped CNFs on locally defined positions on the substrate with the possibility for downscaling to grow single lambda shaped CNFs. Growth of lambda shaped CNFs in a micro-channel with an increased flame velocity led to the discovery of twisted lambda shaped CNFs, revealing two twisted CNFs connected with the ground and a not twisted head CNF. Such splitted or hierarchical CNF structures are in the focus of interest for their potential use to mimic hierarchical structures in nature, such as those of a gecko. More research on this area is necessary to grow 'real' hierarchical structures with more contacts at the top which will improve the adhesion properties and mimicking better the nanostructures of a real gecko.

The original goal of my work was to grow dense arrays of free-standing hierarchical CNTs for their use as dry adhesives. However, there might be another possibility to grow hierarchical CNT based structures by using a cycle of CNT forest growth, passivation and catalyst deposition (Figure 6.1 a). Garcia *et al.* [195] and Hart & Slocum [106] demonstrated CNT forest growth of different sizes from controlled deposition of catalyst arrays on the substrate. As shown in Figure 6.1 b), CNT forests were grown with different sizes down to free standing CNT forests with diameters down to several µm. Figure 6.1 c) shows the idea as a detailed fabrication cycle to achieve a two-level hierarchical structure which can be extended by adding cycles to achieve a multi-level hierarchical structure which comes closer to the hierarchical system of a real gecko. This fabrication cycle starts with a 10 nm Al_2O_3 layer on a silicon substrate. After the deposition of 1 nm Fe over the whole substrate followed by a growth, CNT forests arise covering the whole substrate, followed by sputtering a 100 nm tungsten layer on the top of the CNF forest for passivation. The tungsten covers the Fe catalysts placed on the top of the CNTs and prohibit due to their high melting point of 3422 °C [196] the continuous CNT growth of the achieved structures in the following growth cycles. After deposition of a new 10 nm Al_2O_3 layer on the top of the tungsten layer, structured deposition of 1 nm Fe can be performed by using lithography or a sputter process. Followed by a new CNT growth, CNT forests grow on the positions of deposited catalysts leading to a two-level hierarchical structure.

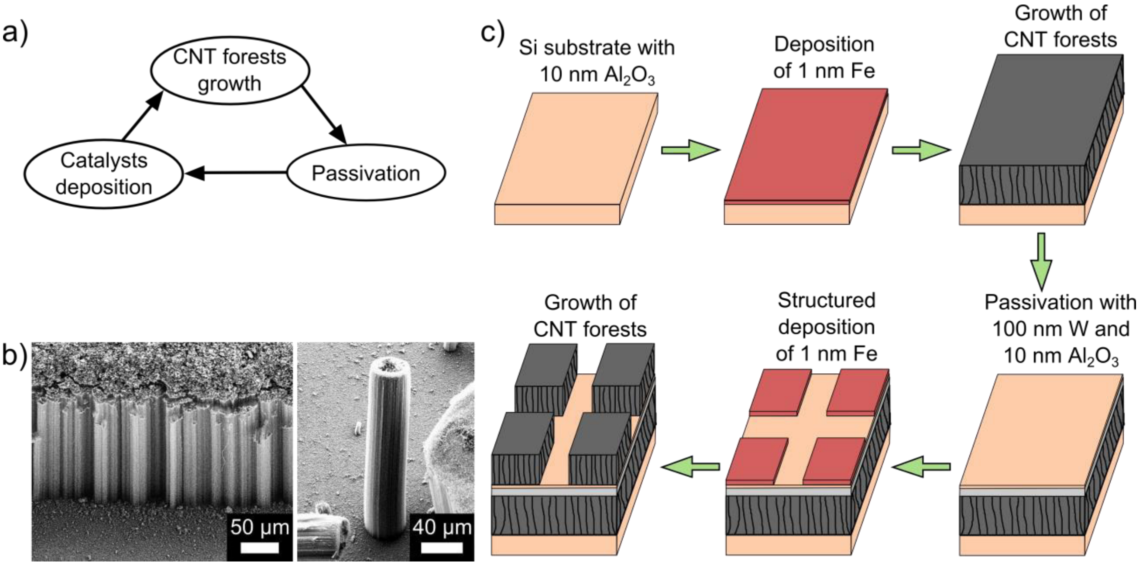

Figure 6.1: Hierarchical dry adhesives made by CNT forests grown in CVD. a) The production cycle with catalyst deposition, growth of CNT forests and passivation to achieve hierarchical structures of CNT forests. b) Different sizes of CNTs forests were grown by CVD, with a big CNT forest on the left side and a CNT forest pillar with a diameter of about 40 µm on the right side. c) Detailed cycle to grow a two-level hierarchical structure of CNT forests. The CNT forests would grow from a 1 nm Fe layer on a 10 nm Al_2O_3 substrate. For the passivation, a layer of 100 nm tungsten covering the Fe catalysts is used. Tungsten benefits from a high melting point and do not reveal CNF growth. Subsequently the Fe catalysts at the top of the CNTs covered with tungsten cannot continue CNT growth.

Another point of my research presented in this work was the invention and controlled growth of twisted lambda shaped CNFs due to increased flame velocities, achieved in a channel structure. More research is necessary to investigate the influence of the flame velocity on the grown structures. Figure 6.2 shows the design of an experimental setup to conduct flame synthesis experiments under different flame velocities. Therefore, gaseous argon (Ar) under pressure is guided into a glass with liquid ethanol (C_2H_6O). The ethanol is heated to ~50 °C to improve the process of ethanol enrichment of the argon gas. Then, the gas mixture goes through another glass with water working as a valve to prevent that gas can go back to the liquid ethanol. The argon-ethanol gas is mixed in a mixing chamber with gaseous oxygen (O_2) under pressure. A jet nozzle at the outlet accelerates the gas and an external flame at the outlet ignites the gas mixture. The sample is placed directly in the ethanol flame. The flame velocity is dependent on the geometry of the jet nozzle and the pressure of the two gases. With this setup, the influence of the flame velocities on the geometry of the CNFs could be investigated.

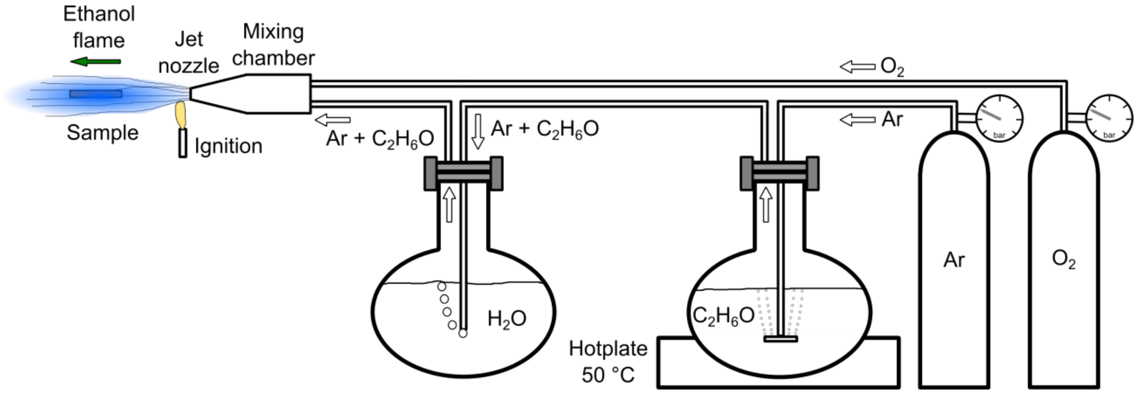

Figure 6.2: Schematic setup of an ethanol flame synthesis with adjustable velocity for the growth investigation of twisted lambda shaped CNFs. Therefore, gaseous argon (Ar) under pressure is guided into a glass with liquid ethanol (C_2H_6O). The ethanol is heated to ~50 °C to improve the process of ethanol enrichment of the argon gas. Then, the gas mixture goes through another glass with water working as a valve to prevent that gas flows back to the liquid ethanol. The argon-ethanol gas is mixed in a mixing chamber with gaseous oxygen (O_2) under pressure. A jet nozzle at the outlet accelerates the gas and an external flame at the outlet ignites the gas mixture. The sample is placed directly in the ethanol flame. The flame velocity dependents on the geometry of the jet nozzle and the pressure of the two gases.

As shown in Chapter 5.4.1, the catalytic center of the lambda shaped CNFs consist of a Ni/Cu alloy (1:20), which is assumable responsible for the growth of two CNFs from one catalytic center. It might be possible that other metals can be mixed to the $NiCl_2$ catalysts, resulting in the growth of novel structures after flame synthesis. Therefore, potassium was selected due to its low boiling point (compared with other metals) of 774 °C, which is in the same range as the temperature of the ethanol flame. For the experiment, a KCl solution in water (20 mg/mL) was mixed with the $NiCl_2$ solution in ethanol (20 mg/mL). A small droplet (1 µL) of this mixed solution was deposited on the substrate. The substrate is the same as for lambda shaped CNFs (see Chapter 5.1). The sample was dried in air and exposed to the ethanol flame for 10 minutes. SEM investigations of the grown structures revealed that ~20 % of the nanostructures have three feet (Figure 6.3), whereas the other structures have two feet and are ΛCNFs.

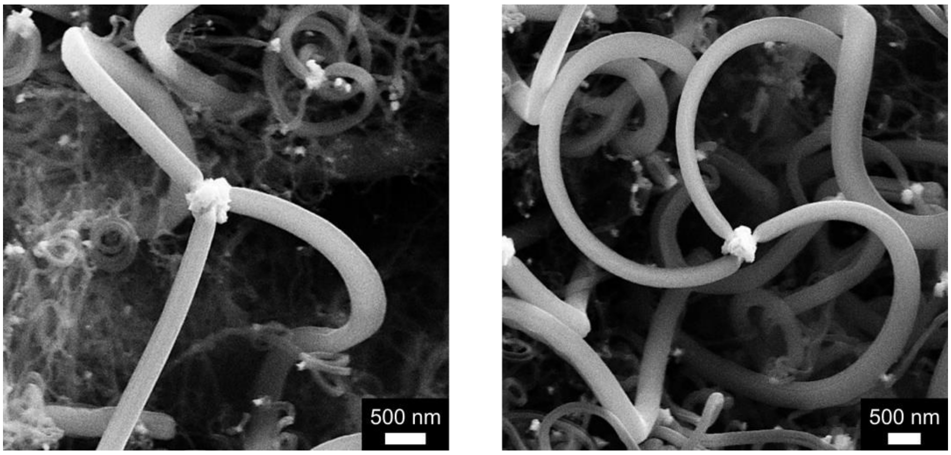

Figure 6.3: Nanotriplefibers grown with flame synthesis. The same setup as for lambdas shaped CNFs was used with the addition of KCl to the $NiCl_2$ solution. The Nanotriplefibers have three feet connected with the ground and in opposite direction the three CNFs end in one catalytic center.

I named the CNFs with three feet due to their appearance nanotriplefibers (NTFs). NTFs have three feet CNFs connected with the ground and on the other end they are connected to one catalytic center. However, more research to grow NTFs in a more controlled way is necessary to understand how they grow and maybe find possibilities to invert NTFs, as well as lambda shaped CNFs, to achieve a kind of hierarchical structure for mimicking the adhesion of a gecko.

Acknowledgements

At first I would like to thank Dr. Julia Syurik and PD Dr. Hendrik Hölscher who gave me the opportunity to conduct my PhD at the KIT and a special thank goes to my supervisor PD Dr. Hendrik Hölscher for his support during my research. Furthermore, I would like to thank the co-referees of my PhD thesis Prof. Dr. Martin Dienwiebel and Prof. Dr. André Schirmeisen. Moreover, I would like to thank Prof. Dr. Robert Stieglitz for guiding as a chair through my PhD examination.

It is a pleasure to thank the people with whom I worked together in the last four years: my students Tobias Loritz and Zeyu Ma, which I am supervised during their thesis, leading also to helpful knowledge and facilities for my work; the students Gökay Ersengün, Luisa Borgmann, Louise Wende and Sabessane Mounirattinam, which I partially supervised during their Master Thesis or research internship; my research group colleagues Richard Thelen, Julia Syurik, Maryna Kavalenka, Radwanul Siddique, Senta Schauer, Claudia Zeiger, Felix Vüllers and Weibin Wu; my PhD colleagues from my office Tobias, Felix, Randy and Florian; the technical and scientific staff of my institute for their helpful support and advice Frank Winkler, Markus Guttmann, Marco Heiler, Paul Abaffy, Giuseppe Papagno and Alexandra Moritz.

It is a honor to acknowledge my cooperation partners for their support and discussions leading to outstanding results; Sharali Malik and Sergei Lebedkin from the INT for the growth of CNTs by CVD including the development of customized setups for CNT growth during my first year; Prof. Manfred Kappes from the INT for suggesting to build up my own machine for CNT/CNF growth; Martin Sommer and Mustahsin Adib for offering me an oven with controllers and process gasses which I modified to a CVD machine for CNF growth. Oleg Il'in and Oleg Ageev from the Southern Federal University in Russia for their helpful discussion and growth of aligned CNTs with PECVD for my studies; Michael Bruns from the IAM for very helpful XPS measurements of my samples; Christian Kübel and C. N. Shyam Kumar from the INT for HRTEM investigations of my CNTs/CNFs; Christian Greiner from the IAM for FIB experiments including the cutting of lambda shaped CNFs; Uwe Bog and Michael Hirtz for our extended cooperation on the controlled growth of lambda shaped CNFs with DPN and µCS; Amandine Charles and Pierre Jouanne from Thales Alenia Space for helpful discussions and conducting space environment experiments for my CNT sample.

I am delighted to mention the financial support from: the WE Heraeus Communication Programme of the “Deutsche Physikalische Gesellschaft” for visiting the spring Meeting of the DPG in Regensburg 2016; the German-Japanese University Network (HeKKSaGOn) for visiting the HeKKSaGOn Kyoto University Winter School in Kyoto 2016. My work was partly carried out with the facilities of the Karlsruhe Nano Micro Facility (KNMF). Furthermore, I would like to thank the University of Stuttgart where I studied mechanical engineering to give me an Erasmus stipendium to study one semester at the University of Exeter in England in 2013 improving my language skills.

I would like to thank my family for their support during my engineering study and my PhD. A special thank goes to the University triathlon sport group of KIT. Regular endurance sport on a daily basis gave me a clear mind, which provided me with fascinating and creative ideas flowing into my work and advancing my PhD.

Finally, it should be mentioned that this work would never be possible without getting free time and space in the second half of my PhD time to following my preferred two scientific working principles with: “Do whatever you can, with whatever you have, wherever you are” [197] and “If you are standing in front of a huge and difficult scientific challenge, does it like the red squirrel: approach slowly!” [From myself], which finally made my PhD to a full success.

List of publications

Articles

Christian Lutz, Julia Syurik, C. N. Shyam Kumar, Christian Kübel, Michael Bruns and Hendrik Hölscher. *Dry adhesives from carbon nanofibers grown in an open ethanol flame,* Beilstein Journal of Nanotechnology, **8**, 2719-2728 (2017)

Christian Lutz, Zeyu Ma, Richard Thelen, Julia Syurik, Oleg Il'in, Oleg Ageev, Pierre Jouanne and Hendrik Hölscher. *Analysis of Carbon Nanotube Arrays for Their Potential Use as Adhesives Under Harsh Conditions as in Space Technology*, Tribology Letters, **67**, 1-10 (2019)

Weibin Wu, **Christian Lutz**, Simon Mersch, Richard Thelen, Christian Greiner, Guillaume Gomard and Hendrik Hölscher. *Characterization of the microscopic tribological properties of sandfish (Scincus scincus) scales by atomic force microscopy*, Beilstein Journal of Nanotechnology, **9**, 2618-2627 (2018)

Christian Lutz, Uwe Bog, Tobias Loritz, Julia Syurik, Sharali Malik, C.N. Shyam Kumar, Christian Kübel, Michael Bruns, Christian Greiner, Michael Hirtz and Hendrik Hölscher. *Locally controlled growth of individual lambda-shaped carbon nanofibers*, accepted for publication in Small (2019)

Conference contributions

Oral presentations

Christian Lutz, Julia Syurik and Hendrik Hölscher. *Bio-inspired Dry Adhesives from Y-shaped Carbon Nanotubes*, HeKKSaGOn Kyoto University Winter School, February 19, 2016, Kyoto, Japan

Christian Lutz, Julia Syurik, Sharali Malik, Sergei Lebedkin and Hendrik Hölscher. *Bioinspired dry adhesives from carbon nanotubes*, 80th Annual Meeting of the DPG and Spring Meeting, March 10, 2016, Regensburg, Germany

Posters

Christian Lutz, Julia Syurik and Hendrik Hölscher. *Bio-inspired Dry Adhesives from Y-shaped Carbon Nanotubes*, HeKKSaGOn Kyoto University Winter School, February 19, 2016, Kyoto, Japan

Christian Lutz, Julia Syurik and Hendrik Hölscher. Gecko-inspired dry adhesives for harsh environments, Heraeus-Seminar: Bio-inspired, Nano- and Microstructured Surfaces: New Functionality by Material and Structure, May 30, 2017, Bad Honnef, Germany

Bibliography

[1] B. Bhushan, “Biomimetics: lessons from nature - an overview,” *Phil. Trans. R. Soc. A, 367*, pp. 1445–1486, 2009.

[2] W. Nachtigall, *Bionik: Grundlagen für Ingenieure und Naturwissenschaftler*, 2nd ed. Berlin Heidelberg: Springer-Verlag, 2002.

[3] Y. Bar-Cohen, *Biomimetics: Nature-Based Innovation*. Boca Raton: CRC Press, 2011.

[4] K. Autumn, “How Gecko Toes Stick,” *Am. Sci.*, vol. 94, pp. 124–132, 2006.

[5] K. Autumn, Y. A. Liang, S. T. Hsieh, W. Zesch, W. P. Chan, T. W. Kenny, R. Fearing, and R. J. Full, “Adhesive force of a single gecko foot-hair,” *Nature*, vol. 405, pp. 681–685, 2000.

[6] W. Barthlott, Z. Cerman, and A. K. Stosch, “Der Lotus-Effekt: Selbstreinigende Oberflächen und ihreÜbertragung in die Technik,” *Biol. unserer Zeit*, vol. 34, no. 5, pp. 290–296, 2004.

[7] K. Autumn, M. Sitti, Y. A. Liang, A. M. Peattie, W. R. Hansen, S. Sponberg, T. W. Kenny, R. Fearing, J. N. Israelachvili, and R. J. Full, “Evidence for van der Waals adhesion in gecko setae,” *Proc. Natl. Acad. Sci. U. S. A.*, vol. 99, no. 19, pp. 12252–12256, Sep. 2002.

[8] W. Federle, K. Rohrseitz, and B. Hölldobler, “Attachment forces of ants measured with a centrifuge: better ‘wax-runners’ have a poorer attachment to a smooth surface,” *J. Exp. Biol.*, vol. 203, no. Pt 3, pp. 505–512, 2000.

[9] H. Peisker, J. Michels, and S. N. Gorb, “Evidence for a material gradient in the adhesive tarsal setae of the ladybird beetle Coccinella septempunctata,” *Nat. Commun.*, vol. 4, p. 1661, 2013.

[10] A. Gasparetto, T. Seidl, and R. Vidoni, “A Mechanical Model for the Adhesion of Spiders to Nominally Flat Surfaces,” *J. Bionic Eng.*, vol. 6, no. 2, pp. 135–142, 2009.

[11] C. Menon, M. Murphy, and M. Sitti, “Gecko Inspired Surface Climbing Robots,” *2004 IEEE Int. Conf. Robot. Biomimetics*, pp. 431–436, 2004.

[12] “Used under license from Shutterstock.com, photographer: Eric Isselee.” .

[13] “Copyright Kellar Autumn.” [Online]. Available: geckolab.lclark.edu. [Accessed: 10-Feb-2015].

[14] B. C. Mahendra, “Contributions to the bionomics, anatomy reproduction and development of the Indian house gecko, Hemidactylus faviviridis Rüppel,” *Proc. Indian Acad. Sci. - Sect. B*, pp. 288–306, 1941.

[15] U. Hiller, “Untersuchungen zum Feinbau und zur Funktion der Haftborstn von Reptilien,” *Z. Morph. Tiere.*, vol. 62, pp. 307–362, 1968.

[16] R. Ruibal and V. Ernst, “The structure of the digital setae of lizards,” *J. Morphol.*, vol. 117, pp. 271–294, 1965.

[17] K. Autumn and N. Gravish, “Gecko adhesion: evolutionary nanotechnology,” *Philos. Trans. R. Soc. A Math. Phys. Eng. Sci.*, vol. 366, no. 1870, pp. 1575–1590, 2008.

[18] Y. Mengüc, M. Röhrig, U. Abusomwan, H. Hölscher, and M. Sitti, “Staying sticky: contact self-cleaning of gecko-inspired adhesives,” *R. Soc.*, pp. 1–12, 2014.

[19] E. Arzt, S. Gorb, and R. Spolenak, “From micro to nano contacts in biological attachment devices,” *Proc. Natl. Acad. Sci. U. S. A.*, vol. 100, no. 19, pp. 10603–6, Sep. 2003.

[20] E. Arzt, “Biological and artificial attachment devices: Lessons for materials scientists from flies and geckos,” *Mater. Sci. Eng. C*, vol. 26, no. 8, pp. 1245–1250, 2006.

[21] M. Röhrig, “Fabrication and Analysis of Bio-inspired Smart Surfaces,” *PhD Thesis, KIT*, 2013.

[22] B. Bhushan, “Adhesion of multi-level hierarchical attachment systems in gecko feet,” *J. Adhes. Sci. Technol.*, vol. 21, no. 12–13, pp. 1213–1258, 2007.

[23] B. Bhushan, A. G. Peressadko, and T. W. Kim, “Adhesion analysis of two-level hierarchical morphology in natural attachment systems for ‘smart adhesion,’” *J. Adhes. Sci. Technol.*, vol. 20, no. 13, pp. 1475–1491, 2006.

[24] T. W. Kim and B. Bhushan, “Effect of stiffness of multi-level hierarchical attachment system on adhesion enhancement,” *Ultramicroscopy*, vol. 107, no. 10–11, pp. 902–912, 2007.

[25] T. W. Kim and B. Bhushan, “The adhesion model considering capillarity for gecko attachment system,” *J. R. Soc. Interface*, vol. 5, no. 20, pp. 319–327, 2008.

[26] H. Margenau, “Van der waals forces,” *Rev. Mod. Phys.*, vol. 11, no. 1, pp. 1–35, 1939.

[27] D. Leckband and J. Israelachvili, “Intermolecular forces in biology,” *Q. Rev. Biophys.*, vol. 34, no. 02, pp. 105 – 267, 2001.

[28] E. W. Hawkes, E. V. Eason, A. T. Asbeck, and M. R. Cutkosky, “The Gecko’s toe: Scaling directional adhesives for climbing applications,” *IEEE/ASME Trans. Mechatronics*, vol. 18, no. 2, pp. 518–526, 2013.

[29] M. K. Kwak, H. E. Jeong, and K. Y. Suh, “Rational design and enhanced biocompatibility of a dry adhesive medical skin patch,” *Adv. Mater.*, vol. 23, no. 34, pp. 3949–3953, 2011.

[30] H. E. Jeong, J. Lee, H. N. Kim, S. H. Moon, and K. Y. Suh, “A nontransferring dry adhesive with hierarchical polymer nanohairs,” *PNAS*, vol. 106, no. 14, pp. 5639–5644, 2009.

[31] A. K. Geim, S. V Dubonos, I. V Grigorieva, K. S. Novoselov, A. A. Zhukov, and S. Y. Shapoval, “Microfabricated adhesive mimicking gecko foot-hair,” *Nat. Mater.*, vol. 2, no. 7, pp. 461–463, 2003.

[32] M. Röhrig, M. Thiel, M. Worgull, and H. Hölscher, “3D direct laser writing of nano- and microstructured hierarchical gecko-mimicking surfaces,” *Small*, vol. 8, no. 19, pp. 3009–3015, Oct. 2012.

[33] H. Wilski, “The radiation induced degradation of polymers,” *Int. J. Radiat. Appl. Instrumentation. Part C. Radiat. Phys. Chem.*, vol. 29, no. 1, pp. 1–14, 1987.

[34] R. F. Egerton, S. Lazar, and M. Libera, “Delocalized radiation damage in polymers,” *Micron*, vol. 43, no. 1, pp. 2–7, 2012.

[35] Q. Zhang, *Carbon Nanotubes and Their Applications Carbon Nanotubes and Their Applications*. Singapore: Pan Stanford Publishing Pte. Ltd., 2012.

[36] R. L. Poveda and N. Gupta, *Carbon Nanofiber Reinforced Polymer Composites*. Basel: Springer International Publishing, 2016.

[37] L. Ge, S. Sethi, L. Ci, P. M. Ajayan, and A. Dhinojwala, “Carbon nanotube-based synthetic gecko tapes,” *Proc. Natl. Acad. Sci. U. S. A.*, vol. 104, no. 26, pp. 10792–10795, Jun. 2007.

[38] S. Hu, Z. Xia, and L. Dai, “Advanced gecko-foot-mimetic dry adhesives based on carbon nanotubes,” *Nanoscale*, vol. 5, no. 2, pp. 475–486, 2013.

[39] C. Lutz, J. Syurik, C. N. Shyam Kumar, C. Kübel, M. Bruns, and H. Hölscher, “Dry adhesives from carbon nanofibers grown in an open ethanol flame,” *Beilstein J. Nanotechnol.*, vol. 8, pp. 2719–2728, 2017.

[40] L. Qu and L. Dai, “Gecko-Foot-Mimetic Aligned Single-Walled Carbon Nanotube Dry Adhesives with Unique Electrical and Thermal Properties,” *Adv. Mater.*, vol. 19, pp. 3844–3849, 2007.

[41] L. Qu, L. Dai, M. Stone, Z. Xia, and L. W. Zhong, “Carbon nanotube arrays with strong shear binding-on and easy normal lifting-off,” *Science (80-.).*, vol. 322, pp. 238–242, 2008.

[42] B. G. Demczyk, M. Wang, J. Cumingd, M. Hetamn, W. Han, A. Zettl, and R. Ritchie, “Direct mechanical measurements of the tensile strength and elastic modulus of multi-walled carbon nanotubes,” *Mater. Sci. Eng. A.*, vol. 334, no. 1–2, pp. 173–178, 2002.

[43] G. Gao, T. Cagin, and W. A. Goddard, “Energetics , structure , mechanical and vibrational properties of single-walled carbon nanotubes,” *Nanotechnology*, vol. 9, pp. 184–191, 1998.

[44] A. Dorigato, M. Brugnara, and A. Pegoretti, “Novel polyamide 12 based nanocomposites for industrial applications,” *J. Polym. Res.*, vol. 24, no. 6, pp. 1–13, 2017.

[45] G. Y. Gerasimov, “Radiation stability of carbon nanostructures,” *J. Eng. Phys. Thermophys.*, vol. 83, no. 2, pp. 393–400, 2010.

[46] E. T. Thostenson, C. Li, and T. W. Chou, “Nanocomposites in context,” *Compos. Sci. Technol.*, vol. 65, no. 3–4, pp. 491–516, 2005.

[47] Y. C. Choi and W. Choi, “Synthesis of Y-junction single-wall carbon nanotubes,” *Carbon N. Y.*, vol. 43, no. 13, pp. 2737–2741, Nov. 2005.

[48] N. Gothard, C. Daraio, J. Gaillard, R. Zidan, S. Jin, and A. M. Rao, “Controlled Growth of Y-Junction Nanotubes Using Ti-Doped Vapor Catalyst,” *Nano Lett.*, vol. 4, no. 2, pp. 213–217, Feb. 2004.

[49] B. C. Satishkumar, P. J. Thomas, A. Govindaraj, and C. N. R. Rao, “Y-junction carbon nanotubes,” *Appl. Phys. Lett.*, vol. 77, no. 16, pp. 2530–2, 2000.

[50] Q. Wei, Y. Liu, L. Zhang, and S. Huang, “Growth and Formation Mechanism of Branched Carbon Nanotubes by Pyrolysis of Iron(II) Phthalocyanine,” *Nano-Micro Lett.*, vol. 5, no. 2, pp. 124–128, Jun. 2013.

[51] M. Yudasaka, R. Kikuchi, T. Matsui, Y. Ohki, S. Yoshimura, and E. Ota, “Specific conditions for Ni catalyzed carbon nanotube growth by chemical vapor deposition,” *Appl. Phys. Lett.*, vol. 67, no. 1995, p. 2477, 1995.

[52] Z. Ren, Z. Huang, J. Xu, J. Wang, P. Bush, M. Siegal, and P. Provencio, “Synthesis of large arrays of well-aligned carbon nanotubes on glass,” *Science (80-.).*, vol. 282, no. 5391, pp. 1105–7, 1998.

[53] M. De Volder, S. Tawfick, R. Baughman, and A. Hart, “Carbon Nanotubes: Present and Future Commercial Applications,” *Science (80-.).*, vol. 339, pp. 535–539, 2013.

[54] B. Chen, G. Zhong, P. G. Oppenheimer, C. Zhang, H. Tornatzky, S. Esconjauregui, S. Hofmann, and J. Robertson, “Influence of Packing Density and Surface Roughness of Vertically- Aligned Carbon Nanotubes on Adhesive Properties of Gecko- Inspired Mimetics,” *ACS Appl. Mater. Interfaces*, vol. 7, p. 3626−3632, 2015.

[55] H. W. Kroto, J. R. Heath, S. C. O’Brien, R. F. Curl, and R. E. Smalley, “C 60: Buckminsterfullerene,” *Nature*, vol. 318, pp. 162–163, 1985.

[56] S. Iijima, “Helical microtubules of graphitic carbon,” *Nature*, vol. 354, pp. 56–58, 1991.

[57] A. Krishnan, E. Dujardin, T. W. Ebbesen, P. N. Yianilos, and M. M. J. Treacy, “Young’s modulus of single-walled nanotubes,” *Phys. Rev. B*, vol. 58, no. 20, pp. 13–19, 1998.

[58] M. Yu, “Strength and Breaking Mechanism of Multiwalled Carbon Nanotubes Under Tensile Load,” *Science (80-.).*, vol. 287, no. 5453, pp. 637–640, 2000.

[59] F. Li, H. M. Cheng, S. Bai, and G. Su, “Tensile strength of single-walled carbon nanotubes directly measured from their macroscopic ropes,” *Appl. Phys. Lett.*, vol. 77, no. 2000, pp. 3161–3163, 2000.

[60] R. Saito, M. Fujita, G. Dresselhaus, and M. S. Dresselhaus, “Electronic structure of graphene tubules,” *Appl. Phys. Lett.*, vol. 60, no. 18, pp. 2204–2206, 1992.

[61] P. R. Bandaru, “Electrical Properties and Applications of Carbon Nanotube Structures,” *J. Nanosci. Nanotechnol.*, vol. 7, no. 4, pp. 1239–1267, 2007.

[62] H. Nagai, Y. Okazaki, S. H. Chew, N. Misawa, Y. Yamashita, S. Akatsuka, T. Ishihara, K. Yamashita, Y. Yoshikawa, H. Yasui, L. Jiang, H. Ohara, T. Takahashi, G. Ichihara, K. Kostarelos, Y. Miyata, H. Shinohara, and S. Toyokuni, “Diameter and rigidity of multiwalled carbon nanotubes are critical factors in mesothelial injury and carcinogenesis,” *Proc. Natl. Acad. Sci.*, vol. 108, no. 49, pp. E1330–E1338, 2011.

[63] C. Shen, A. H. Brozena, and Y. Wang, “Double-walled carbon nanotubes: Challenges and opportunities,” *Nanoscale*, vol. 3, no. 2, pp. 503–518, 2011.

[64] Y. Li, K. Wang, J. Wei, Z. Gu, Z. Wang, J. Luo, and D. Wu, “Tensile properties of long aligned double-walled carbon nanotube strands,” *Carbon N. Y.*, vol. 43, no. 1, pp. 31–35, 2005.

[65] S. Zhang, W. K. Liu, and R. S. Ruoff, “Atomistic Simulations of Double-Walled Carbon Nanotubes (DWCNTs) as Rotational Bearings,” *Nano Lett.*, vol. 4, no. 2, pp. 293–297, 2004.

[66] C. Li, “Elastic moduli of multi-walled carbon nanotubes and the effect of van der Waals forces,” *Compos. Sci. Technol.*, vol. 63, no. 11, pp. 1517–1524, 2003.

[67] S. H. Kim, G. W. Mulholland, and M. R. Zachariah, “Density measurement of size selected multiwalled carbon nanotubes by mobility-mass characterization,” *Carbon N. Y.*, vol. 47, no. 5, pp. 1297–1302, 2009.

[68] U. Fischer, R. Gomeringer, M. Heinzler, R. Kilgus, F. Näher, S. Oesterle, H. Paetzold, and A. Stephan, *Tabellenbuch Metall*, 44th ed. Haan-Gruiten: Europa Lehrmittel, 2008.

[69] C. J. Lee, J. Park, and J. A. Yu, "Catalyst effect on carbon nanotubes synthesized by thermal chemical vapor deposition," *Chem. Phys. Lett.*, vol. 360, no. 3–4, pp. 250–255, 2002.

[70] J. Lu, S. S. Yi, T. Kopley, C. Qian, J. Liu, and E. Gulari, "Fabrication of ordered catalytically active nanoparticles derived from block copolymer micelle templates for controllable synthesis of single-walled carbon nanotubes," *J. Phys. Chem. B*, vol. 110, no. 13, pp. 6655–6660, 2006.

[71] A. Moisala, A. G. Nasibulin, and E. I. Kauppinen, "The role of metal nanoparticles in the catalytic production of single-walled carbon nanotubes - a review," *J. Phys. - Condens. Matter*, vol. 15, pp. S3011 – S3035, 2003.

[72] H. Yokoyama, H. Numakura, and M. Koiwa, "The solubility and diffusion of carbon in palladium," *Acta Mater.*, vol. 46, no. 8, pp. 2823–2830, 1998.

[73] M. Kumar, "Carbon Nanotube Synthesis and Growth Mechanism," in *Carbon Nanotubes - Synthesis, Characterization, Applications;*, 1st ed., S. Yellampalli, Ed. Prague: InTech, 2011.

[74] D. Yuan, L. Ding, H. Chu, Y. Feng, T. P. McNicholas, and J. Liu, "Horizontally aligned single-walled carbon nanotube on quartz from a large variety of metal catalysts," *Nano Lett.*, vol. 8, no. 8, pp. 2576–9, Aug. 2008.

[75] A. M. Cassell, Q. Ye, B. A. Cruden, J. Li, P. C. Sarrazin, H. T. Ng, J. Han, and M. Meyyappan, "Combinatorial chips for optimizing the growth and integration of carbon nanofibre based devices," *Nanotechnology*, vol. 15, no. 1, pp. 9–15, Jan. 2004.

[76] T. De Los Arcos, M. G. Garnier, J. W. Seo, P. Oelhafen, V. Thommen, and D. Mathys, "The influence of catalyst chemical state and morphology on carbon nanotube growth," *J. Phys. Chem. B*, vol. 108, no. 23, pp. 7728–7734, 2004.

[77] A. Cao, P. M. Ajayan, G. Ramanath, R. Baskaran, and K. Turner, "Silicon oxide thickness-dependent growth of carbon nanotubes," *Appl. Phys. Lett.*, vol. 84, no. 1, pp. 109–111, 2004.

[78] R. N. Pease and R. S. Cook, "Equilibrium in the reaction, NiO + H2 ⇌ Ni + H2O. The free energy of nickelous oxide," *J. Am. Chem. Soc.*, vol. 48, no. 5, pp. 1199–1206, 1926.

[79] R. N. A. R. Seman, M. A. Azam, and M. A. Mohamed, "Highly efficient growth of vertically aligned carbon nanotubes on Fe–Ni based metal alloy foils for supercapacitors," *Adv. Nat. Sci. Nanosci. Nanotechnol.*, vol. 7, no. 4, p. 045016, 2016.

[80] M. Häffner, A. Haug, R. T. Weitz, M. Fleischer, M. Burghard, H. Peisert, T. Chassé, and D. P. Kern, "E-beam lithography of catalyst patterns for carbon nanotube growth on insulating substrates," *Microelectron. Eng.*, vol. 85, no. 5–6, pp. 768–773, 2008.

[81] L. Dubrovina, O. Naboka, V. Ogenko, P. Gatenholm, and P. Enoksson, "One-pot synthesis of carbon nanotubes from renewable resource: Cellulose acetate," *J. Mater. Sci.*, vol. 49, no. 3, pp. 1144–1149, 2014.

[82] I. Kuljanishvili, D. A. Dikin, S. Rozhok, S. Mayle, and V. Chandrasekhar, "Controllable patterning and CVD growth of isolated carbon nanotubes with direct parallel writing of catalyst using dip-pen Nanolithography," *Small*, vol. 5, no. 22, pp. 2523–2527, 2009.

[83] A. Kosiorek, W. Kandulski, P. Chudzinski, K. Kempa, and M. Giersig, "Shadow nanosphere lithography: Simulation and experiment," *Nano Lett.*, vol. 4, no. 7, pp. 1359–1363, 2004.

[84] J. Rybczynski, K. Kempa, Y. Wang, Z. F. Ren, J. B. Carlson, B. R. Kimball, and G. Benham, "Visible light diffraction studies on periodically aligned arrays of carbon nanotubes: Experimental and theoretical comparison," *Appl. Phys. Lett.*, vol. 88, no. 20, pp. 10–13, 2006.

[85] Z. P. Huang, D. L. Carnahan, J. Rybczynski, M. Giersig, M. Sennett, D. Z. Wang, J. G. Wen, K. Kempa, and Z. F. Ren, "Growth of large periodic arrays of carbon nanotubes," *Appl. Phys. Lett.*, vol. 82, no. 3, pp. 460–462, 2003.

[86] J. Bansmann, S. Kielbassa, H. Hoster, F. Weigl, H. G. Boyen, U. Wiedwald, P. Ziemann, and R. J. Behm, "Controlling the Interparticle Spacing of Au - Salt Loaded Micelles and Au Nanoparticles on Flat Surfaces," *Langmuir*, vol. 23, no. 20, pp. 10150–10155, 2007.

[87] R. D. Bennett, A. C. Miller, N. T. Kohen, P. T. Hammond, D. J. Irvine, and R. E. Cohen, "Strategies for Controlling the Planar Arrangement of Block Copolymer Micelles and Inorganic Nanoclusters,"

Macromolecules, vol. 38, no. 26, pp. 10728–10735, Dec. 2005.

[88] M. Bräutigam, P. Weyell, T. Rudolph, J. Dellith, S. Krieck, H. Schmalz, F. H. Schacher, and B. Dietzek, “Porous NiOx nanostructures templated by polystyrene-block-poly(2-vinylpyridine) diblock copolymer micelles,” *J. Mater. Chem. A*, vol. 2, no. 17, p. 6158, 2014.

[89] G. Kästle, H.-G. Boyen, F. Weigl, G. Lengl, T. Herzog, P. Ziemann, S. Riethmüller, O. Mayer, C. Hartmann, J. P. Spatz, M. Möller, M. Ozawa, F. Banhart, M. G. Garnier, and P. Oelhafen, “Micellar Nanoreactors—Preparation and Characterization of Hexagonally Ordered Arrays of Metallic Nanodots,” *Adv. Funct. Mater.*, vol. 13, no. 11, pp. 853–861, Nov. 2003.

[90] L. Shan, S. Punniyakoti, M. J. Van Bael, K. Temst, M. K. Van Bael, X. Ke, S. Bals, G. Van Tendeloo, M. D’Olieslaeger, P. Wagner, K. Haenen, and H.-G. Boyen, “Homopolymers as nanocarriers for the loading of block copolymer micelles with metal salts: a facile way to large-scale ordered arrays of transition-metal nanoparticles,” *J. Mater. Chem. C*, vol. 2, no. 4, pp. 701–707, 2014.

[91] J. P. Spatz, S. Mössmer, C. Hartmann, M. Möller, T. Herzog, M. Krieger, H.-G. Boyen, and P. Ziemann, “Ordered Deposition of Inorganic Clusters from Micellar Block Copolymer Films,” *Langmuir*, vol. 16, no. 6, pp. 407–415, 2000.

[92] V. V Terekhin, O. V Dement’eva, and V. M. Rudoy, “Formation of ordered nanoparticle assemblies by block copolymer lithography methods,” *Russ. Chem. Rev.*, vol. 80, no. 5, pp. 453–472, May 2011.

[93] R. D. Bennett, A. J. Hart, and R. E. Cohen, “Controlling the Morphology of Carbon Nanotube Films by Varying the Areal Density of Catalyst Nanoclusters Using Block-Copolymer Micellar Thin Films,” *Adv. Mater.*, vol. 18, no. 17, pp. 2274–2279, Sep. 2006.

[94] R. D. Bennett, G. Y. Xiong, Z. F. Ren, and R. E. Cohen, “Using Block Copolymer Micellar Thin Films as Templates for the Production of Catalysts for Carbon Nanotube Growth,” *Chem. Mater.*, vol. 16, no. 26, pp. 5589–5595, Dec. 2004.

[95] V. Jourdain and C. Bichara, “Current understanding of the growth of carbon nanotubes in catalytic chemical vapour deposition,” *Carbon N. Y.*, vol. 58, pp. 2–39, 2013.

[96] A. R. Harutyunyan, T. Tokune, and E. Mora, “Liquid as a required catalyst phase for carbon single-walled nanotube growth,” *Appl. Phys. Lett.*, vol. 87, no. 5, pp. 2003–2006, 2005.

[97] W. H. Qi, “Size effect on melting temperature of nanosolids,” *Phys. B Condens. Matter*, vol. 368, no. 1–4, pp. 46–50, Nov. 2005.

[98] C. E. Housecroft and E. C. Constable, *Chemistry: An Introduction to Organic, Inorganic and Physical Chemistry*, 4th ed. Harlow: Pearson Education, 2010.

[99] K. K. Nanda, S. N. Sahu, and S. N. Behera, “Liquid-drop model for the size-dependent melting of low-dimensional systems,” *Phys. Rev. A*, vol. 66, no. 1, p. 013208, Jul. 2002.

[100] Y. Ando and X. Zhao, “Synthesis of Carbon Nanotubes by Arc-Discharge Method,” *New Diam. Forntier Carbon Technol.*, vol. 16, no. 3, pp. 123–137, 2006.

[101] T. Guo, P. Nikolaev, A. Thess, D. T. Colbert, and R. E. Smalley, “Catalytic growth of single-walled manotubes by laser vaporization,” *Chem. Phys. Lett.*, vol. 243, no. 1–2, pp. 49–54, 1995.

[102] A. Szabó, C. Perri, A. Csató, G. Giordano, D. Vuono, and J. B. Nagy, “Synthesis methods of carbon nanotubes and related materials,” *Materials (Basel).*, vol. 3, no. 5, pp. 3092–3140, 2010.

[103] J. Yang, S. Esconjauregui, R. Xie, H. Sugime, T. Makaryan, L. D. Arsie, D. Leonardo, G. Arellano, S. Bhardwaj, C. Cepek, and J. Robertson, “Effect of Oxygen Plasma Alumina Treatment on Growth of Carbon Nanotube Forests,” *Phys. Chem.*, vol. 118, no. 32, pp. 18683–92, 2014.

[104] Y. Yun, V. Shanov, Y. Tu, S. Subramaniam, and M. J. Schulz, “Growth Mechanism of Long Aligned Multiwall Carbon Nanotube Arrays by Water-Assisted Chemical Vapor Deposition,” *J. Phys. Chem. B*, vol. 110, no. 47, pp. 23920–23925, 2006.

[105] M. De Volder, S. Park, S. Tawfick, and A. J. Hart, “Strain-engineered manufacturing of freeform carbon nanotube microstructures,” *Nat. Commun.*, vol. 5, pp. 1–9, 2014.

[106] A. J. Hart and A. H. Slocum, “Rapid Growth and Flow-Mediated Nucleation of Millimeter-Scale Aligned Carbon Nanotube Structures from a Thin-Film Catalyst,” *J. Phys. Chem. B*, vol. 110, p. 8250, 2006.

[107] A. Ural, Y. Li, and H. Dai, “Electric-field-aligned growth of single-walled carbon nanotubes on surfaces,” *Appl. Phys. Lett.*, vol. 81, no. 18, p. 3464, 2002.

[108] Y. Zhang, A. Chang, J. Cao, Q. Wang, W. Kim, Y. Li, N. Morris, E. Yenilmez, J. Kong, and H. Dai, “Electric-field-directed growth of aligned single-walled carbon nanotubes,” *Appl. Phys. Lett.*, vol. 79, no. 19, pp. 3155–3157, 2001.

[109] M. Meyyappan, L. Delzeit, A. Cassell, and D. Hash, “Carbon nanotube growth by PECVD: a revie,” *Plasma Sources Sci. Technol.*, vol. 12, pp. 205–216, 2003.

[110] H.-N. Lin, Y.-H. Chang, J.-H. Yen, J.-H. Hsu, I.-C. Leu, and M.-H. Hon, “Selective growth of vertically aligned carbon nanotubes on nickel oxide nanostructures created by atomic force microscope nano-oxidation,” *Chem. Phys. Lett.*, vol. 399, no. 4–6, pp. 422–425, Dec. 2004.

[111] V. I. Merkulov, D. H. Lowndes, Y. Y. Wei, G. Eres, and E. Voelkl, “Patterned growth of individual and multiple vertically aligned carbon nanofibers,” *Appl. Phys. Lett.*, vol. 76, no. 24, pp. 3555–3557, 2000.

[112] V. I. Merkulov, A. V. Melechko, M. A. Guillorn, D. H. Lowndes, and M. L. Simpson, “Alignment mechanism of carbon nanofibers produced by plasma-enhanced chemical-vapor deposition,” *Appl. Phys. Lett.*, vol. 79, no. 18, pp. 2970–2972, 2001.

[113] C. Bower, W. Zhu, S. Jin, and O. Zhou, “Plasma-induced alignment of carbon nanotubes,” *Appl. Phys. Lett.*, vol. 77, no. 6, pp. 830–832, 2000.

[114] S. Hofmann, C. Ducati, J. Robertson, and B. Kleinsorge, “Low-temperature growth of carbon nanotubes by plasma-enhanced chemical vapor deposition,” *Appl. Phys. Lett.*, vol. 83, no. 1, pp. 135–137, 2003.

[115] Y. Y. Li and C. C. Hsieh, “Synthesis of carbon nanotubes by combustion of a paraffin wax candle,” *Micro Nano Lett.*, vol. 2, no. 4, pp. 63 – 66, 2007.

[116] C. Hsieh, M. Youh, H. Wu, L. Hsu, J. Guo, and Y. Li, “Synthesis of Carbon Nanotubes Using a Butane - Air Bunsen Burner and the Resulting Field Emission Characteristics,” *J. Phys. Chem. C*, vol. 112, pp. 19224–19230, 2008.

[117] Q. Bao and C. Pan, “Electric field induced growth of well aligned carbon nanotubes from ethanol flames,” *Nanotechnology*, vol. 17, no. 4, pp. 1016–21, 2006.

[118] C. Pan, Y. Liu, F. Cao, J. Wang, and Y. Ren, “Synthesis and growth mechanism of carbon nanotubes and nanofibers from ethanol flames,” *Micron*, vol. 35, no. 6, pp. 461–468, 2004.

[119] C. Pan and Q. Bao, “Well-aligned carbon nanotubes from ethanol flame,” *J. Mater. Sci. Lett.*, vol. 21, no. 24, pp. 1927–1929, 2002.

[120] J. Zhang and C. Pan, “Magnetic-field-controlled alignment of carbon nanotubes from flames and its growth mechanism,” *J. Phys. Chem. C*, vol. 112, no. 35, pp. 13470–13474, 2008.

[121] J. Chen and X. Gao, “Recent Advances in the Flame Synthesis of Carbon Nanotubes,” *Am. J. Mater. Synth. Process.*, vol. 2, no. 6, pp. 71–89, 2017.

[122] G. Binnig, C. F. Quate, and C. Gerber, “Atomic Force Microscope,” *Phys. Rev. Lett.*, vol. 56, no. 9, pp. 930–933, 1986.

[123] G. Binnig, C. Gerber, E. Stoll, and T. R. Albrecht, “Atomic resolution with atomic force microscope,” *Europhys. Lett.*, vol. 12, 1987.

[124] A. L. Weisenhorn, P. Maivald, H. J. Butt, and P. K. Hansma, “Measuring adhesion, attraction, and repulsion between surfaces in liquids with an atomic-force microscope,” *Phys. Rev. B*, vol. 45, no. 19, pp. 11226–11232, 1992.

[125] D. F. Ogletree, R. W. Carpick, and M. Salmeron, “Calibration of frictional forces in atomic force microscopy,” *Rev. Sci. Instrum.*, vol. 67, no. 9, pp. 3298–3306, 1996.

[126] A. Wadas, “Magnetic Forces Measured By Atomic Force Microscopy. Theoretical Approach,” *J. Magn. Magn. Mater.*, vol. 72, pp. 295–299, 1988.

[127] P. P. Lehenkari and M. A. Horton, “Single Integrin Molecule Adhesion Forces in Intact Cells Measured by Atomic Force Microscopy,” *Biochem. Biophys. Res. Commun.*, vol. 259, no. 3, pp. 645–650, 1999.

[128] A. L. Weisenhorn, J. E. Mac Dougall, S. A. C. Gould, S. D. Cox, W. S. Wise, J. Massie, P. MaiVald,

V. B. Elings, G. D. Stucky, and P. K. Hansma, “Imaging and Manipulating Molecules on a Zeolite Surface with an Atomic Force Microscope,” *Science (80-.).*, vol. 247, 1990.

[129] M. Yasutake, Y. Ejiri, and T. Hattori, “Modification of Silicon Surface Using Atomic Force Microscope with Conducting Probe.pdf.pdf,” *Jpn. J. Appl. Phys.*, vol. 32, 1993.

[130] T. Junno, K. Deppert, L. Montelius, and L. Samuelson, “Controlled manipulation of nanoparticles with an atomic force microscope,” *Appl. Phys. Lett.*, vol. 66, no. 26, pp. 3627–3629, 1995.

[131] D. Guo, G. Xie, and J. Luo, “Mechanical properties of nanoparticles: basics and applications,” *J. Phys. D. Appl. Phys.*, vol. 47, no. 1, p. 013001, 2014.

[132] F. L. Leite, C. C. Bueno, A. L. Da Róz, E. C. Ziemath, and O. N. Oliveira, “Theoretical models for surface forces and adhesion and their measurement using atomic force microscopy,” *Int. J. Mol. Sci.*, vol. 13, no. 10, pp. 12773–12856, 2012.

[133] BRUKER, *AFM Probes (technical catalog)*. Billerica, 2013.

[134] G. Göring, P. I. Dietrich, M. Blaicher, S. Sharma, J. G. Korvink, T. Schimmel, C. Koos, and H. Hölscher, “Tailored probes for atomic force microscopy fabricated by two-photon polymerization,” *Appl. Phys. Lett.*, vol. 109, no. 6, 2016.

[135] J. E. Schmutz, M. M. Schäfer, and H. Hölscher, “Colloid probes with increased tip height for higher sensitivity in friction force microscopy and less cantilever damping in dynamic force microscopy,” *Rev. Sci. Instrum.*, vol. 79, no. 2 Pt 1, p. 026103, 2008.

[136] W. D. Compton, *Where no man has gone before: A History of Apollo Lunar Exploration Mission*. Washington, DC: The NASA History Series, 1989.

[137] J. Crisp, M. Adler, J. Matijevic, S. Squyres, R. Arvidson, and D. Kass, “Mars Exploration Rover mission,” *Geophys. Res.*, vol. 108, no. 12, pp. 8061–8064, 2003.

[138] J. P. Grotzinger, J. Crisp, A. R. Vasavada, R. C. Anderson, C. J. Baker, R. Barry, D. F. Blake, P. Conrad, K. S. Edgett, B. Ferdowski, R. Gellert, J. B. Gilbert, M. Golombek, J. Gómez-Elvira, D. M. Hassler, L. Jandura, M. Litvak, P. Mahaffy, J. Maki, M. Meyer, M. C. Malin, I. Mitrofanov, J. J. Simmonds, D. Vaniman, R. V. Welch, and R. C. Wiens, “Mars Science Laboratory mission and science investigation,” *Space Sci. Rev.*, vol. 170, no. 1–4, pp. 5–56, 2012.

[139] C. Hirt and W. E. Featherstone, “A 1.5 km-resolution gravity field model of the Moon,” *Earth Planet. Sci. Lett.*, vol. 329–330, pp. 22–30, 2012.

[140] K. E. Wrobel and P. H. Schultz, “Effect of planetary rotation on distal tektite deposition on Mars,” *J. Geophys. Res. E Planets*, vol. 109, no. 5, pp. 1–8, 2004.

[141] K. H. Glassmeier, H. Boehnhardt, D. Koschny, E. Kührt, and I. Richter, “The Rosetta mission: Flying towards the origin of the solar system,” *Space Sci. Rev.*, vol. 128, no. 1–4, pp. 1–21, 2007.

[142] J. Biele, S. Ulamec, L. Richter, J. Knollenberg, E. Kührt, and D. Möhlmann, “The putative mechanical strength of comet surface material applied to landing on a comet,” *Acta Astronaut.*, vol. 65, no. 7–8, pp. 1168–1178, 2009.

[143] E. Hand, “Philae probe makes bumpy touchdown on a comet,” *Science (80-.).*, vol. 346, no. 6212, pp. 900–901, 2014.

[144] S. K. Flegel, J. Gelhaus, M. Möckel, C. Wiedemann, H. Krag, H. Klinkrad, and P. Vörsmann, “Multi-layer insulation model for MASTER-2009,” *Acta Astronaut.*, vol. 69, no. 11–12, pp. 911–922, 2011.

[145] O. Kluge, B. Abendroth, T. Köhler, M. Altenburg, L. Borchardt, T. Schüler, A. Zwiebler, M. Tajmar, and T. Schmiel, “Electrochromics for Thermal Control on Spacecrafts,” in *Proceedings of the 3rd World Congress on Momentum, Heat and Mass Transfer (MHMT’18)*, 2018, vol. 2, pp. 1–8.

[146] “Copyright Thales Alenia Space.” [Online]. Available: exploration.esa.int. [Accessed: 11-Dec-2018].

[147] J. N. Cuzzi, J. E. Colwell, L. W. Esposito, C. C. Porco, C. D. Murray, P. D. Nicholson, L. J. Spilker, E. A. Marouf, R. C. French, N. Rappaport, and D. Muhleman, “Saturn’s Rings: Pre-Cassini Status and Mission Goals,” *Space Sci. Rev.*, vol. 118, pp. 209–251, 2002.

[148] T. G. Northrop and J. E. P. Connerney, “A micrometeorite erosion model and the age of Saturn’s rings,” *Icarus*, vol. 70, no. 1, pp. 124–137, 1987.

[149] K. P. So, D. Chen, A. Kushima, M. Li, S. Kim, Y. Yang, Z. Wang, J. G. Park, Y. H. Lee, R. I. Gonzalez, M. Kiwi, E. M. Bringa, L. Shao, and J. Li, “Dispersion of carbon nanotubes in aluminum

improves radiation resistance," *Nano Energy*, vol. 22, pp. 319–327, 2016.

[150] J. A. VAN ALLEN and L. A. FRANK, "Radiation Around the Earth to a Radial Distance of 107,400 km.," *Nature*, vol. 183, pp. 430–434, 1959.

[151] J. A. ROBERTS and M. M. KOMESAROFF, "Evidence for Asymmetry of Jupiter's Van Allen Belt," *Nature*, vol. 203, pp. 827–830, 1964.

[152] E. M. Galimov, V. P. Kolotov, M. A. Nazarov, Y. a. Kostitsyn, I. V. Kubrakova, N. N. Kononkova, I. A. Roshchina, V. A. Alexeev, L. L. Kashkarov, D. D. Badyukov, and V. S. Sevast'yanov, "Analytical results for the material of the Chelyabinsk meteorite," *Geochemistry Int.*, vol. 51, no. 7, pp. 522–539, 2013.

[153] A. Ruzicka, J. N. Grossman, and L. Garvie, "The Meteoritical Bulletin, No. 100, 2014 June," *Meteorit. Planet. Sci.*, vol. 49, no. 8, pp. E1–E101, 2014.

[154] H. C. Connolly, C. Smith, G. Benedix, L. Folco, K. Righter, J. Zipfel, A. Yamaguchi, and H. C. Aoudjehane, "The Meteoritical Bulletin, No. 93, 2008 March," *Meteorit. Planet. Sci.*, vol. 43, no. 3, pp. 571–632, 2008.

[155] J. P. Cleveland, S. Manne, D. Bocek, and P. K. Hansma, "A nondestructive method for determining the spring constant of cantilevers for scanning force microscopy," *Rev. Sci. Instrum.*, vol. 64, no. 2, pp. 403–405, 1993.

[156] J. L. Hutter and J. Bechhoefer, "Calibration of atomic-force microscope tips," *Rev. Sci. Instrum.*, vol. 64, no. 7, pp. 1868–1873, 1993.

[157] O. A. Ageev, O. I. Ilin, A. S. Kolomiytsev, M. V. Rubashkina, V. A. Smirnov, and A. A. Fedotov, "Investigation of Effect of Geometrical Parameters of Vertically Aligned Carbon Nanotubes on their Mechanical Properties," *Adv. Mater. Res.*, vol. 894, pp. 355–359, 2014.

[158] Z. Ma, "Adhäsionsmessung von Carbon Nanotubes bei hohen und tiefen Temperaturen für den Einsatz in der Weltraumtechnik," Bachelor's thesis, Karlsruhe Institute of Technology, 2017.

[159] D. J. Babu, M. Mail, W. Barthlott, and J. J. Schneider, "Superhydrophobic Vertically Aligned Carbon Nanotubes for Biomimetic Air Retention under Water (Salvinia Effect)," *Adv. Mater. Interfaces*, vol. 4, no. 13, pp. 1–6, 2017.

[160] O. K. Dudko, A. E. Filippov, J. Klafter, and M. Urbakh, "Beyond the conventional description of dynamic force spectroscopy of adhesion bonds," *Proc. Natl. Acad. Sci.*, vol. 100, no. 20, pp. 11378–11381, 2003.

[161] O. Gohardani, M. C. Elola, and C. Elizetxea, "Potential and prospective implementation of carbon nanotubes on next generation aircraft and space vehicles: A review of current and expected applications in aerospace sciences," *Prog. Aerosp. Sci.*, vol. 70, pp. 42–68, 2014.

[162] J. Vaverka, A. Pellinen-Wannberg, J. Kero, I. Mann, A. De Spiegeleer, M. Hamrin, C. Norberg, and T. Pitkänen, "Detection of meteoroid hypervelocity impacts on the Cluster spacecraft: First results," *J. Geophys. Res. Sp. Phys.*, vol. 122, no. 6, pp. 6485–6494, 2017.

[163] W. Cho, M. Schulz, and V. Shanov, "Kinetics of Growing Centimeter Long Carbon Nanotube Arrays," in *Synthesis and Applications of Carbon nanotubes and their properties*, 2013, pp. 223–237.

[164] M. J. Mumma and S. B. Charnley, "The Chemical Composition of Comets—Emerging Taxonomies and Natal Heritage," *Annu. Rev. Astron. Astrophys.*, vol. 49, pp. 471–524, 2011.

[165] C. Lutz, Z. Ma, R. Thelen, J. Syurik, O. Il'in, O. Ageev, P. Jouanne, and H. Hölscher, "Analysis of Carbon Nanotube Arrays for Their Potential Use as Adhesives Under Harsh Conditions as in Space Technology," *Tribol. Lett.*, vol. 67, pp. 1–10, 2019.

[166] A. Kumar, A. Cross, K. Manukyan, R. R. Bhosale, L. J. P. Van Den Broeke, J. T. Miller, A. S. Mukasyan, and E. E. Wolf, "Combustion synthesis of copper-nickel catalysts for hydrogen production from ethanol," *Chem. Eng. J.*, vol. 278, pp. 46–54, 2015.

[167] D. Jiles, *Introduction to Magnetism and Magnetic Materials*, 3rd ed. Boca Raton: CRC Press, 2016.

[168] Nuffield Foundation and the Royal Society of Chemistry, "The equilibrium between two coloured cobalt species," 2018.

[169] J. H. Snoeijer, J. Ziegler, B. Andreotti, M. Fermigier, and J. Eggers, "Thick films of viscous fluid

coating a plate withdrawn from a liquid reservoir," *Phys. Rev. Lett.*, vol. 100, no. 24, pp. 8–11, 2008.

[170] R. Krechetnikov and G. M. Homsy, "Experimental study of substrate roughness and surfactant effects on the Landau-Levich law," *Phys. Fluids*, vol. 17, no. 10, 2005.

[171] P. Ball, "NONE MORE BLACK," *Nat. Mater.*, vol. 15, p. 500, 2016.

[172] M. G. Lawrence, "The relationship between relative humidity and the dewpoint temperature in moist air: A simple conversion and applications," *Bull. Am. Meteorol. Soc.*, vol. 86, no. 2, pp. 225–233, 2005.

[173] D. Landolt, *Corrosion and Surface Chemistry of Metals*. Boca Raton: CRC Press, 2007.

[174] G. P. Hatch and R. E. Stelter, "Magnetic design considerations for devices and particles used for biological high-gradient magnetic separation (HGMS) systems," *J. Magn. Magn. Mater.*, vol. 225, no. 1–2, pp. 262–276, 2001.

[175] Supermagnete, "Physical Magnet Data." [Online]. Available: https://www.supermagnete.de/eng/data_table.php.

[176] S.-P. Chai, S. H. S. Zein, and A. R. Mohamed, "Synthesizing carbon nanotubes and carbon nanofibers over supported-nickel oxide catalysts via catalytic decomposition of methane," *Diam. Relat. Mater.*, vol. 16, no. 8, pp. 1656–1664, 2007.

[177] A. A. Ovchinnikov, "Giant diamagnetism of carbon nanotubes," *Phys. Lett. A*, vol. 195, no. 1, pp. 95–96, 1994.

[178] R. P. Bajpai, U. Chandrasekhar, and A. R. Arankalle, *Innovative Design, Analysis and Development Practices in Aerospace and Automotive Engineering*. New Delhi: Springer, 2014.

[179] J. H. Lehman, M. Terrones, E. Mansfield, K. E. Hurst, and V. Meunier, "Evaluating the characteristics of multiwall carbon nanotubes," *Carbon N. Y.*, vol. 49, no. 8, pp. 2581–2602, 2011.

[180] K. L. Parry, A. G. Shard, R. D. Short, R. G. White, J. D. Whittle, and A. Wright, "ARXPS characterisation of plasma polymerised surface chemical gradients," *Surf. Interface Anal.*, vol. 38, no. c, pp. 1497–1504, 2006.

[181] H. Ago, T. Kugler, F. Cacialli, W. R. Salaneck, M. S. P. Shaffer, A. H. Windle, and R. H. Friend, "Work Functions and Surface Functional Groups of Multiwall Carbon Nanotubes," *J. Phys. Chem. B*, vol. 103, no. 38, pp. 8116–8121, 1999.

[182] I. Retzko and W. e. s. Unger, "Analysis of Carbon Materials by X-ray Photoelectron Spectroscopy and X-ray Absorption Spectroscopy," *Adv. Eng. Mater.*, vol. 5, no. 7, pp. 519–522, 2003.

[183] L. Ge, L. Ci, A. Goyal, R. Shi, L. Mahadevan, P. M. Ajayan, and A. Dhinojwala, "Cooperative adhesion and friction of compliant nanohairs," *Nano Lett.*, vol. 10, no. 11, pp. 4509–4513, 2010.

[184] Y. Zhao, T. Tong, L. Delzeit, A. Kashani, M. Meyyappan, and A. Majumdar, "Interfacial energy and strength of multiwalled-carbon-nanotube-based dry adhesive," *J. Vac. Sci. Technol. B Microelectron. Nanom. Struct.*, vol. 24, no. 1, pp. 331 – 335, 2006.

[185] D. Zhou and S. Seraphin, "Complex branching phenomena in the growth of carbon nanotubes," *Chem. Phys. Lett.*, vol. 238, no. 4–6, pp. 286–9, 1995.

[186] C. Sathiskumar, M. Karthik, and S. Karthikeyan, "Synthesis of Y-Junction Carbon Nano-Fibers by CVD Process from Tire Pyrolysis Oil," *J. Environ. Nanotechnol.*, vol. 4, no. 1, pp. 23–26, 2015.

[187] N. Gothard, C. Daraio, J. Gaillard, R. Zidan, S. Jin, and a. M. Rao, "Controlled Growth of Y-Junction Nanotubes Using Ti-Doped Vapor Catalyst," *Nano Lett.*, vol. 4, no. 2, pp. 213–217, Feb. 2004.

[188] S. Malik, Y. Nemoto, H. Guo, K. Ariga, and J. P. Hill, "Fabrication and characterization of branched carbon nanostructures," *Beilstein J. Nanotechnol.*, vol. 7, no. 1, pp. 1260–1266, 2016.

[189] J. Huang, D. H. Kim, R. Seelaboyina, B. K. Rao, D. Wang, M. Park, and W. Choi, "Catalysts effect on single-walled carbon nanotube branching," *Diam. Relat. Mater.*, vol. 16, no. 8, pp. 1524–1529, Aug. 2007.

[190] P. Nagy, R. Ehlich, and L. P. Bir, "Rapid communication Y-branching of single walled carbon nanotubes," *Appl. Phys. A*, vol. 483, pp. 481–483, 2000.

[191] T. Loritz, “Konstruktion, Aufbau und experimentelle Inbetriebnahme einer Versuchsvorrichtung zur Herstellung von Kohlenstoffnanoröhrchen,” Master’s thesis, Karlsruhe Institute of Technology, 2017.

[192] A. Förste, M. Pfirrmann, J. Sachs, R. Gröger, S. Walheim, F. Brinkmann, M. Hirtz, H. Fuchs, and T. Schimmel, “Ultra-large scale AFM of lipid droplet arrays: Investigating the ink transfer volume in dip pen nanolithography,” *Nanotechnology*, vol. 26, no. 17, pp. 1–7, 2015.

[193] M. Davydova, A. de los Santos Pereira, M. Bruns, A. Kromka, E. Ukraintsev, M. Hirtz, and C. Rodriguez-Emmenegger, “Catalyst-free site-specific surface modifications of nanocrystalline diamond films via microchannel cantilever spotting,” *RSC Adv.*, vol. 6, no. 63, pp. 57820–57827, 2016.

[194] J. Y. Huang, S. Chen, Z. Q. Wang, K. Kempa, Y. M. Wang, S. H. Jo, G. Chen, M. S. Dresselhaus, and Z. F. Ren, “Superplastic carbon nanotubes,” *Nature*, vol. 439, no. 7074, pp. 281–281, 2006.

[195] E. J. Garcia, A. J. Hart, B. L. Wardle, and A. H. Slocum, “Fabrication of composite microstructures by capillarity-driven wetting of aligned carbon nanotubes with polymers,” *Nanotechnology*, vol. 18, no. 16, p. 165602, 2007.

[196] Y. Boonyongmaneerat, “Effects of low-content activators on low-temperature sintering of tungsten,” *J. Mater. Process. Technol.*, vol. 209, no. 8, pp. 4084–4087, 2009.

[197] S. K. Name, *Believe: The Fine Art of Setting Yourself Free*. Bloomington: Balboa Press, 2013.